Philipps Universität Marburg

Linear and Nonlinear Optical Properties of Germanium and Dilute Nitride Containing Semiconductors

Dissertation

zur

Erlangung des Doktorgrades

der Naturwissenschaften

(Dr. rer. nat.)

dem

Fachbereich Physik

der Philipps-Universität Marburg

vorgelegt von

Phillip Springer

aus Wuppertal

Marburg (Lahn), 2016

Phillip Springer
Mainzer Gasse 33, Büro 02 001
35037 Marburg
AG Theoretische Halbleiterphysik
Fachbereich Physik der Philipps-Universität Marburg

Vom Fachbereich Physik der Philipps-Universität Marburg
als Dissertation angenommen am

Erstgutachter: Prof. Dr. Stephan W. Koch
Zweitgutachter: PD Dr. Sangam Chatterjee

Tag der mündlichen Prüfung: 11. Mai 2016
Hochschulkennziffer 1180

Für meine Eltern, Joachim und Cornelia.
Für meine Liebe, Patricia.

Zusammenfassung

Kaum ein Forschungsfeld prägt unser heutiges Leben so sehr wie die Halbleiterphysik. Wir interagieren ständig mit unseren Smartphones, unseren Tabletcomputern oder Heimrechnern. Kurzum: mit Geräten, die ohne Grundlagenforschung in der Festkörperphysik nicht möglich wären. Neben den alltäglichen Erfahrungen werden Halbleiter auch in der Medizintechnik, Materialbearbeitung, Umweltanalytik, Energieerzeugung oder der optischen Datenübertragung eingesetzt. Das Streben nach Energieeffizienz bei gleichzeitig höherer Rechenleistung und kleineren Bauelementen treibt die Wissenschaft bis heute an.

So haben Halbleiter Einzug in unser Leben gefunden und stellen einen wesentlichen Bestandteil unserer Welt dar. Die rasante Entwicklungsumgebung hat dabei diverse Anwendungsmöglichkeiten hervorgebracht. Diese reichen von Prozessoren (englisch: central-processing unit, CPU) bis hin zu Datenspeichern in Form von solid-state drives (SSDs). Die Vielfältigkeit von Halbleitern ist ihrer Kristallstruktur geschuldet, welche der Grund für die Bildung der Bandlücke ist. Diese trennt besetzte von unbesetzten elektronischen Zuständen und bestimmt hauptsächlich, welche Energie von der Halbleiterlegierung absorbiert, verstärkt oder emittiert werden kann. Mittels Verspannung und Materialkomposition kann diese Bandlücke verändert werden und ist die Grundlage ihrer Flexibilität. So kann man die Farbe von Leuchtdioden (englisch: light-emitting-diode, LED) über das gesamte sichtbare Spektrum anpassen, indem man die beteiligten Materialien sorgfältig auswählt. Daneben zeichnen sich Halbeiter durch hohe Effizienz, eine lange Lebensdauer und kompakte Bauform aus.

Ein bemerkenswerter Fortschritt in der Kristallzüchtung und den Dotierungstechniken während den letzten Jahrzehnten hat dazu geführt, dass man mit nahezu atomarer Präzision Halbleiterschichten aufeinander abscheiden kann. Hierbei definieren die verschiedenen Schichten in der Wachstumsrichtung des Kristalls ein Potential für Ladungsträger im Leitungs- und Valenzband. In solchen effektiv niederdimensionalen Systemen ist die Bewegung der Elektronen eingeschränkt, wodurch ihre Energie quantisiert wird. Somit ist es notwendig, die Teilchen quantenmechanisch auf einer mikroskopischen Ebene zu beschreiben und messbare Größen von ihnen abzuleiten. In der vorliegenden Dissertation wird eine mikroskopische Vielteilchentheorie zur Beschreibung optischer Eigenschaften von Halbleitern angewandt und erweitert. Das theoretische Verständnis und der hohe Grad an Reinheit bei der Herstellung haben bereits zu außerordentlich hilfreichen und leistungsstarken Applikation geführt wie etwa integrierten Schaltkreisen oder Halbleiterlasern.

Innerhalb der theoretischen Physik ist die ein mikroskopischer Ansatz aus zwei Gründen besonders interessant: Erstens bilden Halbleitersysteme nahezu ideale quantenmechanische Systeme und

eignen sich somit ausgezeichnet als Modellsystem um fundamentale physikalische Eigenschaften zu untersuchen. Daneben werden die künstlich hergestellten Schichtstrukturen bereits seit geraumer Zeit für praktische Zwecke eingesetzt. Ihre Weiterentwicklung und Verbesserung erfordert ein detailliertes Wissen über die elektronischen und optischen Vorgänge der zugrundeliegenden mikroskopischen Prozesse.

Aber auch von experimenteller Seite ist die Untersuchung von Halbleitern faszinierend. Die Beherrschung der Ultrakurzzeitspektroskopie erlaubt die Untersuchung von mikroskopischen Prozessen durch die Erzeugung von Lichtpulsen mit einer Länge von unter einer Pikosekunde (1 ps = 10^{-12} s). Hierzu sind Methoden der kohärenten Spektroskopie wie etwa Vier-Wellen-Mischen [1–3] oder Anregungs-Abfrage-Experimente [4, 5] entwickelt. Bei Halbleiterproben mit Bandlücken von etwa einem Elektronvolt (1 eV≙1240 nm≙242 THz) kann Licht im sichtbaren und nah-infraroten Teil des elektromagnetischen Spektrums elektronische Anregungen erzeugen. Hierbei werden Elektronen vom Valenz- ins Leitungsband gehoben und erzeugen daraufhin eine Vielzahl von kohärenten und inkohärenten Korrelationen. Umfassende Experiment-Theorie-Vergleiche machen es somit möglich, solche Korrelationen über Dephasierungs-, Relaxations- oder Streuprozesse zu studieren, da sie sich direkt in linearer oder nicht-linearer optischer Spektroskopie- und Lumineszenzmessungen widerspiegeln. In dieser Arbeit werden sowohl nicht-linear optische Absorption als auch Photolumineszenzspektren berechnet, um experimentelle Daten zu interpretieren.

Wohl eine der bekannteste Korrelationen ist das Exziton. Als gebundenes Elektron-Loch-Paar ist es ein Quasiteilchen, welches viele Gemeinsamkeiten mit dem Wasserstoff Atom aufweist. Seine Bindungsenergie allerdings ermöglicht intraexzitonische Übergänge, die im Bereich von einigen Terahertz (THz) liegen (1 THz≙4.1 meV). Möchte man also exzitonische Vorgänge und Eigenschaften untersuchen, stellt die Terahertzspektroskopie das ideale Werkzeug dar. Neben rein spektroskopischen Einsatzmöglichkeiten kann starke THz Strahlung auch genutzt werden, um exzitonische Zustände kohärent zu manipulieren [6]. Auch intersubband Übergänge können mit elektromagnetischer Strahlung im THz Bereich induziert werden [7]. Mittels des THz Feldes können dann sogar selektiv Ladungsträger, Exzitonen oder Zweiteilchen-Korrelationen zwischen verschiedenen Halbleiterschichten transportiert werden. Im Rahmen dieser Dissertation wird die etablierte Theorie zur Berechnung von Exziton-Wellenfunktionen und THz Absorptionsspektren auf Halbleiter erweitert, welche eine Anisotropie der effektiven Elektron- und Lochmassen aufweisen.

Die theoretischen Grundlagen für die Erörterung aller weiteren Untersuchungen werden in Kapitel 2 diskutiert. Neben dem System-Hamiltonian werden wichtige Gleichungen zur Berechnung von Bandstrukturen, Photolumineszenz und THz Absorption besprochen. Im anschließenden Kapitel 5 wird die Wannier Gleichung auf Halbleiter mit anisotropen effektiven Ladungsträgermassen erweitert. Die Wannier Gleichung ist eine Eigenwertgleichung für die Wellenfunktion und Bindungsenergien von Exzitonen, die bisher erfolgreich für direkte Halbleiter wie Galliumarsenid (GaAs) angewendet wurde, in denen die effektiven Elektron- und Lochmassen in alle Raumrichtungen identisch sind. Indirekte Halbleiter wie Germanium (Ge) oder Silizium (Si) aber weisen

unterschiedliche Massen bezüglich der Raumrichtungen auf. Am Beispiel von Ge zeigt sich als Konsequenz der Massenanisotropie, dass die Exziton-Wellenfunktionen ihre Form im Vergleich zu isotropen Massen stark ändern. Da die Verallgemeinerung der Theorie auf einer Entwicklung in Kugelflächenfunktionen basiert, ist die Änderung der Form eine Folge von Kopplungen verschiedener Quantenzahlen. Für Ge und Si wird außerdem das THz Absorptionsspektrum berechnet, wobei auch die Entartung der indirekten Bandkante Beachtung findet. Aufgrund dieser Entartung werden zwei energetisch unterscheidbare Resonanzen beobachtet, die der parallelen und senkrechten Komponente der THz Polarisation zugeordnet werden können. Den Abschluss des Kapitels bildet die Berechnung der optischen Absorption in Rutil nahe der Bandkante. Zu diesem Zweck wurden ab-initio Berechnungen mit den vorher beschriebenen Exziton-Wellenfunktionen zu einer neuen Methode kombiniert.

In Kapitel 4 werden experimentelle Anregungs-Abfrage-Experimente von Ge and Galliumindiumarsenid ((Ga,In)As) Quantenfilmen analysiert. Im Experiment zeigt die Ge Probe auffällige Seitenbanden für starke Anregungsdichten. Die (Ga,In)As Heterostruktur zeigt unter äquivalenten Bedingungen jedoch nur den erwarteten Effekt der anregungsinduzierten Dephasierung. Mittels der mikroskopischen Vielteilchentheorie kann der Unterschied auf verschiedene Dephasierungsmechanismen der beiden beiden Proben zurückgeführt werden.

Kapitel 5 adressiert wieder experimentelle Daten einer speziellen Halbleiterheterostruktur. Diese wurde so hergestellt, dass sie eine Typ-II Photolumineszenz zeigt. Eine dichteabhängige Studie der Photolumineszenz offenbart eine ungewöhnlich Breite Bande, was mit einem Vergleich zu theoretischen Spektren auf die beteiligten Übergänge und Wellenfunktionen zurückgeführt werden kann. Bedingt durch den speziellen Probenaufbau ist es möglich, die energetische Bandanpassung von Galliumnitridarsenid (Ga(N,As)) zwischen GaAs Barrieren zu bestimmen, wofür ein leichter Typ-I Übergang gefunden wird.

Acknowledgements

First and foremost, I want to thank my parents and my sister Nora who supported me during all stages of my thesis and without whom this work would not have been possible. I especially would like to thank Prof. Dr. Stephan W. Koch for his guidance and supervision, and for giving me the opportunity to study theoretical physics on extremely interesting topics. His guidance was essential in all the small and large problems I faced. Just as much I want to thank Prof. Dr. Mackillo Kira, especially for teaching me the basic and vital things in science. His everlasting patience and always competent and motivating feedback on my work helped me to push forward whenever I was stuck which really means a lot to me. This work would also not have been possible without the experiments, which I had the opportunity and pleasure to analyze. In this regard, I would like to thank Dr. Sangam Chatterjee, Prof. Dr. Wolfram Heimbrodt, Prof. Dr. Kerstin Volz, Dr. Wolfgang Stolz, and their coworkers. Special thanks are entitled to Dr. Sangam Chatterjee and Prof. Dr. Reinhard Noack for agreeing to evaluate my thesis. Especially Sangam also helped me to understand all the complex problems from an experimental viewpoint in many inspiring discussions. I truly value the help from Prof. Dr. John Sipe, who guided me through the first year in many helpful conversations about physics and pudding. I also thank Martin, Christian, Uli, Markus, Osmo, Christoph, Lukas, Dominik, Benjamin, Tineke, Prof. Dr. Peter Thomas, and the rest of the group for a pleasant and relaxed atmosphere, for a lot of tasty group dinners, for many interesting discussions about physics, running, the Braveheart Battle, funny excuses from students, and other stuff. With Martin, I shared a great and fun time together in the office and I will never forget some epic moments we shared. Both Martin and Christian often helped me to fight off depressing times with extensive exercise sessions whenever things did not work as expected. I also got a lot of support from old friends and members from my former group. Thank you David, Exi, Alex, Marc, Ajanth, Norman, Tobi, and Daniel. I want to especially emphasize my acknowledgement for Tobi and Christian for extensive proof reading of my manuscript.

I gratefully acknowledge financial support by the DFG in the framework of the GRK 1782.

Last but definitely not least, I want to thank Patricia. You keep on being the most significant part of my life. You always protected me from myself, always supported and encouraged my work. I am excited to find out where our way leads us next. **I love you**

Author's Contributions

Publications in Peer-Reviewed Journals

[I] T. B. Norris, P. Springer, and M. Kira, in Front. opt. 2014 (2014), LTu1I.1.

[II] K. Jandieri, P. Ludewig, T. Wegele, A. Beyer, B. Kunert, P. Springer, S. D. Baranovskii, S. W. Koch, K. Volz, and W. Stolz, J. Appl. Phys. **118**, 065701 (2015).

[III] P. Springer, S. Gies, P. Hens, C. Fuchs, H. Han, J. Hader, J. Moloney, W. Stolz, K. Volz, S. Koch, and W. Heimbrodt, J. Lumin. **175**, 255–259 (2016).

[IV] P. Springer, S. W. Koch, and M. Kira, J. Opt. Soc. Am. B **33**, C30 (2016), arXiv:1602.02972.

[V] O. Vänskä, M. Ljungberg, P. Springer, D. Sánchez-Portal, M. Kira, and S. W. Koch, J. Opt. Soc. Am. B **33**, C123 (2016), arXiv:1512.05156.

Publications in Preparation

[VI] P. Springer, P. Rosenow, T. Stroucken, J. Hader, J. V. Moloney, R. Tonner, and S. W. Koch, "An Ab-Initio Modeling Approach for the Optical Properties of Dilute Nitride Semiconductors", in preparation.

[VII] P. Springer, S. W. Koch, M. Kira, N. S. Köster, K. Kolata, S. Chatterjee, J. Cheng, and J. E. Sipe, "Enhancement of Phonon Assisted Optical Transients in Germanium Quantum Wells", in preparation.

[VIII] F. Dobener, P. Springer, P. Ludewig, S. Reinhard, K. Volz, W. Stolz, S. W. Koch, and S. Chatterjee, "Room-temperature optical gain in Ga(N,As,P)/(B,Ga)(As,P) heterostructures", in preparation.

Posters and Talks

[IX] P. Springer, S. W. Koch, M. Kira, J. Cheng, J. E. Sipe, N. S. Köster, K. Kolata, and S. Chatterjee, *Enhancing Optically Induced Transients with Phonon Relaxation*, Poster presented at the Materialforschungstag (Material Sciences Day) Mittelhessen 2014, Gießen, Germany.

[X] P. Springer, S. W. Koch, and M. Kira, *Effect of Anisotropic Mass on Exciton Wave Functions*, Talk presented at the Seminar of the Research Training Group *Functionalization of Semiconductors* (GRK 1782) 2014, Donostia-San Sebastián, Spain.

[XI] P. Springer, S. W. Koch, M. Kira, J. Cheng, J. E. Sipe, N. S. Köster, K. Kolata, and S. Chatterjee, *Enhancing optically induced transients with phonon relaxation*, Poster presented at the Nonlinear Optics and Excitation Kinetics in Semiconductors (NOEKS) 2014, Bremen, Germany.

[XII] P. Springer, T. Stroucken, S. W. Koch, P. Rosenow, R. Tonner, J. Hader, and J. V. Moloney, *Microscopic Calculations of the Optical Properties of Novel Bismide and Nitride Containing III-V Semiconductors*, Talk presented at the Spring Meeting 2015 of the German Physical Society (DPG), Berlin, Germany.

[XIII] P. Springer, P. Rosenow, K. Jandieri, P. Ludewig, T. Wegele, A. Beyer, B. Kunert, R. Tonner, S. D. Baranovskii, K. Volz, W. Stolz, and S. W. Koch, *Photoluminescence in Ga($N_xAs_{1-x-y}P_y$) Systems*, Poster presented at the Materialforschungstag (Material Sciences Day) Mittelhessen 2015, Marburg, Germany.

[XIV] P. Springer, S. Gies, W. Heimbrodt, and S. W. Koch, *Optical Properties of Nitride Containing Quantum Wells*, Poster presented at the GRK Seminar 2015, Hofheim, Germany.

[XV] P. Springer, S. W. Koch, and M. Kira, *Consequences of Anisotropic Electron Masses on THz Absorption*, Talk presented at the GRK Seminar 2015, Hofheim, Germany.

Original Contributions

Publication [II] provides a simple model developed by Stolz et al. to extract nitrogen compositions in Ga(N,As,P)/GaP quantum well heterostructures. In this regard, I conducted multi-band electronic structure calculations based on the $\boldsymbol{k} \cdot \boldsymbol{p}$ theory with a band anticrossing extension. To validate the simple model, I calculated the corresponding photoluminescence spectra and compared them with experiments.

The photoluminescence spectrum of a multi quantum well heterostructure is the subject of publication [III]. Experiments have been conducted by W. Heimbrodt et al. while I applied an established microscopic many-body theory to obtain the multi-band photoluminescence of this system. My calculations form the basis for interpretation of the experimental spectra.

In publication [IV], I developed a microscopic approach to compute the excitonic properties and the corresponding terahertz response for semiconductors which exhibit anisotropic effective masses. I applied the approach to germanium and quantitatively predicted the outcome and interpretation of a future experiment.

In publication [V], the cluster-expansion method is combined with the density-functional theory into a hybrid approach. It is applied to the optical absorption of rutile TiO_2. For this purpose,

exciton wave functions and binding energies are relevant, which I provided. Optical-matrix elements were computed via density-functional theory by M. Ljungberg. The main author, O. Vänskä, composed the results to obtain the optical absorption and is responsible for the theoretical model.

Contents

Zusammenfassung I

Acknowledgements V

Author's Contributions VII

1 Introduction 1

2 Theoretical Framework 5

2.1 System Hamiltonian . . . 5
2.2 Equations of Motion . . . 7
2.3 Band Structure . . . 7
2.3.1 Bulk Semiconductors . . . 7
2.3.2 Semiconductor Heterostructures . . . 9
2.4 Semiconductor Luminescence Equations . . . 10
2.5 Semiconductor Bloch Equations . . . 11
2.5.1 Bulk Semiconductors . . . 13
2.6 Inhomogeneous Broadening . . . 13
2.7 Optical Absorption . . . 14
2.8 Wannier Equation . . . 15
2.9 Linear THz Spectroscopy . . . 16

3 Effects of Mass Anisotropy on the Optical Properties of Semiconductors 19

3.1 THz Spectroscopy of Bulk Germanium . . . 19
3.1.1 Generalized Wannier Equation with Mass Anisotropy . . . 20
3.1.2 Excitons in Germanium . . . 25
3.1.3 Single-Valley Response to Classical THz Excitation . . . 28
3.1.4 Muli-Valley Response to Classical THz Excitation . . . 32
3.2 THz Spectroscopy of Bulk Silicon . . . 36
3.3 Absorption of Bulk Rutile . . . 38
3.3.1 Density Functional Theory . . . 38
3.3.2 Band Structure and Matrix Elements . . . 40
3.3.3 Absorption . . . 42

4 Enhancement of Optical Transients in Germanium Quantum Wells 47
4.1 Experiment 47
4.2 Two-Level System 50
4.3 Quantum-Well System 53
4.3.1 Dephasing 54
4.4 Experiment-Theory Comparison 57

5 Optical Properties of Highly Mismatched Alloys 61
5.1 Band Anticrossing Model 62
5.2 Valence Band Offset Determination of Ga(N,As)/GaAs Quantum Wells 64
5.2.1 Sample Series 65
5.2.2 Valence Band Offset 66
5.2.3 Dominant Transitions 68

6 Conclusion and Outlook 73

Bibliography 75

Wissenschaftlicher Werdegang 85

1 Introduction

The good thing about science is that it's true whether or not you believe in it.

(Neil deGrasse Tyson, American astrophysicist, cosmologist, and author)

Today, only few scientific fields have such an enormous impact on our daily lives as semiconductor physics. We constantly interact with smartphones, tablets, and computers; devices realized on the basis of fundamental solid-state research. Beside our daily experiences with semiconductors they are utilized in medical engineering, material machining, environmental technology, and optical communication. The quest for ever increasing computing power, energy efficiency, and miniaturization drives the fundamental research until today.

Hence, semiconductors have become an integral part of our world. A rapid development environment has created diverse applications ranging from central processing units (CPUs) to data storage solutions in the form of the solid-state drive (SSD). This mutability is owed to the inherent crystal structure of semiconductors, giving rise to the band gap, which separates occupied from unoccupied electronic states. The band gap of a semiconductor alloy mainly determines which energies can be absorbed, amplified, or emitted. Using strain and alloy composition allows to tune the band gap, permitting the fabrication of light-emitting diodes (LEDs) over the entire visible spectrum. Besides the flexibility of these materials, they are featured with a high efficiency, long life time, and compact design.

A remarkable progress in crystal growth and doping techniques during the past few decades has allowed the deposition of semiconductor heterostructure layers with almost atomic precision. The different layers define a potential landscape in the growth direction for charge carriers in the conduction and valence bands. By effectively reducing the system's dimensionality, the motion of electrons is then confined. As a consequence, their energy becomes quantized. Therefore, a quantum mechanical description on a microscopic level is required from which measurable quantities can be derived. In this work, a microscopic many-body theory to describe optical properties of semiconductors is used and further extended. Theoretical comprehension and a high degree of purity during the manufacturing process has led to some extremely helpful and powerful applications, including integrated circuits and semiconductor lasers.

Concerning theoretical physics, a microscopic approach is interesting for two reasons: First, semiconductor structures constitute almost ideal quantum mechanical systems thus qualifying as model systems to study fundamental physical properties. In addition, artificially produced layered

structures have been introduced for a considerable time. To improve and optimize these devices, it is indispensable to gain detailed knowledge about the electrical and optical mechanisms of the underlying microscopic processes.

The experimental prospect of semiconductors is equally fascinating. Mastering ultrafast optical pulses with a duration of less than a picosecond ($1\,\mathrm{ps} = 10^{-12}\,\mathrm{s}$) allowed to experimentally study microscopic processes via methods such as four-wave mixing [1–3] and pump–probe spectroscopy [4, 5]. Applied to semiconductors whose band gap is of the order of one electronvolt ($1\,\mathrm{eV} \mathrel{\hat{=}} 1240\,\mathrm{nm} \mathrel{\hat{=}} 242\,\mathrm{THz}$), light frequencies in the visible and near-infrared regime of the electromagnetic spectrum can induce excitations, e.g. lift an electron from the valence into the conduction band while coherent and incoherent correlations are generated subsequently. Comprehensive experiment–theory comparison have allowed to study such correlations via relaxation, dephasing, and scattering processes of carriers after optical excitation, which in turn can be monitored by linear and nonlinear optical spectroscopy or photoluminescence (PL) measurements. Both nonlinear absorption and PL spectra are analyzed in this thesis to interpret experimental data.

One of the most prominent examples of correlations is the exciton. This quasiparticle consists of a truly bound electron–hole pair and shows major similarities with the hydrogen atom. However, its binding energy allows for interexcitonic transitions in the range of a few terahertz ($1\,\mathrm{THz} \mathrel{\hat{=}} 4.1\,\mathrm{meV}$) in common semiconductors. That makes THz spectroscopy an excellent tool to investigate these transitions. Apart from purely spectroscopical applications, strong THz fields can coherently manipulate excitonic states [6]. Intersubband transitions can also be investigated and manipulated via THz radiation [7]. Resonantly applied, they can selectively transport charge carriers, excitons, or two-particle correlations across semiconductor layers. In the context of this thesis, the established theory to compute exciton wavefunctions and THz-absorption spectra is extended to semiconductors that have anisotropic effective electron and hole masses.

The theoretical basis is revised in Chapter 2. It introduces the system Hamiltonian and covers the relevant equations to compute a band structure, PL, and THz-absorption spectra. In the adjacent Chapter 3, the Wannier equation is extended to semiconductors with anisotropic masses. The Wannier equation defines an eigenvalue problem for the exciton wavefunctions and binding energies. It was successfully applied to materials like gallium arsenide (GaAs), which is a direct semiconductor with isotropic masses. Indirect substances like germanium (Ge) or silicon (Si) however exhibit different masses regarding the spatial directions. As an example, Ge is used to show that mass anisotropy changes the shape of the exciton wavefunctions. Since the generalization of the theory is based on an expansion into spherical harmonics, the altered appearance of the wavefunctions is the outcome of the coupling between different quantum numbers. The THz spectra for Ge and Si are calculated explicitly considering the degeneracy of the band edge. Owing to this degeneracy, two energetically close but separated resonances are observed which can be assigned to the parallel and perpendicular component of the THz field. The closing of this Chapter describes the calculations of the near-bandgap optical absorption of rutile. For this purpose, the generalized the-

ory of exciton wavefunctions is combined with ab-initio calculations which provide optical-matrix elements.

In Chapter 4, pump–probe absorption experiments of (Ga,In)As and Ge quantum wells (QWs) are analyzed. Experimentally, prominent optical transients are observed only in the Ge sample, while the (Ga,In)As sample only shows the usual excitation-induced dephasing (EID) signatures. Using a fully microscopic many-body theory, the difference can be ascribed to different charge carrier dephasing mechanisms.

Chapter 5 addresses the PL spectrum of a specific heterostructure, which was designed to show a type-II PL. An unusually broad PL line shape was observed in an excitation-density dependent experiment but could be explained by a thorough investigation of the participating electronic transitions. The special design of structure also allows to determine the fundamental nature of the valence band offset (VBO) of gallium nitride arsenide (Ga(N,As)) QWs between GaAs barriers, which are found to have a weak type-II alignment.

2 Theoretical Framework

This Chapter provides a short revision of the essential properties and correlations necessary in the context of this thesis. The derivations of the relevant equations have been covered in detail throughout numerous publications [8–12] and shall not be repeated here. The purpose of this Chapter is rather the introduction of a concise notation to be used throughout the thesis.

2.1 System Hamiltonian

The starting point of relevant theoretical investigations is the many-body Hamiltonian

$$H = H_0 + H_\mathrm{C} + H_\mathrm{D} + H_\mathrm{P}\,, \tag{2.1}$$

describing non-interacting particles (including electrons, photons, and phonons) via H_0, Coulomb or electron–electron interaction via H_C, dipole or light–matter interaction via H_D, and carrier–phonon interactions via H_P. It is obtained from the minimal-substitution Hamiltonian in first quantization for N particles which is determined by the gauge invariance of electrodynamics [13–15]. In the Coulomb gauge, it reads [11]

$$H = \sum_{j=1}^{N}\left[\frac{1}{2m_0}\Big(\boldsymbol{p}_j + |e|\boldsymbol{A}\Big)^2 + V_\mathrm{Cr}(\boldsymbol{r}_j)\right] + \frac{1}{2}\sum_{j,l\neq j}^{N} V(\boldsymbol{r}_j - \boldsymbol{r}_l) + H_\mathrm{em} + H_\mathrm{ph}\,, \tag{2.2}$$

where $\boldsymbol{p}$ and $\boldsymbol{r}$ are the canonical momentum and position operators of particle j moving within the periodic crystal potential V_Cr and having charge $e = -|e|$ and mass m_0. Carrier–carrier interactions are described via the Coulomb potential [16]

$$V(\boldsymbol{r}) = \frac{e^2}{4\pi\epsilon_0\sqrt{\epsilon_1\epsilon_2\epsilon_3}}\frac{1}{\sqrt{\frac{r_1^2}{\epsilon_1}+\frac{r_2^2}{\epsilon_2}+\frac{r_3^2}{\epsilon_3}}}\,, \tag{2.3}$$

containing ϵ_l, the materials background dielectric permittivity in principal directions $l = \{1,2,3\}$, which in general can be anisotropic, e.g. $\epsilon_1 \neq \epsilon_2 \neq \epsilon_3 \neq \epsilon_1$. However, it is worth noting that the Coulomb potential can always be modified into a symmetric function via a coordinate transfor-

mation $\tilde{\boldsymbol{r}} = \left(r_1, \sqrt{\frac{\epsilon_1}{\epsilon_2}} r_2, \sqrt{\frac{\epsilon_1}{\epsilon_3}} r_3\right)$, so that

$$V(\tilde{\boldsymbol{r}}) = V(|\tilde{\boldsymbol{r}}| = \tilde{r}) = \frac{e^2}{4\pi\epsilon_0\sqrt{\epsilon_2\epsilon_3}} \frac{1}{\tilde{r}} . \tag{2.4}$$

Whenever the system is isotropic, $\epsilon_1 = \epsilon_2 = \epsilon_3 \equiv \epsilon_{\mathrm{BG}}$ and $\tilde{\boldsymbol{r}} = \boldsymbol{r}$ maps trivially.

In Eq. (2.2), the transverse light field is given by $\boldsymbol{A}$ and it has been assumed that all external longitudinal fields vanish resulting in no additional potential term. The free-field part in Eq. (2.2) is given by H_{em} and phonon interactions are covered by H_{ph}, whose explicit forms can be found in Refs. [10] and [12].

To obtain the Hamiltonian (2.1) in second quantization from Eq. (2.2), it is usually advantageous to expand the field operators in the Bloch basis

$$\hat{\Psi}(\boldsymbol{r}) = \sum_{\lambda,\boldsymbol{k}} \hat{a}_{\lambda,\boldsymbol{k}}\, \phi_{\lambda,\boldsymbol{k}}(\boldsymbol{r}) , \qquad \hat{\Psi}^\dagger(\boldsymbol{r}) = \sum_{\lambda,\boldsymbol{k}} \hat{a}^\dagger_{\lambda,\boldsymbol{k}}\, \phi^\star_{\lambda,\boldsymbol{k}}(\boldsymbol{r}) , \tag{2.5}$$

containing the creation (annihilation) operator $\hat{a}^\dagger_{\lambda,\boldsymbol{k}}$ ($\hat{a}_{\lambda,\boldsymbol{k}}$) of an electron characterized by a full set of quantum numbers λ and having momentum $\hbar\boldsymbol{k}$. The single-particle wave functions $\phi_{\lambda,\boldsymbol{k}}$ obey the time-independent Schrödinger equation [17]

$$\left[\frac{\boldsymbol{p}^2}{2m_0} + V_{\mathrm{Cr}}(r)\right]\phi_{\lambda,\boldsymbol{k}}(\boldsymbol{r}) = \epsilon_{\lambda,\boldsymbol{k}}\, \phi_{\lambda,\boldsymbol{k}}(\boldsymbol{r}) , \tag{2.6}$$

$$V_{\mathrm{Cr}}(r) = V_{\mathrm{Ion}}(r) + \frac{1}{2m_0^2c_0^2r}\frac{\partial V_{\mathrm{Ion}}(r)}{\partial r}\boldsymbol{S}\cdot\boldsymbol{L} , \tag{2.7}$$

containing the particle's angular momentum and spin $\boldsymbol{L}$ and $\boldsymbol{S}$, respectively, and the ionic crystal potential V_{Ion}. Thus, spin-orbit interactions have been explicitly included.

Several approaches have been developed to solve Eq. (2.6), e.g the $\boldsymbol{k}\cdot\boldsymbol{p}$ method [18–20], the tight-binding model [21, 22], or density functional theory (DFT) [23, 24]. In the scope of this thesis, two different strategies will be used. For the modeling of semiconductor heterostructures, realistic single-particle energies are computed using an 8-band $\boldsymbol{k}\cdot\boldsymbol{p}$ Hamiltonian [25] containing non-parabolicities which emerge due to coupling effects between individual bands. Whenever fundamental physical properties have been investigated, such subsidiary effects can be neglected to identify the essential physics. Thus, the effective-mass approximation (see Section 2.3.1) has been used in these cases.

The wave functions $\phi_{\lambda,\boldsymbol{k}}$ contain the effective dimensionality of the system. In bulk semiconductors, they can be separated into a lattice periodic and a free-particle wave part via Bloch's theorem [26]. In quantum well systems, the envelope-function approximation [10, 12, 27] can be applied to reduce the effective dimensionality. The same approach can be used to obtain quantum-wire and even quantum-dot properties.

2.2 Equations of Motion

The most interesting properties of excited semiconducting materials include the spectral distribution of emitted, transmitted, reflected, or absorbed light. Once the temporal evolution of the relevant expectation values such as the microscopic polarization or the photon-number correlation is known, they can be obtained via a Fourier transformation into the frequency domain. The Heisenberg equation of motion

$$\mathrm{i}\hbar\frac{\partial}{\partial t}\left\langle\hat{O}\right\rangle = \left\langle\left[\hat{O},\hat{H}\right]_{-}\right\rangle, \tag{2.8}$$

can be used to calculate the temporal evolution of the expectation value of an operator $\hat{O}$. However, Eq. (2.8) couples an N to an $(N+1)$-particle operator, which leads to the well known infinite hierarchy of equations. A systematic way to deal with this problem is the cluster-expansion approach (CE). Here, an N-particle quantity is factorized into clusters of single particles, correlated pairs, correlated three particle clusters, and so forth. The truncation at one specific level allows to include only relevant physical effects, while simultaneously reducing the numerical effort.

If the truncation is performed at the single-particle level, the most basic Hartree–Fock approximation is obtained. Many quantum-optical phenomena such as exciton formation or EID require a truncation at higher cluster levels. Neglecting these contributions may yield an incomplete description of the system [28].

2.3 Band Structure

2.3.1 Bulk Semiconductors

A wave function in a periodic potential fulfills Bloch's theorem [26]. Thus, it must necessarily have the form

$$\phi_{\lambda,\boldsymbol{k}}(\boldsymbol{r}) = \frac{1}{\sqrt{L^3}}\,\mathrm{e}^{\mathrm{i}\boldsymbol{k}\cdot\boldsymbol{r}}\,u_{\lambda,\boldsymbol{k}}(\boldsymbol{r}), \tag{2.9}$$

where $u_{\lambda,\boldsymbol{k}}$ is the lattice-periodic part of the wave function and L^3 is the quantization area. This can be used in Eq. (2.6) to obtain

$$\left[\frac{\boldsymbol{p}^2}{2m_0} + V_{\mathrm{Cr}}(r) + \frac{\hbar}{m_0}\boldsymbol{k}\cdot\boldsymbol{p}\right]u_{\lambda,\boldsymbol{k}}(\boldsymbol{r}) = \left(\epsilon_{\lambda,\boldsymbol{k}} - \frac{\hbar^2\boldsymbol{k}^2}{2m_0}\right)u_{\lambda,\boldsymbol{k}}(\boldsymbol{r}). \tag{2.10}$$

Considering the term proportional to $\boldsymbol{k}\cdot\boldsymbol{p}$ being a small disturbance, second-order non-degenerate perturbation theory can be applied, once the eigenvalue problem (2.10) has been solved for one specific $\boldsymbol{k} = \boldsymbol{k}_0$. For momenta $\boldsymbol{k}$ within the vicinity of $\boldsymbol{k}_0$, the lattice periodic wave function is then

given by [29]

$$u_{\lambda,\boldsymbol{k}}(\boldsymbol{r}) = \sum_{\nu} c_{\lambda,\nu,\boldsymbol{k}}\, u_{\nu,\boldsymbol{k}_0}(\boldsymbol{r})\,, \tag{2.11}$$

where

$$c_{\lambda,\nu,\boldsymbol{k}} = \delta_{\lambda,\nu} + \left(1-\delta_{\lambda,\nu}\right)\frac{\hbar}{m_0}\frac{(\boldsymbol{k}-\boldsymbol{k}_0)\cdot\boldsymbol{p}_{\nu,\lambda}(\boldsymbol{k}_0)}{\epsilon_{\lambda,\boldsymbol{k}_0}-\epsilon_{\nu,\boldsymbol{k}_0}}\,, \tag{2.12}$$

are the expansion coefficients containing the momentum matrix element [11]

$$\boldsymbol{p}_{\nu,\lambda}(\boldsymbol{k}) = \left\langle \nu,\boldsymbol{k}\middle|\mathrm{e}^{-\mathrm{i}\boldsymbol{k}\cdot\boldsymbol{r}}\,\boldsymbol{p}\,\mathrm{e}^{\mathrm{i}\boldsymbol{k}\cdot\boldsymbol{r}}\middle|\lambda,\boldsymbol{k}\right\rangle\,. \tag{2.13}$$

Here, Dirac's notation $\left\langle \boldsymbol{r}\middle|\lambda,\boldsymbol{k}\right\rangle = u_{\lambda,\boldsymbol{k}}(\boldsymbol{r})$ is used.

The single-particle energy of electrons in band λ and in the vicinity of $\boldsymbol{k}_0$ reads [11]

$$\epsilon_{\lambda,\boldsymbol{k}} = \epsilon_{\lambda,\boldsymbol{k}_0} + \sum_{j=1}^{3}\frac{\hbar^2}{2m_{\lambda,j}(\boldsymbol{k})}\Big[\left(\boldsymbol{k}-\boldsymbol{k}_0\right)\cdot\boldsymbol{e}_j\Big]^2\,, \tag{2.14}$$

containing the effective mass

$$\begin{aligned}\frac{1}{m_{\lambda,j}(\boldsymbol{k})} = \frac{1}{m_0} + \frac{2}{\hbar m_0}\frac{\boldsymbol{p}_{\lambda,\lambda}(\boldsymbol{k}_0)\cdot\boldsymbol{e}_j}{\left(\boldsymbol{k}-\boldsymbol{k}_0\right)\cdot\boldsymbol{e}_j} \\ +\frac{2}{m_0^2}\sum_{\nu\neq\lambda,l}\frac{\left(\boldsymbol{k}-\boldsymbol{k}_0\right)\cdot\boldsymbol{e}_l}{\left(\boldsymbol{k}-\boldsymbol{k}_0\right)\cdot\boldsymbol{e}_j}\frac{\boldsymbol{p}_{\lambda,\nu}(\boldsymbol{k}_0)\cdot\boldsymbol{e}_j\,\boldsymbol{p}_{\nu,\lambda}(\boldsymbol{k}_0)\cdot\boldsymbol{e}_l}{\epsilon_{\lambda,\boldsymbol{k}_0}-\epsilon_{\nu,\boldsymbol{k}_0}}\,.\end{aligned} \tag{2.15}$$

Equation (2.14) is essentially the effective-mass equation. The pairwise orthogonal unit vectors $\boldsymbol{e}_j$ of the principal directions j are pointing away from $\boldsymbol{k}_0$ [30]. If the wave functions $u_{\lambda,\boldsymbol{k}_0}(\boldsymbol{r})$ have a well defined parity, then $\boldsymbol{p}_{\lambda,\lambda}(\boldsymbol{k})$ vanishes [12]. Equation (2.14) is also valid in QW systems with the replacement $\boldsymbol{k}\to\boldsymbol{k}_\parallel$.

The ansatz (2.11) used in Eq. (2.10) constitutes a coupled eigenvalue problem that must be solved simultaneously for both the lattice-periodic wave functions $u_{\lambda,\boldsymbol{k}}$ and the energies $\epsilon_{\lambda,\boldsymbol{k}}$. This can be done by diagonalizing the $\boldsymbol{k}\cdot\boldsymbol{p}$ Hamiltonian defined by Eq. (2.10) for a finite set of quantum numbers λ, resulting in realistic band structures and wave functions. Usually, $\boldsymbol{k}_0$ is chosen to be a point of high symmetry, since the wave functions $u_{\lambda,\boldsymbol{k}_0}$ and energies $\epsilon_{\lambda,\boldsymbol{k}_0}$ are known here. In general, $\epsilon_{\lambda,\boldsymbol{k}_0}$ refers to a group of energetic minima of band λ. For example, in direct-gap zincblende and wurtzite III-V and II-VI semiconductors, $\boldsymbol{k}_0 = \boldsymbol{0}$ and $u_{\lambda,\boldsymbol{k}_0}$ have the symmetry of angular momentum eigenstates [25, 29], while the band-gap energies $\epsilon_{\lambda,\boldsymbol{k}_0}$ must be provided by experiments. In this thesis, the lowest conduction (e), heavy- (hh), light-hole (lh), and spin-orbit split-off (so) band are considered explicitly. Each band is twice spin degenerate, resulting in a set of eight bands. The explicit representation of the resulting fully-coupled Luttinger Hamiltonian can be found in

Ref. [25].

Although the Löwdin renormalization [31] provides perturbation theory with a framework to include implications from remote bands, without taking them into account explicitly, an eight-band model is insufficient to describe the band structure of indirect semiconductors around the global energetic minima. This is due to the limited momentum range as a consequence of the perturbation around a single point. Much more than the eight bands used in this thesis are required to calculate a realistic band structure extending over the whole Brioullin zone [32].

Sometimes effects from band non-parabolicities are not of interest. It is then often useful to restrict the discussion to two bands and Eq. (2.10) does not have to be solved explicitly. Instead, it is sufficient to use Eq. (2.14) regarding a limited momentum range around the band minimum. Although the effective mass (2.15) depends on the momentum, it can be assumed constant around the band minima and is ultimately provided by experiments, which is fairly accurate concerning optics in semiconductor systems that are excited closely to the band gap. This approach is called effective-mass approximation. In this case, Eq. (2.15) decouples concerning λ so that $\boldsymbol{k}_0$ is a free parameter. While for direct semiconductors, $\boldsymbol{k}_0$ is identical for all λ, it differs in indirect materials since electrons and holes accumulate at different valleys. Then, $\boldsymbol{k}_0$ is effectively replaced by $\boldsymbol{k}_{0,\lambda}$, the group of global minima for band λ.

For direct semiconductors with cubic symmetry, all masses are isotropic [29], e.g. $m_{\lambda,1} = m_{\lambda,2} = m_{\lambda,3} \equiv m_\lambda$. In indirect semiconductors however, all masses can be different although the anisotropy is usually constrained to the conduction band. Yet, if the group of $\boldsymbol{k}_0$ contains at least a threefold axis, two of the three conduction band masses have the same value [30], a result obtained using group theory [20].

2.3.2 Semiconductor Heterostructures

The envelope-function approach [27, 33] is an excellent tool to find the band structure of semiconductor heterostructures. These structures can be considered mesoscopic since the QW's lateral extension is considerably larger than the lattice constant of the utilized materials, but small in comparison to the full sample. As a consequence, the electrons are confined within these regions and quantized along the growth direction of the crystal.

Therefore, the considerations of the previous Section can be repeated with the adjusted Bloch theorem

$$\phi_{\lambda,\nu,\boldsymbol{k}}(\boldsymbol{r}) = \frac{1}{\sqrt{L^2}}\, \mathrm{e}^{\mathrm{i}\boldsymbol{k}_\parallel \cdot \boldsymbol{r}_\parallel}\, \xi_{\lambda,\nu}(z)\, u_{\lambda,\nu,\boldsymbol{k}_\parallel}(\boldsymbol{r})\,, \tag{2.16}$$

containing the confinement function $\xi_{\lambda,\nu}$ characterized by a bulk band index λ and a subband index ν. Both the momentum and spatial coordinates have been decomposed into a component in growth direction of the crystal (k_z and z) and one perpendicular to it, e.g. within the QW plane ($\boldsymbol{k}_\parallel$ and $\boldsymbol{r}_\parallel$). The additional subband quantum number ν occurs due to the quantization in the growth

direction z.

Similar steps as in Section 2.3.1 yield the perturbative wave function using bulk states via

$$\xi_{\lambda,\nu}(z)\, u_{\lambda,\nu,\boldsymbol{k}_\parallel}(\boldsymbol{r}) = \sum_{\mu} \xi^{(\mu)}_{\lambda,\nu,\boldsymbol{k}_\parallel}(z)\, u_{\mu,\boldsymbol{k}_0}(\boldsymbol{r})\,. \tag{2.17}$$

Formally, $\xi^{(\mu)}_{\lambda,\nu,\boldsymbol{k}_\parallel}$ are the expansion coefficients in analogy to Eq. (2.12). However, they are sometimes called confinement functions as well.

A heterostructure system constitutes a spatial potential landscape V_λ for electrons and holes in the conduction ($\lambda = \mathrm{e}$) and valence ($\lambda \in \mathrm{h} \equiv \{\mathrm{hh}, \mathrm{lh}, \mathrm{so}\}$) bands [34]

$$V_{\lambda\in\mathrm{e(h)}}(z) = \epsilon_{\lambda,\boldsymbol{k}_0}(z) + V_{\mathrm{offset}}(z) \overset{-}{(+)} |e|\Phi(z)\,, \tag{2.18}$$

with contributions V_{offset} to account for the relative energetic alignment of adjacent layers. The screening potential Φ obeys the Poisson equation [35]

$$\frac{\mathrm{d}^2}{\mathrm{d}z^2}\Phi(z) = -\frac{|e|}{\epsilon_0 \epsilon_{\mathrm{BG}}(z)}\big(\rho_{\mathrm{h}}(z) - \rho_{\mathrm{e}}(z)\big)\,, \tag{2.19}$$

where the charge density distribution $\rho(z) = \rho_{\mathrm{h}}(z) - \rho_{\mathrm{e}}(z)$ has been decomposed into hole (ρ_{h}) and electron (ρ_{e}) contributions. Using the expansion (2.17), they read [36]

$$\rho_{\mathrm{h}}(z) = \frac{1}{\sqrt{L^2}} \sum_{\nu_{\mathrm{h}},\boldsymbol{k}_\parallel,\mu} \left|\xi^{(\mu)}_{\nu_{\mathrm{h}},\boldsymbol{k}_\parallel}(z)\right|^2 \left(1 - f^{\nu_{\mathrm{h}}}_{\boldsymbol{k}_\parallel}\right), \quad \rho_{\mathrm{e}}(z) = \frac{1}{\sqrt{L^2}} \sum_{\nu_{\mathrm{e}},\boldsymbol{k}_\parallel,\mu} \left|\xi^{(\mu)}_{\nu_{\mathrm{e}},\boldsymbol{k}_\parallel}(z)\right|^2 f^{\nu_{\mathrm{e}}}_{\boldsymbol{k}_\parallel}\,, \tag{2.20}$$

containing the carrier distribution

$$f^{\nu_\lambda}_{\boldsymbol{k}_\parallel} = \langle \hat{a}^\dagger_{\nu_\lambda,\boldsymbol{k}_\parallel} \hat{a}_{\nu_\lambda,\boldsymbol{k}_\parallel} \rangle\,. \tag{2.21}$$

Here, the notation $(\lambda, \nu) \equiv \nu_\lambda$ is introduced to label subbands directly according to their bulk affiliation. This is useful to emphasize a restriction of a specific subband to be either an occupied (electron) or unoccupied (hole) state.

2.4 Semiconductor Luminescence Equations

Once an excited system has reached a quasi-equilibrium state, the energy of the exciting light field is completely stored in its quantum fluctuations. Under these conditions, it is necessary to quantize the light field [12]. As a result, spontaneous emission of a photon from an excited semiconductor, known as luminescence, is a purely quantum-optical effect. One of the several forms of luminescence is PL, the light emission from any form of matter after the preceding absorption of electromagnetic radiation. In semiconductors, its origin is the radiative recombination of electron–hole

pairs. PL signals emerge from electronic transitions defined by the band structure of the system. Hence, it is an excellent tool to investigate the fundamental band gap of semiconductors [37, 38]. But device applications of PL are numerous. In phosphor thermometry, its temperature dependence is exploited to measure heat [39].

The most relevant quantity in the description of PL is the photon-number-like correlation

$$\mathcal{N}_{\boldsymbol{q}} = \Delta\langle \hat{b}^\dagger_{\boldsymbol{q}} \hat{b}_{\boldsymbol{q}} \rangle \ , \tag{2.22}$$

since it is proportional to the temporal change of the amount of photons. Here, $\hat{b}^\dagger_{\boldsymbol{q}}$ ($\hat{b}_{\boldsymbol{q}}$) is the creation (annihilation) operator of a photon with optical frequency $\omega_{\boldsymbol{q}} = c_0|\boldsymbol{q}|$. Via Eq. (2.8), the steady-state luminescence in the rotating-frame approximation can be found to be [40]

$$\mathrm{PL} = \frac{\partial}{\partial t}\mathcal{N}_{\boldsymbol{q}} = 2\frac{1}{L^2}\,\mathrm{Re}\left[\sum_{\lambda_\mathrm{e},\nu_\mathrm{h},\boldsymbol{k}_\parallel} \left(\mathcal{F}^{\lambda_\mathrm{e},\nu_\mathrm{h}}_{\boldsymbol{q}}\right)^\star \Pi^{\lambda_\mathrm{e},\nu_\mathrm{h}}_{\boldsymbol{k}_\parallel,\boldsymbol{q}}\right], \tag{2.23}$$

containing the coupling-matrix element $\mathcal{F}^{\lambda_\mathrm{e},\nu_\mathrm{h}}_{\boldsymbol{q}}$ and the photon-assisted polarization

$$\Pi^{\lambda_\mathrm{e},\nu_\mathrm{h}}_{\boldsymbol{k}_\parallel,\boldsymbol{q}} = \Delta\left\langle \hat{b}^\dagger_{\boldsymbol{q}} \hat{a}^\dagger_{\lambda_\mathrm{e},\boldsymbol{k}_\parallel} \hat{a}_{\nu_\mathrm{h},\boldsymbol{k}_\parallel} \right\rangle \ . \tag{2.24}$$

Equation (2.24) characterizes the emission of a photon under simultaneous recombination of an electron–hole pair. Explicit forms for $\mathcal{F}^{\lambda_\mathrm{e},\nu_\mathrm{h}}_{\boldsymbol{q}}$ can be found in Refs. [10] and [40]. The dynamics of Eq. (2.24) can again be obtained using the Heisenberg equation of motion (2.8), yielding

$$\mathrm{i}\hbar\frac{\partial}{\partial t}\Pi^{\lambda_\mathrm{e},\nu_\mathrm{h}}_{\boldsymbol{k}_\parallel,\boldsymbol{q}} = \left(\epsilon_{\lambda_\mathrm{e},\boldsymbol{k}_\parallel} - \epsilon_{\nu_\mathrm{h},\boldsymbol{k}_\parallel} - \hbar\omega_{\boldsymbol{q}}\right)\Pi^{\lambda_\mathrm{e},\nu_\mathrm{h}}_{\boldsymbol{k}_\parallel,\boldsymbol{q}} + \mathcal{W}^{\lambda_\mathrm{e},\nu_\mathrm{h}}_{\boldsymbol{q},\boldsymbol{k}_\parallel} - \left(1 - f^{\lambda_\mathrm{e}}_{\boldsymbol{k}_\parallel} - f^{\nu_\mathrm{h}}_{\boldsymbol{k}_\parallel}\right)\mathcal{U}^{\lambda_\mathrm{e},\nu_\mathrm{h}}_{\boldsymbol{q},\boldsymbol{k}_\parallel} \ . \tag{2.25}$$

Both the spontaneous-emission source $\mathcal{W}^{\lambda_\mathrm{e},\nu_\mathrm{h}}_{\boldsymbol{q},\boldsymbol{k}_\parallel}$ and the stimulated-emission source $\mathcal{U}^{\lambda_\mathrm{e},\nu_\mathrm{h}}_{\boldsymbol{q},\boldsymbol{k}_\parallel}$ depend on the level of approximation made concerning contributions from scattering. In this thesis, we treat these contributions on the second-Born level and in the Markov limit. The Markov limit explicitly neglects quantum-memory effects for the phonon interactions [41]. The second-Born approximation includes Coulomb effects up to quadratic order in the screened interaction potential for carrier many-body effects [42]. Resulting explicit representations of $\mathcal{W}^{\lambda_\mathrm{e},\nu_\mathrm{h}}_{\boldsymbol{q},\boldsymbol{k}_\parallel}$ and $\mathcal{U}^{\lambda_\mathrm{e},\nu_\mathrm{h}}_{\boldsymbol{q},\boldsymbol{k}_\parallel}$ can be found in Refs. [29] and [40].

2.5 Semiconductor Bloch Equations

Ideally, a coherent laser generates a light field which is very close to classical light [10]. Hence, it is not required to quantize the light field while investigating the absorption of a semiconductor system. Instead, it is sufficient to assume a coherent classical light source which is described via $\boldsymbol{E}(t) \equiv E(t)\boldsymbol{e}_\mathrm{P}$. It contains the polarization $\boldsymbol{e}_\mathrm{P}$ and acts at the position of the QW.

In order to determine the optical response of a many-body system to this classical light field, the microscopic interband polarization is introduced via $p^{\nu_\mathrm{h},\lambda_\mathrm{e}}_{\boldsymbol{k}_\parallel} = \langle \hat{a}^\dagger_{\nu_\mathrm{h},\boldsymbol{k}_\parallel} \hat{a}_{\lambda_\mathrm{e},\boldsymbol{k}_\parallel} \rangle$, which corresponds to the transition amplitude of an excitation process. Again, Eq. (2.8) can be employed to obtain the relevant dynamics, which read

$$\begin{aligned} \mathrm{i}\hbar \frac{\partial}{\partial t} p^{\nu_\mathrm{h},\lambda_\mathrm{e}}_{\boldsymbol{k}_\parallel} = & \sum_{\mu_\mathrm{e},\eta_\mathrm{h}} \left[\tilde{\epsilon}^\mathrm{e}_{\lambda_\mathrm{e},\mu_\mathrm{e}} \delta_{\nu_\mathrm{h},\eta_\mathrm{h}} + \tilde{\epsilon}^\mathrm{h}_{\nu_\mathrm{h},\eta_\mathrm{h}} \delta_{\lambda_\mathrm{e},\mu_\mathrm{e}} \right] p^{\eta_\mathrm{h},\mu_\mathrm{e}}_{\boldsymbol{k}_\parallel} \\ & - \left(1 - f^{\lambda_\mathrm{e}}_{\boldsymbol{k}_\parallel} - f^{\nu_\mathrm{h}}_{\boldsymbol{k}_\parallel} \right) \Omega^{\nu_\mathrm{e},\lambda_\mathrm{h}}_{\boldsymbol{k}_\parallel} + \mathrm{i}\hbar \Gamma^{\nu_\mathrm{h},\lambda_\mathrm{e}}_{\boldsymbol{k}_\parallel} , \end{aligned} \tag{2.26}$$

$$\frac{\partial}{\partial t} f^{\lambda_\mathrm{e}}_{\boldsymbol{k}_\parallel} = -\frac{2}{\hbar} \mathrm{Im} \left[\sum_{\nu_\mathrm{h}} \Omega^{\lambda_\mathrm{e},\nu_\mathrm{h}}_{\boldsymbol{k}_\parallel} \left(p^{\nu_\mathrm{h},\lambda_\mathrm{e}}_{\boldsymbol{k}_\parallel} \right)^\star \right] + \Gamma^{\lambda_\mathrm{e},\lambda_\mathrm{e}}_{\boldsymbol{k}_\parallel} , \tag{2.27}$$

$$\frac{\partial}{\partial t} f^{\nu_\mathrm{h}}_{\boldsymbol{k}_\parallel} = -\frac{2}{\hbar} \mathrm{Im} \left[\sum_{\lambda_\mathrm{e}} \Omega^{\lambda_\mathrm{e},\nu_\mathrm{h}}_{\boldsymbol{k}_\parallel} \left(p^{\nu_\mathrm{h},\lambda_\mathrm{e}}_{\boldsymbol{k}_\parallel} \right)^\star \right] + \Gamma^{\nu_\mathrm{h},\nu_\mathrm{h}}_{\boldsymbol{k}_\parallel} , \tag{2.28}$$

with the renormalized band energies

$$\tilde{\epsilon}^\mathrm{e}_{\lambda_\mathrm{e},\nu_\mathrm{e}} = \epsilon_{\lambda_\mathrm{e},\boldsymbol{k}_\parallel} \delta_{\lambda_\mathrm{e},\nu_\mathrm{e}} - \sum_{\mu_\mathrm{e},\boldsymbol{k}'_\parallel} V^{\lambda_\mathrm{e},\mu_\mathrm{e},\nu_\mathrm{e},\mu_\mathrm{e}}_{\boldsymbol{k}_\parallel - \boldsymbol{k}'_\parallel} f^{\mu_\mathrm{e}}_{\boldsymbol{k}_\parallel} , \tag{2.29}$$

$$\tilde{\epsilon}^\mathrm{h}_{\lambda_\mathrm{h},\nu_\mathrm{h}} = \epsilon_{\lambda_\mathrm{h},\boldsymbol{k}_\parallel} \delta_{\lambda_\mathrm{h},\nu_\mathrm{h}} - \sum_{\mu_\mathrm{h},\boldsymbol{k}'_\parallel} V^{\nu_\mathrm{h},\mu_\mathrm{h},\lambda_\mathrm{h},\mu_\mathrm{h}}_{\boldsymbol{k}_\parallel - \boldsymbol{k}'_\parallel} f^{\mu_\mathrm{h}}_{\boldsymbol{k}_\parallel} , \tag{2.30}$$

and the renormalized Rabi energy

$$\Omega^{\nu_\mathrm{e},\lambda_\mathrm{h}}_{\boldsymbol{k}_\parallel} = d^{\nu_\mathrm{e},\lambda_\mathrm{h}}_{\boldsymbol{k}_\parallel} E(t) + \sum_{\mu_\mathrm{e},\eta_\mathrm{h},\boldsymbol{k}'_\parallel} V^{\lambda_\mathrm{e},\eta_\mathrm{h},\nu_\mathrm{h},\mu_\mathrm{e}}_{\boldsymbol{k}_\parallel - \boldsymbol{k}'_\parallel} p^{\eta_\mathrm{h},\mu_\mathrm{e}}_{\boldsymbol{k}_\parallel} . \tag{2.31}$$

The scattering terms $\Gamma^{\lambda,\nu}_{\boldsymbol{k}_\parallel}$ in Eqs. (2.26)–(2.28) which constitute the semiconductor Bloch equations (SBEs), are again treated in second Born approximation and the Markov limit. Explicit versions can be found in Refs. [29, 43]. Equations (2.29)-(2.31) also contain the dipole-matrix element

$$d^{\lambda_\mathrm{e},\nu_\mathrm{h}}_{\boldsymbol{k}_\parallel} = \frac{\mathrm{i}e}{m_0 \left(\epsilon_{\lambda_\mathrm{e},\boldsymbol{k}_\parallel} - \epsilon_{\nu_\mathrm{h},\boldsymbol{k}_\parallel} \right)} \sum_{\mu,\kappa} \int_{-\infty}^{\infty} \mathrm{d}z \left[\xi^{(\mu)}_{\lambda_\mathrm{e},\boldsymbol{k}_\parallel}(z) \right]^\star \left[\delta_{\mu,\kappa} \hbar \boldsymbol{k}_\parallel + \boldsymbol{p}_{\mu,\kappa} \right] \cdot \boldsymbol{e}_\mathrm{P} \, \xi^{(\kappa)}_{\nu_\mathrm{h},\boldsymbol{k}_\parallel}(z) , \tag{2.32}$$

and the Coulomb-matrix element

$$\begin{aligned} V^{\lambda_j,\nu_l,\mu_m,\eta_n}_{\boldsymbol{k}_\parallel} = & \frac{e^2}{2\epsilon_0 \epsilon_\mathrm{BG} \left| \boldsymbol{k}_\parallel \right| L^2} \\ & \times \sum_{\mu,\kappa} \iint_{-\infty}^{\infty} \mathrm{d}z \, \mathrm{d}z' \left[\xi^{(\mu)}_{\lambda_j,\boldsymbol{k}_\parallel}(z) \xi^{(\kappa)}_{\nu_l,\boldsymbol{k}_\parallel}(z') \right]^\star \mathrm{e}^{-\left| \boldsymbol{k}_\parallel (z-z') \right|} \xi^{(\kappa)}_{\mu_m,\boldsymbol{k}_\parallel}(z') \xi^{(\mu)}_{\eta_n,\boldsymbol{k}_\parallel}(z) , \end{aligned} \tag{2.33}$$

both using the expansion (2.17).

2.5.1 Bulk Semiconductors

In some parts of this thesis, the SBEs for bulk semiconductors are required. Although the differences are marginal, they are given here for completeness. Within the scope of this thesis, a two band model is considered.

A restriction to the bulk e and hh bands yields the dynamics of the macroscopic polarization $p_{\boldsymbol{k}} \equiv \left\langle a^{\dagger}_{\mathrm{hh},\boldsymbol{k}} a_{\mathrm{e},\boldsymbol{k}} \right\rangle$ and carrier distributions $f^{\mathrm{e(hh)}}_{\boldsymbol{k}} = \left\langle a^{\dagger}_{\mathrm{e(hh)},\boldsymbol{k}} a_{\mathrm{e(hh)},\boldsymbol{k}} \right\rangle$, which read

$$\mathrm{i}\hbar \frac{\partial}{\partial t} p_{\boldsymbol{k}} = \tilde{\epsilon}_{\boldsymbol{k}} + \left(1 - f^{\mathrm{e}}_{\boldsymbol{k}} - f^{\mathrm{hh}}_{\boldsymbol{k}}\right) \Omega_{\boldsymbol{k}} + \mathrm{i}\hbar \Gamma^{\mathrm{hh,e}}_{\boldsymbol{k}} , \tag{2.34}$$

$$\frac{\partial}{\partial t} f^{\mathrm{e}}_{\boldsymbol{k}} = -\frac{2}{\hbar} \mathrm{Im}\left[\Omega_{\boldsymbol{k}} \left(p_{\boldsymbol{k}}\right)^{\star}\right] + \Gamma^{\mathrm{e,e}}_{\boldsymbol{k}} , \tag{2.35}$$

$$\frac{\partial}{\partial t} f^{\mathrm{hh}}_{\boldsymbol{k}} = -\frac{2}{\hbar} \mathrm{Im}\left[\Omega_{\boldsymbol{k}} \left(p_{\boldsymbol{k}}\right)^{\star}\right] + \Gamma^{\mathrm{hh,hh}}_{\boldsymbol{k}} , \tag{2.36}$$

containing the renormalized band dispersion $\tilde{\epsilon}_{\boldsymbol{k}} = \epsilon_{\mathrm{e},\boldsymbol{k}} - \epsilon_{\mathrm{hh},\boldsymbol{k}} - \sum_{\boldsymbol{k}'} V_{\boldsymbol{k}-\boldsymbol{k}'} \left(f^{\mathrm{e}}_{\boldsymbol{k}'} + f^{\mathrm{hh}}_{\boldsymbol{k}'}\right)$ and scattering terms $\Gamma^{\lambda,\nu}_{\boldsymbol{k}}$. The renormalized Rabi energy is given by

$$\Omega_{\boldsymbol{k}} = d_{\boldsymbol{k}} E(t) + \sum_{\boldsymbol{k}'} V_{\boldsymbol{k}-\boldsymbol{k}'} p_{\boldsymbol{k}'} , \tag{2.37}$$

containing the Coulomb potential

$$V_{\boldsymbol{q}} = \frac{e^2}{\epsilon_{\mathrm{BG}}\, \epsilon_0\, L^3} \frac{1}{q^2} , \tag{2.38}$$

which is the Fourier transform of Eq. (2.4), and the interband dipole matrix element $d_{\boldsymbol{k}} = d^{\mathrm{e,hh}}_{\boldsymbol{k}}$ with

$$d^{\lambda,\nu}_{\boldsymbol{k}} = \left\langle \lambda \boldsymbol{k} \middle| \left(-|e|\boldsymbol{r}\right) \middle| \nu \boldsymbol{k} \right\rangle = \frac{\mathrm{i}\hbar|e|}{m_0} \frac{\boldsymbol{p}_{\lambda,\nu}(\boldsymbol{k})}{\epsilon_{\lambda,\boldsymbol{k}} - \epsilon_{\nu,\boldsymbol{k}}} . \tag{2.39}$$

2.6 Inhomogeneous Broadening

If the hierarchy problem is truncated at the level of the second-Born approximation, only homogeneous broadening effects are taken into account explicitly. However, realistic semiconductors are subject to other mechanisms that may contribute to the absorption or PL line shape. Most commonly, these are local fluctuations of the band gap due to small composition inhomogeneities, layer thickness variations, or disorder. To account for these effects, a homogeneous response $S(E = \hbar\omega, 0)$ can be convoluted with a Gaussian to obtain the inhomogeneously broadened

one by

$$S(E,\Delta) = \frac{2\sqrt{\ln(2)}}{\Delta\sqrt{\pi}} \int_0^\infty \mathrm{d}E'\, S(E',0) \exp\left[-\frac{4\ln(2)\left(E-E'\right)^2}{\Delta^2}\right], \tag{2.40}$$

which is characterized by the full width at half maximum (FWHM) Δ.

2.7 Optical Absorption

Computing the dynamics of specific quantities outlined previously is motivated by their suitability to calculate the optical response of semiconductor systems. The used microscopic many-body approach simultaneously allows to examine interactions on the scale of fundamental particles. Optically accessible quantities can be modeled via macroscopic properties derived from their microscopic counterparts. While PL has already been discussed in Section 2.4, this Section focuses on linear and nonlinear absorption.

The response of an excited semiconductor is determined by the macroscopic polarization

$$P(t) = \frac{1}{L^2}\frac{1}{d_{\mathrm{QW}}} \sum_{\lambda_\mathrm{e},\nu_\mathrm{h},\boldsymbol{k}_\parallel} p_{\boldsymbol{k}_\parallel}^{\nu_\mathrm{h},\lambda_\mathrm{e}} \left[d_{\boldsymbol{k}_\parallel}^{\lambda_\mathrm{e},\nu_\mathrm{h}}\right]^\star + \mathrm{c.c.}\,, \tag{2.41}$$

$$P(t) = \frac{1}{L^3} \sum_{\boldsymbol{k}} p_{\boldsymbol{k}}\, d_{\boldsymbol{k}}^\star + \mathrm{c.c.}\,, \tag{2.42}$$

for QWs and bulk materials, respectively. Here, $d_{\mathrm{QW}} = \sum_j l_j$ is the lateral extension of a multi QW structure consisting of active layers with lengths l_j.

When a transverse electric field is applied to a sample, the optical response is also determined by the transverse dielectric function [44–46],

$$\epsilon_\mathrm{T}(\omega) = \epsilon_\mathrm{BG} + \chi(\omega)\,. \tag{2.43}$$

It contains the electric susceptibility χ, which relates the macroscopic polarization P to the semiclassical electric field E via

$$P(\omega) = \epsilon_0 \chi(\omega) E(\omega)\,. \tag{2.44}$$

In more complicated QW structures such as the "W"-Laser [47–50], ϵ_BG is determined by averaging over the active regions, e.g.

$$\epsilon_\mathrm{BG} = \frac{1}{d_{\mathrm{QW}}} \sum_j \epsilon_{\mathrm{BG},j}\, l_j\,, \tag{2.45}$$

with $\epsilon_{\mathrm{BG},j}$ being the background relative permittivity of the j-th optically active layer.

The absorption of a QW heterostructure as an experimentally accessible property is related to the electric susceptibility via [10]

$$\alpha(\omega) = 1 - \left|R(\omega)\right|^2 - \left|T(\omega)\right|^2 = \frac{2\,\mathrm{Im}\left[\xi(\omega)\right]}{1 + \left|\xi(\omega)\right|^2 + 2\,\mathrm{Im}\left[\xi(\omega)\right]}\,, \tag{2.46}$$

where ξ is the scaled susceptibility

$$\xi(\omega) = \frac{\omega}{2\sqrt{\epsilon_{\mathrm{BG}}}c_0}\chi(\omega)\,. \tag{2.47}$$

The reflectance and transmission coefficients are given by [10]

$$R(\omega) = \frac{\mathrm{i}\xi(\omega)}{1 - \mathrm{i}\xi(\omega)}\,, \tag{2.48}$$

$$T(\omega) = \frac{1}{1 - \mathrm{i}\xi(\omega)}\,. \tag{2.49}$$

If we assume that both $\left|\xi(\omega)\right|^2$ and $\mathrm{Im}\left[\xi(\omega)\right]$ are small, Eq. (2.46) reduces to

$$\alpha(\omega) \approx 2\,\mathrm{Im}\left[\xi(\omega)\right] = \frac{\omega}{\sqrt{\epsilon_{\mathrm{BG}}}c_0}\,\mathrm{Im}\left[\chi(\omega)\right]. \tag{2.50}$$

2.8 Wannier Equation

The incoherent limit describes a quasi-equilibrium configuration in which carriers have been excited by a preceding light pulse and decayed into a thermal state. This means that this state is characterized by a temperature T and sufficiently described by a Fermi–Dirac distribution,

$$f_{\boldsymbol{k}}^{\lambda} = \frac{1}{\exp\left[\beta\left(\epsilon_{\lambda,\boldsymbol{k}} - \mu_{\lambda}\right)\right] + 1}\,, \qquad \beta^{-1} = k_{\mathrm{B}}T\,, \tag{2.51}$$

containing the chemical potential μ_{λ}.

Having eliminated the time dependence for the carrier distributions in the SBEs, the differential equation for the polarization (2.34) becomes homogenous, since the driving field has already been decayed in the incoherent limit. Thus, the homogeneous solution ψ_{λ} constitutes an eigenvalue problem for the exciton wave function and binding energies E_{λ} known as the generalized Wannier equation [51]

$$E_{\lambda}\,\psi_{\lambda}^{\mathrm{R}}\left(\boldsymbol{k}\right) = \tilde{\epsilon}_{\boldsymbol{k}}\,\psi_{\lambda}^{\mathrm{R}}\left(\boldsymbol{k}\right) - \left(1 - f_{\boldsymbol{k}}^{\mathrm{e}} - f_{\boldsymbol{k}}^{\mathrm{h}}\right)\sum_{\boldsymbol{k}'} V_{\boldsymbol{k}-\boldsymbol{k}'}\,\psi_{\lambda}^{\mathrm{R}}\left(\boldsymbol{k}'\right). \tag{2.52}$$

For non-vanishing carrier distributions, Eq. (2.52) is non-Hermitian thus having both left- ($\psi_{\lambda}^{\mathrm{L}}$)

and right-handed ($\psi^{\mathrm{R}}_{\lambda}$) solutions. The corresponding left-handed equation reads [52]

$$\left[\psi^{\mathrm{L}}_{\lambda}(\boldsymbol{k})\right]^{\star} E_{\lambda} = \left[\psi^{\mathrm{L}}_{\lambda}(\boldsymbol{k})\right]^{\star} \tilde{\epsilon}_{\boldsymbol{k}} - \sum_{\boldsymbol{k}'} \left[\psi^{\mathrm{L}}_{\lambda}(\boldsymbol{k}')\right]^{\star} \left(1 - f^{\mathrm{e}}_{\boldsymbol{k}'} - f^{\mathrm{h}}_{\boldsymbol{k}'}\right) V_{\boldsymbol{k}-\boldsymbol{k}'}\,, \tag{2.53}$$

and both solutions are related via [10]

$$\psi^{\mathrm{L}}_{\lambda}(\boldsymbol{k}) = \frac{\psi^{\mathrm{R}}_{\lambda}(\boldsymbol{k})}{1 - f^{\mathrm{e}}_{\boldsymbol{k}} - f^{\mathrm{h}}_{\boldsymbol{k}}}\,. \tag{2.54}$$

Although Eqs. (2.52) and (2.53) assume $\Gamma^{\mathrm{hh,e}}_{\boldsymbol{k}} = 0$, dephasing mechanisms can be included microscopically. As an example, Coulomb correlated effects such as EID [28, 51] may be included via complex scattering matrices [53]. Then, Equation (2.54) is no longer valid and Eqs. (2.52) and (2.53) must be solved simultaneously.

The wave functions obey the orthogonalization and completeness relation [52]

$$\sum_{\boldsymbol{k}} \left[\psi^{\mathrm{L}}_{\lambda}(\boldsymbol{k})\right]^{\star} \psi^{\mathrm{R}}_{\nu}(\boldsymbol{k}) = \delta_{\lambda,\nu}\,, \tag{2.55}$$

$$\sum_{\lambda} \left[\psi^{\mathrm{L}}_{\lambda}(\boldsymbol{k})\right]^{\star} \psi^{\mathrm{R}}_{\lambda}(\boldsymbol{k}') = \delta_{\boldsymbol{k},\boldsymbol{k}'}\,. \tag{2.56}$$

For vanishing carrier densities, Eq. (2.52) resembles the Schrödinger equation for the relative motion of a hydrogen-like atom [12]. However, differences in the particle masses and dielectric constants yield binding energies which differ by about 3 orders of magnitude. While the hydrogen binding energy depends on the bare electron mass m_0 and has a well known absolute value of 13.6 eV [54], the exciton counterpart in common semiconductors is usually in the order of 1 – 20 meV [55]. Covering the energy range of a few meV is what makes THz spectroscopy an especially qualified tool to identify and study excitonic effects in semiconductors [56].

2.9 Linear THz Spectroscopy

That part of the system Hamiltonian (2.1) that governs the interaction of carriers and a weak classical THz field $\boldsymbol{A}_{\mathrm{THz}} \equiv A_{\mathrm{THz}}(t)\boldsymbol{e}_A$ reads [10]

$$H_{\mathrm{THz}} = -\sum_{\lambda,\boldsymbol{k}} \boldsymbol{j}_{\lambda,\boldsymbol{k}} \cdot \boldsymbol{A}_{\mathrm{THz}}(t)\, a^{\dagger}_{\lambda,\boldsymbol{k}} a_{\lambda,\boldsymbol{k}}\,. \tag{2.57}$$

The field's polarization is labeled $\boldsymbol{e}_A$ while the current-matrix element is given by [6]

$$\boldsymbol{j}_{\lambda,\boldsymbol{k}} = -\frac{e}{\hbar} \nabla_{\boldsymbol{k}} \epsilon_{\lambda,\boldsymbol{k}}\,. \tag{2.58}$$

As a measure of the overlap of the participating exciton states, transitions are mediated via the transition-matrix element [57]

$$J_{\lambda,\nu} = \sum_{\boldsymbol{k}} \left[\psi_{\lambda}^{\mathrm{L}}(\boldsymbol{k})\right]^{\star} j(\boldsymbol{k})\, \psi_{\nu}^{\mathrm{R}}(\boldsymbol{k})\,, \tag{2.59}$$

containing the reduced current

$$j(\boldsymbol{k}) = \sum_{\lambda} \boldsymbol{j}_{\lambda,\boldsymbol{k}} \cdot \boldsymbol{e}_{\mathrm{p}}\,. \tag{2.60}$$

Finally, the absorption follows from the THz-Elliott formula [10]

$$\alpha_{\mathrm{THz}}(\omega) = \mathrm{Im}\left[\sum_{\lambda,\nu} \frac{S_{\lambda,\nu}(\omega)\Delta n_{\lambda,\nu} - \left[S_{\lambda,\nu}(-\omega)\Delta n_{\lambda,\nu}\right]^{\star}}{\epsilon_0\sqrt{\epsilon_{\mathrm{BG}}}\, c_0 \omega\left(\hbar\omega + \mathrm{i}\gamma_J\right)}\right], \tag{2.61}$$

with the response function

$$S_{\lambda,\nu}(\omega) = \sum_{\beta} \frac{\left(E_{\beta} - E_{\lambda}\right) J_{\lambda,\beta}\, J_{\beta,\nu}}{E_{\beta} - E_{\lambda} - \hbar\omega - \mathrm{i}\gamma}\,, \tag{2.62}$$

and the total density of exciton correlations $\Delta n_{\lambda,\nu}$, which generally includes both exciton and free carrier contributions [58]. The phenomenological damping constant of the exciton correlations (THz current) is labeled γ (γ_J).

3 Effects of Mass Anisotropy on the Optical Properties of Semiconductors

One of the most fascinating organizing principles in quantum many-body physics is the formation of quasiparticles. As such, an electron in a periodic potential kinetically behaves as if moved through free space but with a modified mass. The recently discovered dropleton [59] consists of collectively bound electron–hole complexes and is characterized by a pair-correlation function identical to that of a liquid [60]. In turn, quasiparticles can modify a semiconductor's optical response making them an excellent phenomenon to test our understanding of quantum mechanics with spectroscopical techniques.

The formation of a bound state consisting of an electron and a hole via the attractive Coulomb interaction is known as an exciton and qualifies as one of the most fundamental excitations in semiconductors [61]. This energetically favorable state in excited semiconductors has been studied extensively in material systems such as GaAs [62–65], where the electrons' effective mass is isotropic [66], i.e. does not depend on the direction of motion. In this Chapter, the description of the exciton wavefunction is extended to systems where the electrons' effective mass is anisotropic, e.g. varies concerning different crystal momentum paths. To confirm its validity, it is applied to calculate the THz absorption in Ge and Si. It will also be used to obtain the near-bandgap excitonic optical absorption of titanium dioxide (TiO_2) in rutile configuration.

3.1 THz Spectroscopy of Bulk Germanium

The energetic width of THz radiation roughly covers the range of $1 - 15\,\mathrm{meV}$, making THz spectroscopy a uniquely qualified method to investigate inter-molecular vibrations [67], high-harmonic generation [68], transient photoconductivity [69], or transition energies of exciton eigenstates in quantum many-body systems [70–72]. Especially excitons take an important role in both optical and THz spectroscopy of semiconductors. As an experimentally directly observable quantity, transition energies between exciton states critically depend on effective electron and hole masses. THz excitation dynamics and spectra of many direct-gap semiconductors have been investigated by both theoretical [73–76] and experimental [77–80] means. In these systems, exciton properties can be obtained even analytically [73, 74].

Effective carrier masses in indirect semiconductors are often anisotropic. Although excitons have been observed in such systems, e.g. in Ge [81] or Si [82], this has been done by means of THz

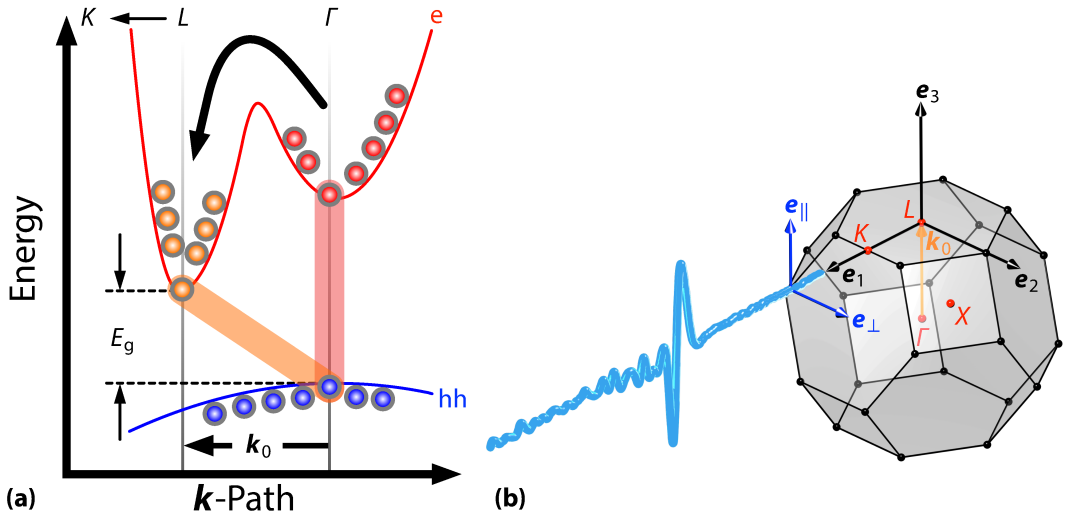

Figure 3.1 — (a) Schematic band diagram and exciton formation in Ge. Assuming that electrons are optically excited at the Γ point (red circles) in the conduction band (e) and holes (blue dots) in the heavy-hole (hh) band, a direct coherent polarization (red-shaded area) is generated. After the electrons have been scattered into the band minimum at the L valley (orange circles), the coherent excitons decay into incoherent correlations which may contain indirect incoherent excitons (orange-shaded area). (b) Schematic of the first Brillouin zone of a cubic semiconductor addressed by a THz pulse (light blue) propagating along the $\boldsymbol{e}_1$ axis. The vector separating the Γ and L points is denoted by $\boldsymbol{k}_0$ (orange). In contrast to Ge, $\boldsymbol{k}_0$ would point from the Γ into the direction of the X point in Si. Several points of high symmetry are marked (red spheres). The pulse polarization (dark blue) is aligned either be parallel ($\boldsymbol{e}_\parallel$) or perpendicular ($\boldsymbol{e}_\perp$) to $\boldsymbol{e}_3$.

spectroscopy only recently [83, 84]. Finding an analytical solution considering many-body effects is almost impossible and numerical solvers must be employed. The development of a numerical scheme for systems with strong mass anisotropy is the subject of this Section.

3.1.1 Generalized Wannier Equation with Mass Anisotropy

In indirect semiconductors, the valence band maximum and the conduction band minimum are not aligned in momentum space ($\boldsymbol{k}_{0,\mathrm{e}} \neq \boldsymbol{k}_{0,\mathrm{hh}} = \boldsymbol{0}$), as depicted in Fig. 3.1(a) for Ge. To find the consequential modifications to the generalized Wannier equation (2.52), transitions between two different momenta must be permitted. Therefore, the equation of motion of the general interband polarization $p_{\boldsymbol{k},\boldsymbol{k}'} = \left\langle a^\dagger_{\mathrm{hh},\boldsymbol{k}} a_{\mathrm{e},\boldsymbol{k}'} \right\rangle$ in analogy to Section 2.8 needs to be determined. The homogenous solution then constitutes an eigenvalue problem for the exciton wavefunction involving two

particles having different momenta and reads

$$E_\lambda\,\psi_\lambda^{\mathrm{R}}\big(\boldsymbol{k},\boldsymbol{k}'\big)=\tilde{\epsilon}_{\boldsymbol{k},\boldsymbol{k}'}\,\psi_\lambda^{\mathrm{R}}\big(\boldsymbol{k},\boldsymbol{k}'\big)-\Big(1-f_{\boldsymbol{k}'}^{\mathrm{e}}-f_{\boldsymbol{k}}^{\mathrm{h}}\Big)\sum_{\boldsymbol{q}}V_{\boldsymbol{q}}\,\psi_\lambda^{\mathrm{R}}\big(\boldsymbol{k}-\boldsymbol{q},\boldsymbol{k}'-\boldsymbol{q}\big)\,. \tag{3.1}$$

The appropriate renormalized band dispersion is given by

$$\tilde{\epsilon}_{\boldsymbol{k},\boldsymbol{k}'}=\epsilon_{\mathrm{e},\boldsymbol{k}'}-\epsilon_{\mathrm{hh},\boldsymbol{k}}-\sum_{\boldsymbol{q}}V_{\boldsymbol{q}}\Big(f_{\boldsymbol{k}'-\boldsymbol{q}}^{\mathrm{e}}+f_{\boldsymbol{k}-\boldsymbol{q}}^{\mathrm{h}}\Big)\,. \tag{3.2}$$

The discussion will be restricted on bulk semiconductors so that the Fourier transform of the Coulomb potential is given by Eq. (2.38).

In quasi-equilibrium, electrons accumulate around $\boldsymbol{k}_{0,\mathrm{e}}\equiv\boldsymbol{k}_0$ while holes usually are aggregated around the Γ valley, e.g. $\boldsymbol{k}_{0,\mathrm{hh}}=\boldsymbol{0}$. Hence, $\boldsymbol{k}_0$ is the separation between the band extrema. In the following, only diagonal excitons where $\boldsymbol{k}'=\boldsymbol{k}+\boldsymbol{k}_0$ are considered. With this assumption, Eq. (3.1) reduces to the usual Wannier equation (2.52), while the renormalized band structure is given by

$$\begin{aligned}\tilde{\epsilon}_{\boldsymbol{k}}&=\epsilon_{\mathrm{e},\boldsymbol{k}+\boldsymbol{k}_0}-\epsilon_{\mathrm{hh},\boldsymbol{k}}-\sum_{\boldsymbol{k}'}V_{\boldsymbol{k}-\boldsymbol{k}'}\Big(f_{\boldsymbol{k}'}^{\mathrm{e}}+f_{\boldsymbol{k}'}^{\mathrm{h}}\Big)\\&=E_{\mathrm{g}}+\sum_{j=1}^{3}\frac{\hbar^2}{2\mu_j}\Big[\boldsymbol{k}\cdot\boldsymbol{e}_j\Big]^2-\sum_{\boldsymbol{k}'}V_{\boldsymbol{k}-\boldsymbol{k}'}\Big(f_{\boldsymbol{k}'}^{\mathrm{e}}+f_{\boldsymbol{k}'}^{\mathrm{h}}\Big)\,,\end{aligned} \tag{3.3}$$

introducing the reduced effective masses $\mu_j^{-1}=m_{\mathrm{e},j}^{-1}+m_{\mathrm{hh},j}^{-1}$ and the band gap $E_{\mathrm{g}}=\epsilon_{\mathrm{e},\boldsymbol{k}_0}-\epsilon_{\mathrm{hh},\boldsymbol{0}}$.

Next, the numerical effort can be reduced by explicitly accounting for the angle dependence within the generalized Wannier equation. An efficient approach is to project Eq. (3.1) onto spherical harmonics,

$$\begin{aligned}\int\mathrm{d}\Omega\left[Y_l^m(\Omega)\right]^\star E_\lambda\,\psi_\lambda^{\mathrm{R}}\big(\boldsymbol{k}\big)=&\int\mathrm{d}\Omega\left[Y_l^m(\Omega)\right]^\star\tilde{\epsilon}_{\boldsymbol{k}}\,\psi_\lambda^{\mathrm{R}}\big(\boldsymbol{k}\big)\\&-\Big(1-f_k^{\mathrm{e}}-f_k^{\mathrm{h}}\Big)\underbrace{\int\mathrm{d}\Omega\left[Y_l^m(\Omega)\right]^\star\sum_{\boldsymbol{k}'}V_{\boldsymbol{k}-\boldsymbol{k}'}\,\psi_\lambda^{\mathrm{R}}\big(\boldsymbol{k}'\big)}_{\equiv I_k}\,,\end{aligned} \tag{3.4}$$

where radially symmetric carrier distributions $f_{\boldsymbol{k}}=f_k$ have been assumed. In terms of angles, it is $\Omega=\big(\theta,\varphi\big)$ and $\int\mathrm{d}\Omega=\int_0^{2\pi}\mathrm{d}\varphi\int_0^{\pi}\sin\theta\,\mathrm{d}\theta$. The appearing integrals can be solved if the wavefunction is expanded into a linear combination of spherical harmonics Y_l^m,

$$\psi_\lambda^{\mathrm{R}}\big(\boldsymbol{k}\big)=\sum_{l=0}^{\infty}\sum_{m=-l}^{l}R_{\lambda,l,m}\big(k\big)\,Y_l^m\big(\theta,\varphi\big)\,, \tag{3.5}$$

which is valid since they constitute an orthonormal basis. If the carrier distributions cannot be assumed to be radially symmetric, they also need to be expanded into a series of spherical harmonics similar to Eq. (3.5). However, this issue goes beyond the scope of this thesis.

A wavefunction's dominant character may be defined via that pair $\{l, m\}$ which produces the largest value for the expression

$$C_{\lambda,l,m} \equiv \sum_{\boldsymbol{k}} \left| R_{\lambda,l,m}(k)\, Y_l^m(\theta,\varphi) \right|^2 . \tag{3.6}$$

Equation (3.6) is a measure for the individual contributions from different angular momentum eigenstates. Any wavefunction can then be uniquely labeled by $\{\nu, l, m\}$ according to its dominant character $\{l, m\}$ and a principal quantum number $\nu = \{1, 2, 3, \dots\}$. Instead of a single label $\lambda = \{1, 2, 3, \dots\}$, this notation also reflects symmetry information and allows to use the usual notation for complex-valued atomic orbitals $\{1,0,0\} \equiv 1s$, $\{2,1,-1\} \equiv 2p_{-1}$, $\{2,1,0\} \equiv 2p_0$, $\{2,1,1\} \equiv 2p_1$, $\{2,0,0\} \equiv 2s$, and so on.

One representation of the spherical harmonics is given by [85]

$$Y_l^m(\theta,\varphi) = (-1)^m \alpha_l^m P_l^m(\cos\theta)\, \mathrm{e}^{\mathrm{i}m\varphi}, \qquad \alpha_l^m = \sqrt{\frac{(2l+1)(l-m)!}{4\pi(l+m)!}}, \tag{3.7}$$

where the phase factor $(-1)^m$ is chosen **not** to be included in the associated Legendre polynomials

$$P_l^m(x) = \sqrt{(1-x^2)^m}\, \frac{\mathrm{d}^m}{\mathrm{d}x^m} P_l(x), \tag{3.8}$$

which contain the Legendre polynomials P_l. This choice is also known as the Condon–Shortley sign convention [86].

In a system with isotropic masses, all integrals in Eq. (3.4) except I_k are easily solved due to the orthogonality of the spherical harmonics [87],

$$\int \mathrm{d}\Omega \left[Y_l^m(\Omega) \right]^\star Y_{l'}^{m'}(\Omega) = \delta_{l,l'}\, \delta_{m,m'} . \tag{3.9}$$

After inserting the expansion (3.5), I_k reads

$$I_k = \sum_{l=0}^{\infty} \sum_{m=-l}^{l} \int_0^\infty \mathrm{d}k' \left(k'\right)^2 R_{\lambda,l,m}(k') \underbrace{\int \mathrm{d}\Omega' \left(\frac{L}{2\pi}\right)^3 V_{\boldsymbol{k}-\boldsymbol{k}'}\, Y_l^m(\Omega')}_{\equiv \mathcal{I}_{k,k'}}, \tag{3.10}$$

if the vectorial sum is replaced by an integral [8], $\sum_{\boldsymbol{k}} \to \left(\frac{L}{2\pi}\right)^3 \int \mathrm{d}^3k$, which is then implemented in spherical coordinates. In attempt to solve $\mathcal{I}_{k,k'}$, the Fourier transformed Coulomb potential needs to be expressed via

$$V_{\boldsymbol{k}-\boldsymbol{k}'} = \frac{1}{L^3} \int_0^\infty \mathrm{d}^3r\, V(\boldsymbol{r})\, \mathrm{e}^{-\mathrm{i}\boldsymbol{k}\cdot\boldsymbol{r}} \mathrm{e}^{\mathrm{i}\boldsymbol{k}'\cdot\boldsymbol{r}} . \tag{3.11}$$

The plane-wave expansion [88, 89],

$$\mathrm{e}^{-\mathrm{i}\boldsymbol{k}\cdot\boldsymbol{r}} = 4\pi \sum_{l=0}^{\infty} \sum_{m=-l}^{l} (-\mathrm{i})^l j_l^\star\big(kr\big)\big[Y_l^m(\Omega)\big]^\star Y_l^m(\Theta)\,, \tag{3.12}$$

contains the spherical Bessel functions j_l while $\boldsymbol{r} = (r, \Theta)$ with $\Theta = \big(\vartheta, \phi\big)$ is the position-vector coordinate in spherical coordinates. Equations (3.11) and (3.12) can be used to obtain

$$\mathcal{I}_{k,k'} = Y_l^m(\Omega)\, \mathcal{V}_{k,k'}^l\,, \tag{3.13}$$

$$\mathcal{V}_{k,k'}^l = \frac{2}{\pi} \int_0^\infty \mathrm{d}r\, r^2\, V(r)\, j_l^\star\big(kr\big)\, j_l\big(k'r\big)\,. \tag{3.14}$$

Equation (3.14) only depends on the absolute values of the wave vectors and the azimuthal quantum number l.

On the other hand, Eq. (3.13) yields

$$\mathcal{V}_{k,k'}^l = \int \mathrm{d}\Omega' \left(\frac{L}{2\pi}\right)^3 V_{\boldsymbol{k}-\boldsymbol{k}'} \frac{Y_l^m(\Omega')}{Y_l^m(\Omega)}\,, \tag{3.15}$$

where the right-hand side is known to be independent of m and Ω, see Eq. (3.14). Therefore, their values can be chosen to be most convenient, e.g. $m = 0$ and $\theta = \varphi = 0$. With the help of Eq. (2.3), it follows that

$$\mathcal{V}_{k,k'}^l = \frac{e^2}{4\pi^2 \epsilon_0 \epsilon_{\mathrm{BG}}} \int_0^\pi \mathrm{d}\theta' \, \frac{\sin\theta'\, P_l\big(\cos\theta'\big)}{k^2 + \big(k'\big)^2 - 2kk'\cos\theta'}\,. \tag{3.16}$$

This representation is beneficial mostly due to numerical reasons, since no additional grid for the spatial coordinate is required, contrary to Eq. (3.14).

Without radial symmetry, the projection of the kinetic part of the Wannier equation in Eq. (3.4) produces integrals of the type

$$I_{1/2} = \int_0^\pi \mathrm{d}\theta\, \sin^3\theta\, P_{l'}^m\big(\cos\theta\big)\, P_l^m\big(\cos\theta\big)\,, \qquad I_3 = \int_0^\pi \mathrm{d}\theta\, \sin\theta\, \cos^2\theta\, P_{l'}^m\big(\cos\theta\big)\, P_l^m\big(\cos\theta\big)\,, \tag{3.17}$$

resulting from the components of the wave vector in spherical coordinates. They can be solved using the recurrence formula for the associated Legendre polynomials [90].

The final radial eigenvalue equation reads

Anisotropic Radial Wannier Equation

$$\tilde{E}_\lambda R_{\lambda,l,m}(k) = \left[\varepsilon^{(1)}_{l,m,k} - \int_0^\infty \mathrm{d}k' \left(k'\right)^2 \mathcal{V}^l_{k,k'}\left(f^{\mathrm{e}}_{k'} + f^{\mathrm{h}}_{k'}\right)\right] R_{\lambda,l,m}(k) + \varepsilon^{(2)}_{l-2,m,k} R_{\lambda,l-2,m}(k)$$
$$+\varepsilon^{(2)}_{l,m,k} R_{\lambda,l+2,m}(k) + c_{\lambda,l,m}(k) - \left(1 - f^{\mathrm{e}}_k - f^{\mathrm{h}}_k\right) \int_0^\infty \mathrm{d}k' \left(k'\right)^2 \mathcal{V}^l_{k,k'} R_{\lambda,l,m}(k') \,. \tag{3.18}$$

The binding energy $\tilde{E}_\lambda = E_\lambda - E_\mathrm{g}$ has been defined with regard to the band gap while the function $c_{\lambda,l,m}$ collects all radial parts with a magnetic quantum number different from m

$$c_{\lambda,l,m}(k) = \varepsilon^{(3)}_{l,m,k} R_{\lambda,l,m+2}(k) + \varepsilon^{(3)}_{l,m-2,k} R_{\lambda,l,m-2}(k) + \varepsilon^{(4)}_{l-2,m-2,k} R_{\lambda,l-2,m-2}(k)$$
$$+\varepsilon^{(4)}_{l-2,-(m+2),k} R_{\lambda,l-2,m+2}(k) + \varepsilon^{(4)}_{l,-m,k} R_{\lambda,l+2,m-2}(k) \,, \tag{3.19}$$

containing the coupling energies

$$\varepsilon^{(1)}_{l,m,k} = \frac{\hbar^2 k^2}{2}\left[\frac{K^m_l}{\mu_+} + \frac{N^m_l}{\mu_3}\right], \quad \varepsilon^{(2)}_{l,m,k} = \frac{\hbar^2 k^2}{2}\left[\frac{2}{\mu_3} - \frac{1}{\mu_+}\right] L^m_l \,,$$
$$\varepsilon^{(3)}_{l,m,k} = -\frac{\hbar^2 k^2}{2}\frac{X^m_l}{\mu_-} \,, \qquad \varepsilon^{(4)}_{l,m,k} = \frac{\hbar^2 k^2}{2}\frac{W^m_l}{\mu_-} \,, \tag{3.20}$$

where $\mu^{-1}_\pm = \mu^{-1}_1 \pm \mu^{-1}_2$. The appearing weights are given by

$$K^m_l = \frac{l^2 + l + m^2 - 1}{4l^2 + 4l - 3} \,,$$
$$N^m_l = \frac{2l^2 + 2l - 2m^2 - 1}{4l^2 + 4l - 3} \,,$$
$$L^m_l = \frac{1}{2(2l+3)}\sqrt{\frac{(l-m+2)(l-m+1)(l+m+1)(l+m+2)}{(2l+1)(2l+5)}} \,,$$
$$X^m_l = \frac{\sqrt{(l+m+2)(l+m+1)(l-m)(l-m-1)}}{2(4l^2+4l-3)} \,,$$
$$W^m_l = \frac{1}{4(2l+3)}\sqrt{\frac{(l+m+4)(l+m+3)(l+m+2)(l+m+1)}{(2l+1)(2l+5)}} \,. \tag{3.21}$$

It can be observed in Eq. (3.18) that a coupling between different quantum numbers is the consequence of mass anisotropy which breaks the symmetry. More specifically, a pair $\{l, m\}$ couples to itself as well as $\{l \pm 2, m \pm 2\}$, which may be formulated by the notation $\Delta l = \Delta m = \{0, \pm 2\}$.

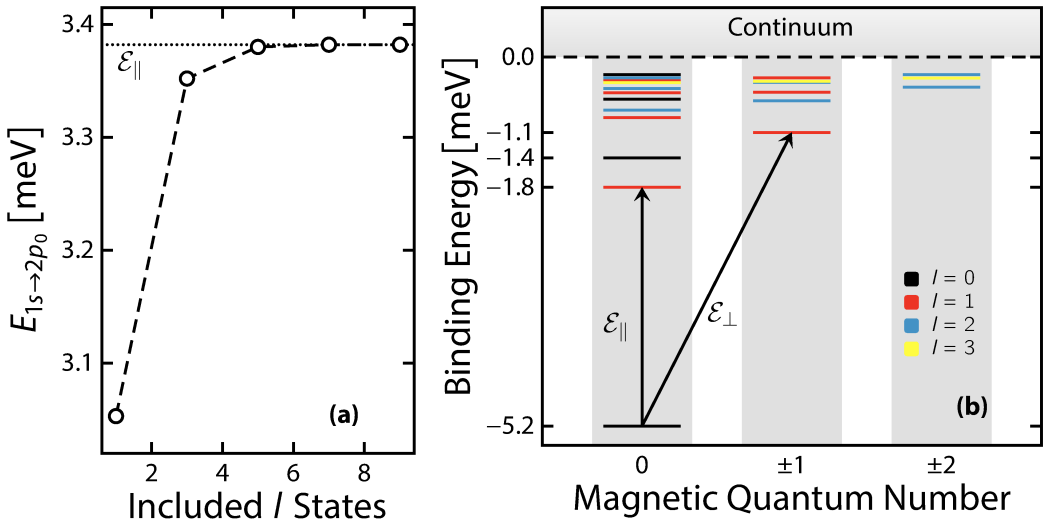

Figure 3.2 — (a) Convergence of the transition energy $E_{1s\to 2p_0}$ between the two energetically lowest states by means of maximally included l quantum number. Converged results are obtained using seven l states. The dashed line only acts as a guide to the eye. (b) Energy diagram of exciton binding energies using Ge masses. Each column represents a magnetic quantum number m while l states are color coded. The lowest allowed THz transitions from the ground state are indicated by arrows and correspond to either parallel ($\mathcal{E}_\parallel$) or perpendicular ($\mathcal{E}_\perp$) THz field polarization.

This is different compared to the usual Wannier equation, which only couples identical quantum numbers. It is worth noting that $c_{\lambda,l,m} = 0$ if $\mu_1 = \mu_2$ so that Eq. (3.18) simplifies significantly and only couples identical m quantum numbers. Moreover, if all masses are equal, Eq. (3.18) reduces to the usual form of the radial Wannier equation.

3.1.2 Excitons in Germanium

Equation (3.18) generally defines the eigenvalue problem for the radial part of the exciton wavefunction in a bulk semiconductor. The only restrictions made are that the single-particle energies can be described adequately within a two-band effective-mass approximation and the carrier distributions remain radially symmetric. For weak excitations at low temperatures, these assumptions are fulfilled [91].

Germanium is an indirect semiconductor with a strong anisotropy [92] constrained to the conduction band L valley. Two of the three electron masses are identical and can be decomposed into a direction parallel ($\parallel$) and perpendicular ($\perp$) to $\boldsymbol{k}_0$ such that $m_{\mathrm{e},1} = m_{\mathrm{e},2} \equiv m_\perp$ and $m_{\mathrm{e},3} \equiv m_\parallel$ (compare Fig. 3.1). The material's extraordinary large anisotropy $m_\parallel/m_\perp \approx 20$ results from the

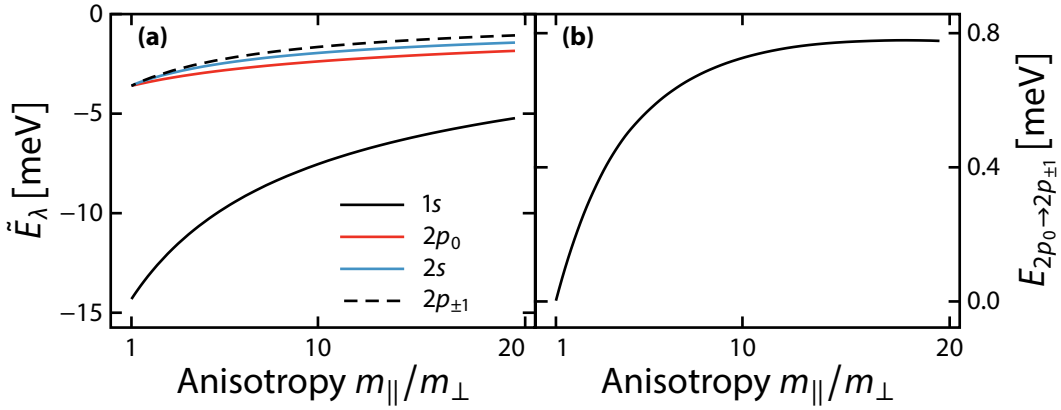

Figure 3.3 — (a) Binding energies of different states as function of anisotropy are presented. (b) The energetic difference $E_{2p_0\to 2p_{\pm1}}$ between the first states with p_0 and $p_{\pm1}$ symmetry (solid red and dashed black lines from Frame (a)).

carrier masses [93]

$$m_\parallel = 1.59\, m_0\,, \tag{3.22}$$

$$m_\perp = 0.0815\, m_0\,, \tag{3.23}$$

$$m_{\mathrm{hh}} = 0.33\, m_0\,. \tag{3.24}$$

Throughout this Section, Ge is used as a prototype system and weak excitations ($f_k^{\mathrm{e}} = f_k^{\mathrm{h}} = 0$) are assumed to demonstrate the major effects of mass anisotropy. A numerical solution of Eq. (3.18) requires a truncation of the maximal included l quantum number because of the expansion (3.5). As a criterion for convergence, we can evaluate the transition energy $E_{\lambda\to\lambda'} = |E_\lambda - E_{\lambda'}|$ between two states λ and λ'. For $\lambda = 1s$ and $\lambda' = 2p_0$, fast convergence is provided by Eq. (3.5), which is shown in Fig. 3.2(a). Stable results are obtained by including seven l states producing $E_{1s\to 2p_0} \equiv \mathcal{E}_\parallel = 3.38\,\mathrm{meV}$ (dotted line). Using the effective masses in Ge, the ground state has dominant s-like symmetry while the first excited state possesses a dominant p_0 character.

Next, it is useful to study the energetic arrangement of exciton states in Ge. Figure 3.2(b) shows $\tilde{E}_\lambda$ for different dominant symmetries. Each column represents a magnetic quantum number m while orbital quantum numbers are color coded. It can be observed that the $2s$, $2p_{\pm1}$, and $2p_0$ states are energetically non-degenerate.

To provide more insights, the gradual change of $\tilde{E}_\lambda$ for these states from isotropic to anisotropic masses is studied in Fig. 3.3(a). It depicts the binding energies of the four first bound excitons as a function of anisotropy $m_\parallel/m_\perp$ while $m_\parallel$ is kept constant. For isotropic masses ($m_\parallel/m_\perp = 1$), all the considered excited states are energetically degenerate, which is the expected result of purely $2s$ and $2p$-like hydrogen wavefunctions. This initial degeneracy is lifted with decreasing $m_\perp$ (or

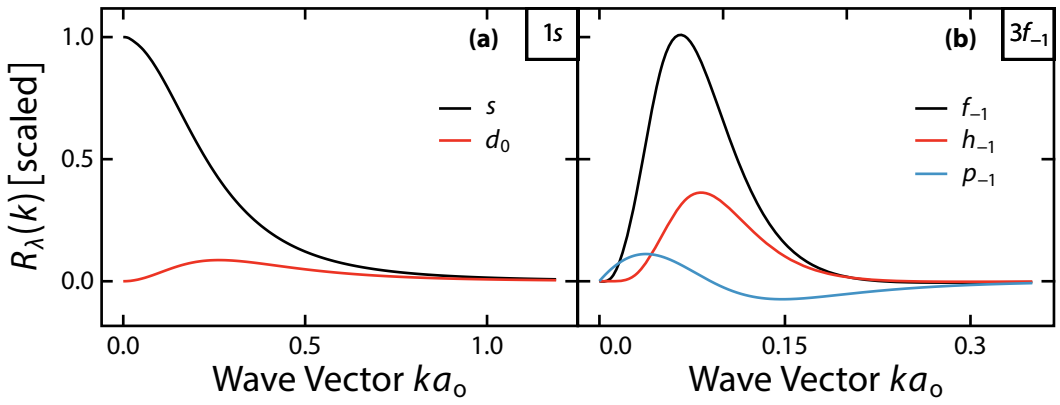

Figure 3.4 — Decomposition of exciton wavefunctions into radial part $R_\lambda(k)$. (a) The 1*s* ground state wavefunction is clearly dominated by the *s*-like radial part. The only other non-vanishing radial part has d_0 symmetry. (b) The decomposition of the $3f_{-1}$ wavefunction shows dominant $\{3, -1\}$ character and a coupling to p_{-1} and h_{-1} radial parts. This is in agreement with the scheme presented at the end of Section 3.1. All other radial parts vanish due to nonexistent coupling.

increasing $m_\parallel/m_\perp$) and reveals this to be a direct consequence of mass anisotropy. The 1*s* ground state emphasizes the general trend of a fast change close to $m_\parallel/m_\perp = 1$ while $\tilde{E}_\lambda$ saturates with increasing anisotropy. Increasing $m_\parallel/m_\perp$ freezes the motion in the parallel direction, which is why this saturation is observed. Measuring the energetic difference $E_{2p_0\to 2p_{\pm1}}$ between the first excited states with p symmetry visualizes the initial degeneracy in Fig. 3.3(b). For Ge masses, $E_{2p_0\to 2p_{\pm1}}$ converges against 0.78 meV. As a result, initially degenerated states are lifted due to the mass anisotropy, producing a $E_{2s\to 2p_0} = 0.415$ meV ($E_{2s\to 2p_{\pm1}} = 0.362$ meV) separation between the $2s$ and the $2p_0$ ($2p_{\pm1}$) states. It is noted that $E_{1s\to 2p_{\pm1}} \equiv \mathcal{E}_\perp = 4.16$ meV, since this transition energy will be of interest in Section 3.1.3.

The previous Section discussed that a wavefunction will contain many $\{l, m\}$ components due to the ansatz (3.5). Figure 3.4 visualizes the resulting coupling rules of Eq. (3.1) for the 1*s* and $3f_{-1}$ states in Frames (a) and (b), respectively, only showing non-vanishing contributions. As the ground state, the 1*s* wavefunction possesses dominantly $\{0, 0\}$ symmetry. The only other non-vanishing component is d_0, which conforms to the coupling rules $\Delta l = \{0, 2\}$ and $\Delta m = 0$ ($\Delta l = -2$ is not possible for $\nu < 2$). No coupling to $\Delta m = \pm 2$ is provided due to identical masses within the plane perpendicular to $\boldsymbol{k}_0$. To verify the full coupling rules, the $3f_{-1}$ wavefunction, which is characterized by the $\{3, -1\}$ radial part, shows non-vanishing $\{1, -1\}$ (or p_{-1}) and $\{5, -1\}$ (or h_{-1}) components.

To gain more insight, modifications to the wavefunctions after the transition from isotropic to anisotropic masses are investigated. The effects are illustrated in Fig. 3.5, which shows a selection of exciton wavefunctions $\left|\psi^{\mathrm{R}}_\lambda(\boldsymbol{k})\right|$ for isotropic (top row) and anisotropic (bottom row) electron

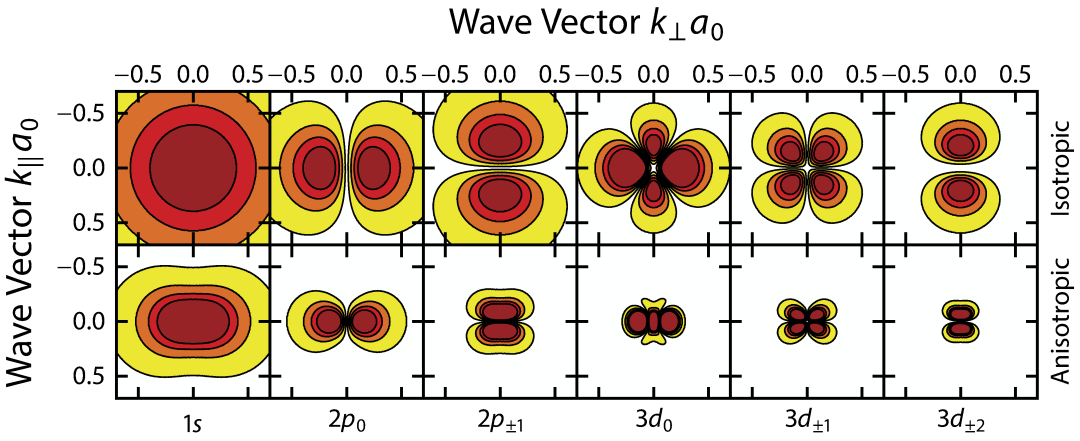

Figure 3.5 — Comparison of the energetically lowest wavefunctions $\left|\psi^{\mathrm{R}}_{\lambda}(\boldsymbol{k})\right|$ which are dominated by $l \leq 2$. Compared are isotropic (top row, $m_\parallel = m_\perp = 1.59\, m_0$) and anisotropic (bottom row, $m_\parallel = 1.59\, m_0$, $m_\perp = 0.0815\, m_0$) masses. The quantum number λ is labeled on the bottom.

masses. The respective quantum number is denoted on the bottom. While in the anisotropic case, Ge masses are used, the isotropic one was obtained with $m_\parallel = m_\perp = 1.59\, m_0$. The latter produces the expected hydrogen-like wavefunctions while anisotropy already squeezes the 1*s* ground state. The observed modifications are explained by the heavier mass in $k_\parallel$ direction. As a result of the changed shape, the degeneracy present for the isotropic states is lifted.

To further examine these distortions, Fig 3.6 shows the $2p_0$ (upper row) and $2p_1$ (bottom row) wavefunctions from Fig. 3.5, which only deviate in the magnetic quantum number m. The left (right) column depicts the isotropic (anisotropic) case. Three dimensional representations are shown aside from the contour plots emphasizing the different amplitudes. Regarding the isotropic wavefunctions, an increase of the magnetic quantum number from $m = 0$ to $m = 1$ only rotates it, which is the expected behavior known from atomic orbitals. In contrast, anisotropic masses dramatically change the shape. The symmetry is broken since $m_\parallel > m_\perp$ which consequently yields a strong squeezing in the $k_\parallel$ direction.

3.1.3 Single-Valley Response to Classical THz Excitation

It is instructive to study the THz response at a single L valley first, even though it might be experimentally difficult to generate excitons in this way due to rapid inter-valley equilibrium scattering [94]. The results will be generalized to include realistic multi-valley excitations in Section 3.1.4.

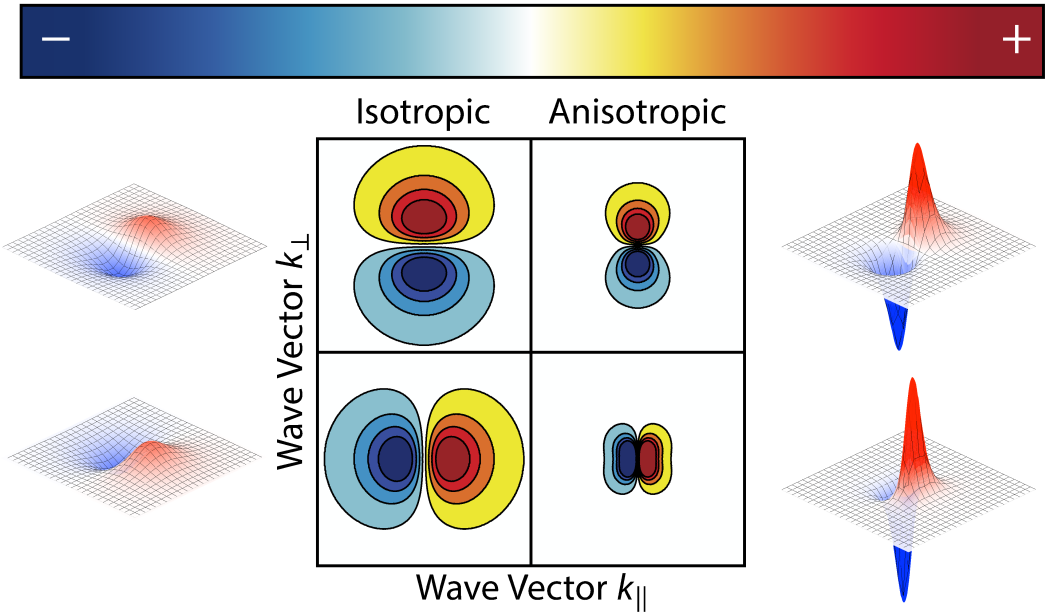

Figure 3.6 — Wavefunction with dominant symmetry $2p_0$ (top row) and $2p_1$ (bottom row). Isotropic (left column) are compared to anisotropic (right column) masses with a three dimensional representation aside each contour plot.

Using the coordinate system of Fig. 3.1, the eight L valleys in Ge are situated at

$$\boldsymbol{k}_0 \equiv \boldsymbol{L}_0 = \frac{\sqrt{3}\pi}{a}(0 \quad 0 \quad 1)^\top, \qquad \boldsymbol{L}_1 = \frac{\sqrt{3}\pi}{a}\left(-\tfrac{\sqrt{2}}{3} \quad -\sqrt{\tfrac{2}{3}} \quad \tfrac{1}{3}\right)^\top, \tag{3.25}$$

$$\boldsymbol{L}_2 = \frac{\sqrt{3}\pi}{a}\left(-\tfrac{2}{3}\sqrt{2} \quad 0 \quad -\tfrac{1}{3}\right)^\top, \qquad \boldsymbol{L}_3 = \frac{\sqrt{3}\pi}{a}\left(-\tfrac{\sqrt{2}}{3} \quad \sqrt{\tfrac{2}{3}} \quad \tfrac{1}{3}\right)^\top, \tag{3.26}$$

and $\boldsymbol{L}_{j+4} = -\boldsymbol{L}_j$, where $a = 5.6579\,\text{Å}$ is the lattice constant of Ge [95]. However, the L valley in total is only fourfold degenerate, because each valley is shared equally with the adjacent Brillouin zone. In this Section, the response at $\boldsymbol{L}_0$ will be calculated for a THz field $\boldsymbol{A}_{\text{THz}}(t) = A_0(t)\,\boldsymbol{e}_A$. The polarization $\boldsymbol{e}_A$ which addresses the sample can be either aligned parallel ($\boldsymbol{e}_A = \boldsymbol{e}_3 \equiv \boldsymbol{e}_{||}$) or perpendicular ($\boldsymbol{e}_A = x\boldsymbol{e}_1 + y\boldsymbol{e}_2 \equiv \boldsymbol{e}_\perp$ with $x^2 + y^2 = 1$) to $\boldsymbol{L}_0$. Due to equal masses in $\boldsymbol{e}_1$ and $\boldsymbol{e}_2$ directions, the response within the $\boldsymbol{e}_1$–$\boldsymbol{e}_2$ plane is identical. Therefore, the choice $x = 0$ and $y = 1$ is justified and the simplification $\boldsymbol{e}_\perp = \boldsymbol{e}_2$ holds without loss of generality. The two polarizations are depicted in Fig. 3.1(b) by blue arrows.

The THz field $\boldsymbol{A}_{\text{THz}}$ excites the system for parallel and perpendicular polarization via

$$j_{||}(\boldsymbol{k}) = -\frac{e\hbar k_3}{\mu_{||}}, \qquad j_\perp(\boldsymbol{k}) = -\frac{e\hbar k_2}{\mu_\perp}, \tag{3.27}$$

which follows from Eq. (2.60) using the effective-mass approximation (2.14). Accordingly, the transition-matrix elements (2.59) become

$$J^{\parallel}_{\lambda,\nu} = -\frac{e\hbar L^3}{8\pi^3\mu_3}\int_0^\infty \mathrm{d}k\, k^3 \sum_{l=0}^{\infty}\sum_{m=-l}^{l} R^{\star}_{\lambda,l,m}\left[g^m_l\, R_{\nu,l+1,m} + g^m_{l-1}\, R_{\nu,l-1,m}\right], \tag{3.28}$$

and

$$\begin{aligned} J^{\perp}_{\lambda,\nu} = -\mathrm{i}\frac{e\hbar L^3}{8\pi^3\mu_2}\int_0^\infty \mathrm{d}k\, k^3 \sum_{l=0}^{\infty}\sum_{m=-l}^{l} R^{\star}_{\lambda,l,m}\Big[f^m_l\, R_{\nu,l+1,m+1} - f^{-m}_l\, R_{\nu,l+1,m-1} \\ - f^{-m-1}_{l-1}\, R_{\nu,l-1,m+1} + f^{m-1}_{l-1}\, R_{\nu,l-1,m-1}\Big], \end{aligned} \tag{3.29}$$

containing the weight functions

$$g^m_l = \sqrt{\frac{(l-m+1)(l+m+1)}{(2l+3)(2l+1)}}, \tag{3.30}$$

$$f^m_l = -\frac{1}{2}\sqrt{\frac{(l+m+1)(l+m+2)}{(2l+1)(2l+3)}}. \tag{3.31}$$

Equations (3.28) and (3.29) define selection rules incorporating effects due to the mass anisotropy. In particular, $J^{\parallel}_{\lambda,\nu}$ vanishes for all transitions except those with equal m components while the l quantum number differs by ±1. In the usual notation, this is $\Delta m = 0$ and $\Delta l = \pm 1$. Regarding $\boldsymbol{e}_\perp$ polarized excitons, the transition rules translate according to $\Delta m = \Delta l = \pm 1$. Consequently, the energetically lowest allowed THz transition is $\mathcal{E}_\parallel$ and $\mathcal{E}_\perp$ for parallel and perpendicular polarized THz fields, respectively, assuming exclusive occupation of 1s ground-state excitons. Thus, 1s and $2p_0$ ($2p_{\pm1}$) states are involved for $\boldsymbol{e}_A = \boldsymbol{e}_\parallel$ ($\boldsymbol{e}_A = \boldsymbol{e}_\perp$) and both transitions are illustrated in Fig. 3.2 by arrows. Conclusively, these two transitions differ by $\mathcal{E}_\perp - \mathcal{E}_\parallel = 0.78\,\mathrm{meV}$ as a consequence of the mass anisotropy and produce direction-dependent THz resonances.

The wavefunctions describing the sample's many-body state are determined for arbitrary carrier masses by Eq. (3.18) as discussed in the previous Section. Once they are known, the linear THz absorption spectrum follows from the THz Elliott Formula (2.61). Although weak carrier densities are still assumed throughout this Section, three different excitation conditions will be investigated:

(i) Coherent excitons generated at the Γ valley,

(ii) incoherent excitons formed across the L valley addressed by parallel polarization,

(iii) incoherent excitons formed across the L valley addressed by perpendicular polarization.

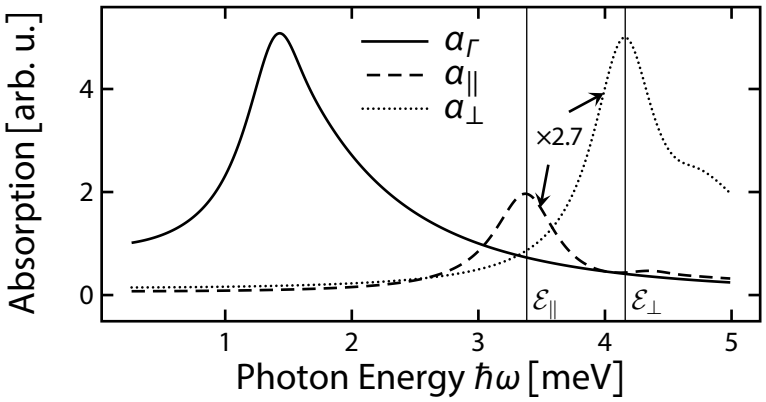

Figure 3.7 — THz absorption spectra of Ge. Assuming carrier masses of excitons forming at the Γ valley (solid line) leads to a significantly stronger signal and an energetically lower fundamental transition compared to excitons forming across the indirect L valley. The spectra for parallel (dashed line) and perpendicular (dotted line) polarization are magnified for clarity. Thin vertical lines indicate the fundamental transition energies for indirectly bound excitons.

While incoherent excitons exhibit the full mass anisotropy in the L valley, coherent excitons form at the direct Γ point. Thus, the carrier masses are isotropic with $m_\mathrm{e} = 0.041\, m_0$ [93] and no dependency on the THz polarization exists. Experimentally, these two situations can be achieved via the delay between optical-pump and THz-probe beam: Directly after the optical excitation at the direct Γ point, a THz probe pulse would detect the coherent polarization as depicted in Fig 3.1(b) as a red-shaded area. Due to the long temporal extension of a THz pulse compared to the equilibrium scattering times of conduction band electrons, the experimental realization of such a situation poses an extreme challenge. In Ge, conduction band electrons eventually scatter into the indirect L valley, which takes about 400 fs [96, 97]. Since quantum-optical many-body correlations build up sequentially [98], the radiative lifetime must be sufficiently long to allow carriers to scatter into the indirect valley and provide abundant exciton formation (orange-shaded area in Fig. 3.1(a)). Typically, this presumption is fulfilled in many indirect semiconductors at low temperatures and long after a weak optical excitation [91, 99–101]. Then, a THz pulse detects the indirectly bound excitons. The binding energies are computed to be $\tilde{E}^{\Gamma}_{1s} = -1.910\,\mathrm{meV}$ and $\tilde{E}^{L}_{1s} = -5.228\,\mathrm{meV}$ for direct and indirect excitons, respectively. These values are in reasonable agreement with previous theoretical and experimental findings [102–109].

Figure 3.7 compares the THz absorptions α_Γ, $\alpha_\parallel$, and $\alpha_\perp$ corresponding to situations (i), (ii), and (iii), respectively. It is assumed that only the 1s ground state exciton is occupied with a density n_{1s}, e.g. $\Delta n_{\lambda,\nu} = \delta_{\lambda,\nu}\delta_{\lambda,1s} n_{1s}$. The dephasing has been chosen to be $\gamma = \gamma_J = 0.3\,\mathrm{meV}$. Contributions due to a correlated electron–hole plasma have been neglected here since they only add a Drude-

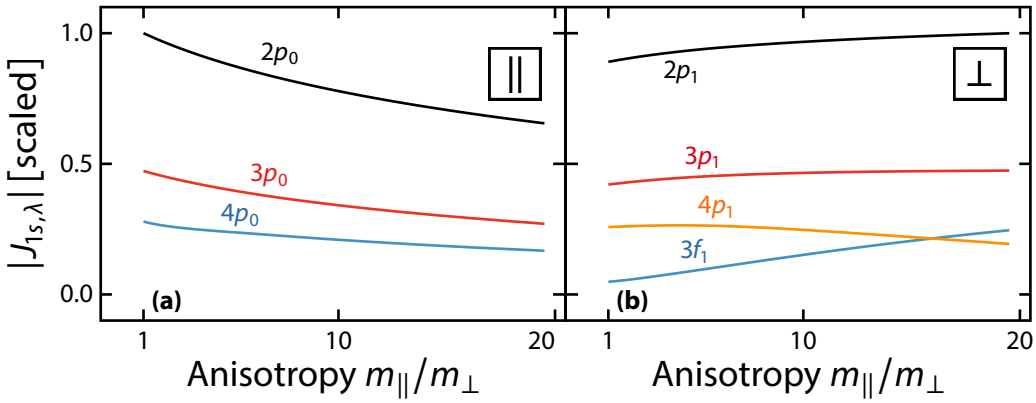

Figure 3.8 — Transition-matrix elements from the ground state for parallel and perpendicular THz polarization. (a) For $\boldsymbol{e}_A = \boldsymbol{e}_{||}$, the first three allowed transitions from the 1*s* state have p_0 symmetry. (b) The first four end states for $\boldsymbol{e}_A = \boldsymbol{e}_{\perp}$ have dominantly p_1 and f_1 symmetry.

type free carrier response to the spectrum [58]. The coherent exciton response α_Γ (solid line) is shown besides the incoherent exciton THz absorption $\alpha_{||}$ (dashed line) and $\alpha_{\perp}$ (dotted line) for parallel and perpendicular polarization, respectively. Both incoherent responses have been magnified by a factor 2.7 for enhanced visibility. The symmetry-based arguments about the selection rules are corroborated by the two distinct resonance energies (thin vertical lines), exhibited by these responses.

To study general trends of THz-transition oscillator strengths, Fig. 3.8 shows $\left|J_{1s,\lambda}\right|$ as a function of anisotropy $m_{||}/m_{\perp}$ for selected end states λ. Frames (a) and (b) depict parallel and perpendicular polarizations according to Eqs. (3.28) and (3.29), respectively. The selection rules determine the symmetry of the first three end states to be p_0 for parallel polarized excitons. Conversely, the first four non-vanishing matrix elements for perpendicularly polarized excitons are of p_1 and f_1 symmetry. From the THz-Elliott formula (2.61) it can be deduced that $J_{1s,\lambda}$ determines the strength of absorption for 1*s*-to-λ transitions as it is a measure of the overlap of the participating wavefunctions. Since it monotonically decreases for parallel polarization while it increases in the perpendicular case, the corresponding THz absorption appears stronger in perpendicular polarization as observed in Fig. 3.7.

3.1.4 Muli-Valley Response to Classical THz Excitation

Until now, the THz absorption for purely parallel and perpendicular directions at a single L valley has been calculated. A generalization, which takes the fourfold degeneracy of the L point into account, is the subject of this Section.

The issue is visualized in Fig. 3.9. A polarization $\boldsymbol{e}_A$ may address the particular valley $\boldsymbol{L}_0$ in an

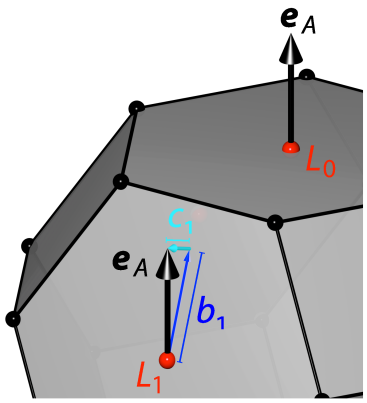

Figure 3.9 — Detail of the first Brillouin zone of a cubic semiconductor. Focusing on Ge, only L valleys are highlighted explicitly. A polarization vector $\boldsymbol{e}_A = \boldsymbol{e}_3$ at the L_0 valley has no in-plane component but the polarization addresses all L simultaneously. Hence, the effective polarization at a different L point contains both in- and out-of-plane contributions, shown in blue and cyan, respectively.

exclusively parallel direction. But the same vector $\boldsymbol{e}_A$ would excite both parallel and perpendicular excitons at a different valley, e.g. $\boldsymbol{L}_1$. To obtain the full THz response, the absorption at each of the eight valleys needs to be calculated for an arbitrary polarization.

As discussed in the previous Section, the THz responses at a single valley are identical within the hexagonal planes of the truncated octahedron that define the first Brillouin zone. Thus, the in-plane response is independent of the exact in-plane direction, so that an arbitrary polarization may be written as

$$\boldsymbol{e}_A = b\,\boldsymbol{e}_\perp + c\,\boldsymbol{e}_\parallel\,, \qquad \boldsymbol{e}_\perp = x\,\boldsymbol{e}_1 + y\,\boldsymbol{e}_2\,, \tag{3.32}$$

with $b^2 + c^2 = 1$. Unlike in the previous section, $\boldsymbol{e}_\perp$ is not restricted on a principal axis. A geometrical approach to compute the total response is to find the in- and out-of-plane projections of the polarization vector to all L valleys, as depicted in Fig. 3.9. They determine the fraction of $\alpha_\parallel$ and $\alpha_\perp$ to the total absorption.

Let b_j and c_j denote the respective in- and out-of-plane projections of $\boldsymbol{e}_A$ at the valley $\boldsymbol{L}_j$ (see Fig. 3.9). Then, the total absorption is given by

$$\alpha_{\mathrm{THz}}(\omega) = \frac{1}{2}\left[\alpha_\perp(\omega)\sum_{j=1}^{8} b_j^2 + \alpha_\parallel(\omega)\sum_{j=1}^{8} c_j^2\right], \tag{3.33}$$

where the factor $\frac{1}{2}$ accounts for the sharing of each valley between adjacent Brillouin zones. Repeating the derivation from Section 3.1.1 with $\boldsymbol{k}_0 \to -\boldsymbol{k}_0$ reveals that two opposing valleys yield the

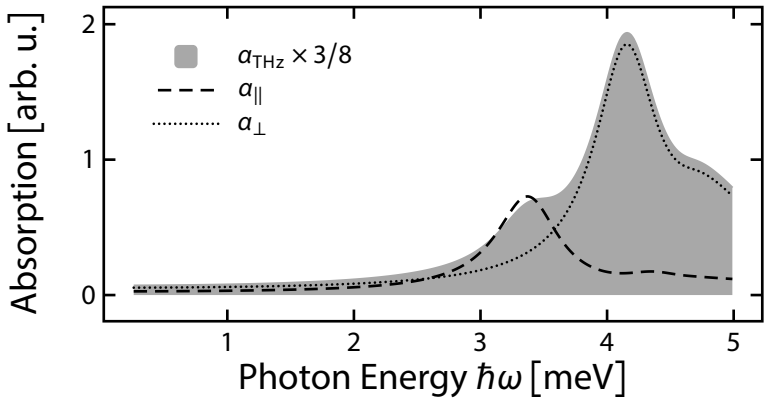

Figure 3.10 — Full THz absorption $\alpha_{\mathrm{THz}}(\omega)$ (shaded area) according to Eq. (3.37). The individual contributions from the parallel (solid line) and perpendicular (dashed line) constituents are also shown. A scaling factor of 3/8 has been applied to the full spectrum for visibility.

same response. Hence, Eq. (3.33) becomes

$$\alpha_{\mathrm{THz}}(\omega) = \alpha_{\perp}(\omega) \sum_{j=1}^{4} b_j^2 + \alpha_{\parallel}(\omega) \sum_{j=1}^{4} c_j^2 \,. \tag{3.34}$$

Next, b_j and c_j are calculated for all relevant L points. The in-plane projection is found via

$$c_j = \boldsymbol{L}_j \cdot \boldsymbol{e}_A = b\, \boldsymbol{L}_j \cdot \boldsymbol{e}_{\perp} + c\, \boldsymbol{L}_j \cdot \boldsymbol{e}_{\parallel} \equiv b\, A_j + c\, B_j \,. \tag{3.35}$$

The coefficients A_j and B_j are summarized in Table 3.1 and it follows that

$$\sum_{j=1}^{4} b_j^2 = \frac{8}{3} \,, \qquad \sum_{j=1}^{4} c_j^2 = \frac{4}{3} \,, \tag{3.36}$$

resulting in the total THz absorption

$$\alpha_{\mathrm{THz}}(\omega) = \frac{4}{3} \Big[2\alpha_{\perp}(\omega) + \alpha_{\parallel}(\omega) \Big] \,, \tag{3.37}$$

j	1	2	3	4
A_j	0.0	−0.4714	−0.9428	−0.4714
B_j	1	1/3	–1/3	1/3

Table 3.1 —Coefficients found from Eq. (3.35).

where $b_j^2 = 1 - c_j^2$ and $b^2 + c^2 = 1$ is used. Hence, the THz absorption for any arbitrary polarization always yields the same mixture of parallel and perpendicular constituents. A simple interpretation of this result is that the total response is determined by the directional mean value of all four relevant L valleys. The full absorption is shown along its two components in Fig. 3.10. Although $\alpha(\omega)$ contains a mixture composed of all directions, it still exhibits a residual double-peak structure as a result of the mass anisotropy. This result suggests that anisotropic masses can be detected directly via available THz experiments [68, 72, 110]. As a prerequisite, the dephasing γ and γ_J must not greatly exceed the anisotropic splitting of 0.78 meV. To the best of the authors knowledge, such experiments have not yet been conducted using Ge samples.

Alternative Derivation

An alternative view on the THz current provides a more concise derivation of Eq. (3.37) that does not rely on geometrical arguments. The THz interaction Hamiltonian (2.57) may be written as

$$H_{\mathrm{THz}} = -\boldsymbol{J} \cdot \boldsymbol{A}_{\mathrm{THz}}\,, \tag{3.38}$$

containing the carrier-density dependent part of the current

$$\boldsymbol{J} = \sum_n \boldsymbol{J}_n = \sum_n \sum_{\lambda,\boldsymbol{k}_n} \boldsymbol{j}^{\lambda}_{\boldsymbol{k}_n}\, \hat{a}^{\dagger}_{\lambda,\boldsymbol{k}_n} \hat{a}_{\lambda,\boldsymbol{k}_n}\,, \tag{3.39}$$

where $\boldsymbol{k}_n$ is in the vicinity of $\boldsymbol{L}_n$.

It is beneficial to introduce the vector $\boldsymbol{e}_{n,m}$, which is obtained from the unit vector $\boldsymbol{e}_m$ via a rotation so that $\boldsymbol{e}_{n,3}$ and $\boldsymbol{L}_n$ are aligned. This guarantees that a set $\boldsymbol{e}_{n,m}$ forms a coordinate system where $\boldsymbol{e}_{n,z}$ points out-of and $\boldsymbol{e}_{n,1}/\boldsymbol{e}_{n,2}$ are within the n-th Brillouin zone edge plane. Hence, the absorption follows from the single-valley response as described in Section 3.1.3.

The current at the n-th L point is given by

$$\boldsymbol{J}_n = \sum_m J_{n,m}(\omega)\boldsymbol{e}_{n,m}\,, \qquad J_{n,m}(\omega) = \boldsymbol{J}_n \cdot \boldsymbol{e}_{n,m}\,. \tag{3.40}$$

At the same time, the current at $\boldsymbol{L}_n$ in direction m is [10]

$$J_{n,m}(\omega) = \frac{1}{2}\epsilon_0\, \omega^2 \chi_m(\omega) A_{L_n,m}(\omega)\,, \tag{3.41}$$

where

$$A_{n,m}(\omega) = \boldsymbol{A}_{\mathrm{THz}}(\omega) \cdot \boldsymbol{e}_{n,m}\,, \tag{3.42}$$

is the projected THz field. Equation (3.41) also contains the single-valley susceptibility χ_m. This approximation is valid when no crosstalk of the current is expected, e.g. in the linear regime. Hence,

we can compute χ_m at a reference valley as done in Section 3.1.3. An additional factor 1/2 accounts for the sharing of each L point with the adjacent Brillouin zone. Then, the total response is determined by

$$\begin{aligned}\chi(\omega) &\equiv \frac{\boldsymbol{J}\cdot\boldsymbol{e}_A}{\epsilon_0\,\omega^2 A(\omega)} = \frac{1}{2}\frac{1}{A(\omega)}\sum_{n,m}\chi_m A_{n,m}\boldsymbol{e}_{n,m}\cdot\boldsymbol{e}_A \\ &= \boldsymbol{e}_A\cdot\sum_{n,m}\frac{\chi_m}{2}(\boldsymbol{e}_{n,m}\otimes\boldsymbol{e}_{n,m})\cdot\boldsymbol{e}_A \equiv \boldsymbol{e}_A\cdot\sum_n \underline{\underline{\chi}}_n\cdot\boldsymbol{e}_A\,,\end{aligned} \tag{3.43}$$

defining both the total susceptibility χ and the susceptibility tensor $\underline{\underline{\chi}}$. The Fourier transform of $A(t)$ is denoted by $A(\omega)$. For example, it is

$$\underline{\underline{\chi}}_1 = \begin{pmatrix}\chi_\perp & 0 & 0\\ 0 & \chi_\perp & 0\\ 0 & 0 & \chi_\parallel\end{pmatrix}, \tag{3.44}$$

since $\chi_1 = \chi_2 \equiv \chi_\perp$ and $\chi_3 = \chi_\parallel$. Considering all eight L valleys, it is

$$\sum_n \underline{\underline{\chi}}_n = \frac{4}{3}\Big(2\chi_\perp + \chi_\parallel\Big)\begin{pmatrix}1 & 0 & 0\\ 0 & 1 & 0\\ 0 & 0 & 1\end{pmatrix}. \tag{3.45}$$

Applied to Eq. (3.43), the total susceptibility reads

$$\chi(\omega) = \frac{4}{3}\Big(2\chi_\perp + \chi_\parallel\Big), \tag{3.46}$$

which yields Eq. (3.37) via the general expression (2.50) for the linear absorption.

3.2 THz Spectroscopy of Bulk Silicon

To the best of the authors knowledge, an experiment as described in the previous Section has not yet been conducted. However, similar measurements in Si have been performed by Suzuki and Shimano [83]. Therefore, the calculations from the previous Section shall be repeated adapted to Si, in which the electron masses are [95]

$$m_\parallel = 0.98\,m_0\,, \qquad m_\perp = 0.19\,m_0\,, \qquad m_{\mathrm{hh}} = 0.49\,m_0\,. \tag{3.47}$$

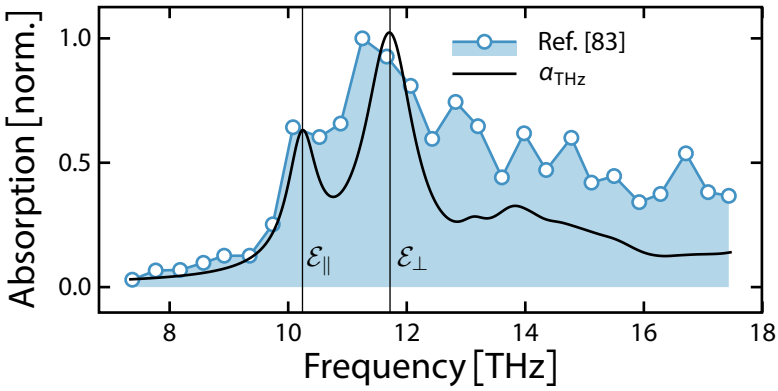

Figure 3.11 — THz absorption of bulk Si. Experiments from Ref. [83] (blue-shaded area) are compared to the full absorption obtained from Eq. (3.48) (black solid line).

In Si, the energetic minima are situated somewhere between the Γ and X points [111] and threefold degenerate. It is straightforward to show that the total absorption is then given by

$$\alpha_{\mathrm{THz}}(\omega) = \frac{6}{2}\frac{1}{3}\Big[\,2\alpha_{\perp}(\omega) + \alpha_{\parallel}(\omega)\Big], \tag{3.48}$$

which can be interpreted as the spatial average at a single valley again, multiplied by the degeneracy of the energetic minima accounting for the sharing between adjacent Brillouin zones.

The results are summarized in Fig. 3.11. A blue-shaded area represents the experimental data from Ref. [83], which depicts a situation 600 ps after a weak optical excitation. The authors of that study assign the double-peak characteristic at 10.1 THz and 11.3 THz to the fine structure of an isotropic $2p$ excitons, arising from the simultaneous presence of both parallel and anti-parallel spin alignments of the participating carriers. However, no effort was made to actually prove this statement, although several experiments are suitable for this purpose. For example, excitons can be spin-polarized using circularly polarized radiation [112]. An exciton population with exclusively parallel or anti-parallel spin-polarization would not give rise to a fine structure. Furthermore, applying an external magnetic field would allow the manipulation of the fine structure splitting via the field strength and orientation [113]. Besides, the separation of the fine structure splitted states is usually in the range of 0.002 – 0.03 THz [114] due to small exchange interactions. Even big splittings of 0.5 THz, which occur only in rare cases such as cadmium selenide (CdSe) quantum dots (QDs) [114], are smaller than the observed splitting of 1.2 THz in Fig. 3.11.

The theoretically obtained spectrum (solid black line) shows a certain agreement with the experiment. Especially the transition energies of parallel and perpendicular responses indicated by thin vertical lines coincide with the measured resonances. Even the asymmetric high frequency tail is covered by the theoretical data, while the original study does not explain this at all. Also, the

oscillator strengths of the relevant transitions are matching those that are observed experimentally. The good agreement between experiment and theory suggests that the observed features originate from the mass anisotropy rather then fine structure effects. However, thorough studies are required to sustain such assumptions.

3.3 Absorption of Bulk Rutile

For many optically interesting systems it is impossible to calculate fundamental properties such as energy dispersions or single-particle wavefunctions using the $\boldsymbol{k} \cdot \boldsymbol{p}$ theory due to a lack of knowledge of the relevant band parameters. Concerning TiO_2, not a single Luttinger parameter can be found in the literature today. These nontrivial systems such as complex compounds and interface-dominated or organic/inorganic heterostructures impose a challenging task. However, with DFT it is possible to calculate band structures and optical-matrix elements of the ground state in any arbitrary system. On the other side, the CE outlined in Section 2.2 has been proven extremely suitable to obtain dynamics of relevant microscopic operator expectation values.

In this Section, the CE–DFT method is presented that combines the strength of DFT and the CE. At a glance, DFT determines ground-state optical-matrix elements while the dynamics of the excited many-body system are computed using the CE. Under certain conditions, it is possible to obtain the optical absorption via the wavefunctions described in Section 3.1.1. Rutile serves as a prototype system in this Section to verify the method.

3.3.1 Density Functional Theory

Chapter 2 outlines the main results of the semiconductor many-body physics relevant for this thesis. Knowledge of the complete system wavefunction Ψ was not necessary at any step of the derivations. The introduction of field operators reduced the needed information to single-particle wavefunctions that obey a much simpler Schrödinger equation (2.10) for which the $\boldsymbol{k} \cdot \boldsymbol{p}$ theory provides a useful framework with low computational effort. Although the expansion (2.5) can be done using any complete set of basis functions, the natural integration of effective dimensionalities via the confinement function makes the use of single-particle wavefunctions advantageous.

Nevertheless, the complete system wavefunction Ψ obeys the Schrödinger equation

$$H\,\Psi(\boldsymbol{r}_1, \boldsymbol{r}_2, \ldots, \boldsymbol{r}_N) = E\,\Psi(\boldsymbol{r}_1, \boldsymbol{r}_2, \ldots, \boldsymbol{r}_N)\,, \tag{3.49}$$

where H is the many-body Hamiltonian Eq. (2.1) for N electrons moving in the crystal lattice while E is the electronic eigenenergy. The attempt to solve Eq. (3.49) would obviously fail due to the huge amount of $3N$ variables in a realistic many-body system and limited computing resources. Over time, many powerful methods have been developed to solve the Schrödinger equation. The diagrammatic perturbation theory based on Feynman diagrams and Green's functions have been used

in physics. In chemistry, a systematic expansion in terms of Slater determinants has been applied widely but it has hardly been practicable to calculate properties of systems with more than 100 molecules with this method [24]. DFT provides a remedy concerning this limitations. Although it might be less accurate, it presents itself as a versatile and viable alternative. Many structural, electronic, or magnetic properties of molecules, semiconductors, and other materials have been calculated using DFT, granting it a significant role in fundamental natural sciences [115]. Awarding the Nobel Prize in 1998 to John A. Pople [116] and Walter Kohn [117], who is one of the founding fathers of this method, emphasizes its importance.

The central quantity in DFT is the electron density

$$n(\boldsymbol{r}) = N \iiint \mathrm{d}\boldsymbol{r}_2\, \mathrm{d}\boldsymbol{r}_3 \ldots \mathrm{d}\boldsymbol{r}_N \left|\Psi(\boldsymbol{r}, \boldsymbol{r}_2, \ldots, \boldsymbol{r}_N)\right|^2 . \tag{3.50}$$

In their famous paper [23], Hohenberg and Kohn showed that it is in principle possible to find the wavefunction Ψ_0 and energy E_0 of a systems ground state, given that its density is known. In other words, the ground state density n_0 and wavefunction Ψ_0 are connected via a functional $\Psi_0[n_0]$ and as a consequence, all other system observables will be, too. This effectively reduces the number of variables from $3N$ to only 3, making a numerical solution possible.

For an arbitrary density n, the energy functional is given by

$$E[n] = \min_{\Psi \to n} \langle \Psi | H | \Psi \rangle \ , \tag{3.51}$$

where $\Psi \to n$ denotes the requirement that Ψ must reproduce n via Eq. (3.50) while a ground-state wavefunction has to minimize the system's energy. Since the energy will be at least as large as the ground state energy for any $n \neq n_0$, e.g. $E[n_0] \leq E[n]$, a variational procedure can be applied to obtain an approximative solution for n_0 and Ψ_0. Usually, Eq. (3.51) is divided according to the Kohn–Sham equations, which is the most popular formulation of DFT. Its foundation is the representation of the interacting electrons to a system of non-interacting carriers, introducing the Kohn–Sham orbitals from which single-particle properties (such as the band structure) can be derived. This allows the separation into an uncorrelated kinetic part — which can be solved exactly — and the exchange correlation energy. The latter is not exactly solvable because the exchange correlation potential is unknown. Although DFT is formally exact, this embodies its greatest weakness, since only boundary conditions for the exchange potential can be formulated. This lack of knowledge restricts DFT from being truly universal and forces one to find the most suitable functional to reproduce physical properties like band gaps.

Different functionals have been proposed to cope with this issue. It is well known that some reproduce only certain physical aspects. Possibly the most famous example is the underestimation of the band gap using the Perdew–Burke–Ernzerhof (PBE) [118, 119] functional. Nevertheless, the PBE functional successfully describes the valence-band effective masses or the spatial relaxation of atoms [120].

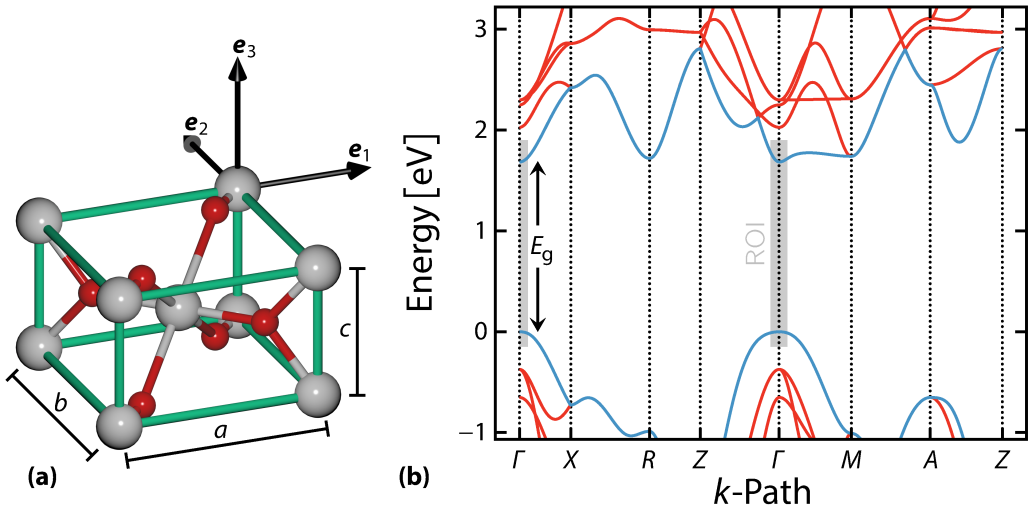

Figure 3.12 — (a) Tetragonal unit cell of rutile, where the grey and red spheres depict titanium and oxygen atoms, respectively. (b) The band structure obtained by density functional theory calculations is depicted for momentum paths along the high symmetry points of the crystal. The region of interest (ROI) relevant for optical transitions has been marked as a grey-shaded area.

3.3.2 Band Structure and Matrix Elements

In this Section, the CE-DFT method is demonstrated using rutile as a prototype system. Rutile is the most common natural form of TiO_2 whose crystal structure is defined by a unit cell with lattice constants $a = b = 4.59$ Å and $c = 2.96$ Å [121] depicted in Fig. 3.12(a). In principle, this is the only required input information for a DFT calculation, which has been carried out using the SIESTA [122] code.

The diagonalization of the Kohn–Sham Hamiltonian yields the band structure and Bloch functions. These in turn can be used to calculate optical transition-matrix elements. Figure 3.12(b) presents the Kohn–Sham energies for various paths connecting points of high symmetry in the first Brillouin zone. This indicates a direct band gap at the Γ point. Shaded areas mark the regions around the Brillouin zone center that are relevant for optical transitions. Since these regions are very small compared to the Brillouin-zone extension and within, higher bands are separated by some 100 meV, the discussion is restricted in the following to include only two bands (blue lines in Fig. 3.12(b)).

As mentioned in the previous Section, the PBE functional frequently underestimates the band gap and therefore needs to be adjusted. Usually, this is done by shifting all conduction bands so that an experimentally available value for the band gap is reproduced [123, 124]. The band gap of rutile is not exactly known, but generally accepted to be $E_g = 3.03$ eV [125]. Hence, a shift of 1.3 eV

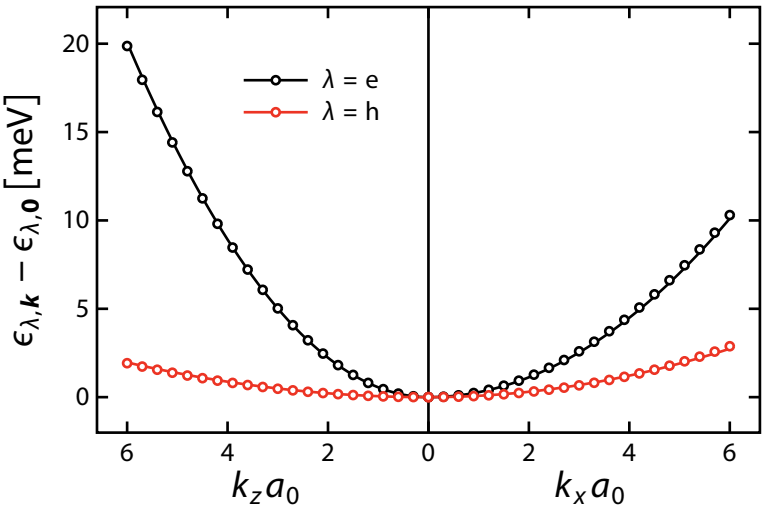

Figure 3.13 — Magnification of the band structure into the region of interest shown as a shaded area in Fig. 3.12(b). The dots resemble results obtained by density functional theory calculations, while the solid lines are parabolic fits, allowing to extract effective masses.

is applied to the conduction band.

Carriers in the lowest conduction band exhibit a strong mass anisotropy due to different curvatures into different momentum directions. Figure 3.13 presents a magnification of the region of interest (shaded area in Fig. 3.12(b)). Besides the DFT single-particle energies (dots), parabolic approximations (solid lines) according to Eq. (2.14) are shown. They reproduce the band structure almost perfectly, with only minor deviations at larger momenta. This degree of agreement is obtained using the effective masses $m_{\mathrm{e},1} = m_{\mathrm{e},2} \equiv m_{\mathrm{e},\perp} = 1.03\, m_0$, $m_{\mathrm{e},3} \equiv m_{\mathrm{e},\parallel} = 0.519\, m_0$, $m_{\mathrm{h},1} = m_{\mathrm{h},2} \equiv m_{\mathrm{h},\perp} = 3.8\, m_0$, and $m_{\mathrm{h},3} \equiv m_{\mathrm{h},\parallel} = 5.3\, m_0$. Here, the notation of Section 3.1.2 has been applied with a minor modification: Since the highest valence band is non-degenerate and hence no classification into hh and lh is feasible, it is labeled h instead of hh. As opposed to Ge, carriers in the valence band also exhibit anisotropy. The replacement of the true band structure by the effective-mass approximation later allows the usage of exciton wavefunctions obtained by Eq. (3.18).

To explain the optical-absorption spectra of TiO_2, the transversal electric and magnetic fields in Eq. (2.2) are expanded in terms of multipoles. For this purpose, they are assumed to have the form $\boldsymbol{E}(\boldsymbol{r},t) = -\frac{\partial}{\partial t}\boldsymbol{A}(\boldsymbol{r},t) \equiv E(t)\boldsymbol{E}(\boldsymbol{r})$ and $\boldsymbol{B}(\boldsymbol{r},t) = \nabla \times \boldsymbol{A}(\boldsymbol{r},t) \equiv E(t)/\omega\, \boldsymbol{B}(\boldsymbol{r})$. After the quantization procedure, the light–matter coupling term in Eq. (2.1) reads

$$\hat{H}_{\mathrm{D}} = -E(t) \sum_{\lambda,\boldsymbol{k}} \sum_{\nu,\boldsymbol{k}'} F_{\lambda,\boldsymbol{k}}^{\nu,\boldsymbol{k}'}\, \hat{a}_{\lambda,\boldsymbol{k}}^{\dagger} \hat{a}_{\nu,\boldsymbol{k}'}\,, \tag{3.52}$$

where its strength is given by

$$F_{\lambda,\boldsymbol{k}}^{\nu,\boldsymbol{k}'} = \int \mathrm{d}^3 r\; \phi_{\lambda,\boldsymbol{k}}^{\star}(\boldsymbol{r})\, F(\boldsymbol{p},\boldsymbol{r})\, \phi_{\nu,\boldsymbol{k}'}(\boldsymbol{r})\,, \tag{3.53}$$

containing the light–matter coupling operator

$$\begin{aligned} F(\boldsymbol{p},\boldsymbol{r}) = -e\boldsymbol{r}\cdot\sum_{n=0}^{\infty}\frac{1}{(n+1)!}\left[(\boldsymbol{r}\cdot\nabla_{\boldsymbol{r}'})^n\,\boldsymbol{E}(\boldsymbol{r}')\right]\Big|_{\boldsymbol{r}'=0} \\ -\frac{e}{2m_0}\sum_{l=0}^{\infty}\frac{l+1}{(l+2)!}\left\{\boldsymbol{p}\cdot\left[\boldsymbol{r}\times\left[(\boldsymbol{r}\cdot\nabla_{\boldsymbol{r}'})^l\,\boldsymbol{B}(\boldsymbol{r}')\right]\right]+\left[\boldsymbol{r}\times\left[(\boldsymbol{r}\cdot\nabla_{\boldsymbol{r}'})^l\,\boldsymbol{B}(\boldsymbol{r}')\right]\right]\cdot\boldsymbol{p}\right\}\Big|_{\boldsymbol{r}'=0}. \end{aligned} \tag{3.54}$$

In its most popular form, the light–matter interaction in Eq. (2.1) is given including only electric dipoles, e.g. $F(\boldsymbol{p},\boldsymbol{r}) = -e\boldsymbol{r}\cdot\boldsymbol{E}(\boldsymbol{0})$. Once the dipole-matrix element vanishes, such as is the case for rutile, it is necessary to include higher multipole contributions, such as electric- and magnetic-quadrupole interactions. In contrast to the band structure, these matrix elements are taken directly from the DFT calculations and depend on the field polarization. The DFT calculation reveals that magnetic dipole-matrix elements are vanishingly small and are therefore neglected.

3.3.3 Absorption

Apart from the mass anisotropy, the low-frequency dielectric constants of TiO_2 also show an extraordinary direction dependence with $\epsilon_1 = \epsilon_2 \equiv \epsilon_\perp = 111$ and $\epsilon_3 \equiv \epsilon_\parallel = 257$ [121]. Since in the derivation of the exciton wavefunctions (3.18), isotropic dielectric constants have been assumed for the Coulomb potential, Eq. (3.15) does not hold any more. However, a coordinate transformation as discussed in Section 2.1 can be applied so that the Coulomb potential remains isotropic. As a consequence, ϵ_{BG} and $\mu_\parallel$ have to be replaced according to $\epsilon_{\mathrm{BG}} \to \sqrt{\epsilon_\parallel\epsilon_\perp}$ and $\mu_\parallel \to \mu_\parallel\epsilon_\parallel/\epsilon_\perp$ in Eq. (3.15), which then can be used without further restrictions.

Since they constitute an orthonormal basis, it is possible to expand the microscopic polarization (2.42) into the exciton wavefunctions (3.1) via [10]

$$p_{\boldsymbol{k}} = \sum_\lambda p_\lambda\, \psi_\lambda^{\mathrm{R}}(\boldsymbol{k})\,, \qquad p_\lambda = \sum_\lambda p_{\boldsymbol{k}}\left[\psi_\lambda^{\mathrm{L}}(\boldsymbol{k})\right]^{\star}. \tag{3.55}$$

Here, diagonal excitons with $\boldsymbol{k}' = \boldsymbol{k}$ (which follows from $\boldsymbol{k}_0 = \boldsymbol{0}$) have been assumed, see Section 3.1. The change of basis (3.55) can be used to transform the dynamics of $p_{\boldsymbol{k}}$. A subsequent Fourier transform yields

$$p_\lambda(\omega) = \frac{\mathcal{F}_\lambda}{E_\lambda - \hbar\omega - \mathrm{i}\gamma_\lambda(\omega)}E(\omega)\,, \tag{3.56}$$

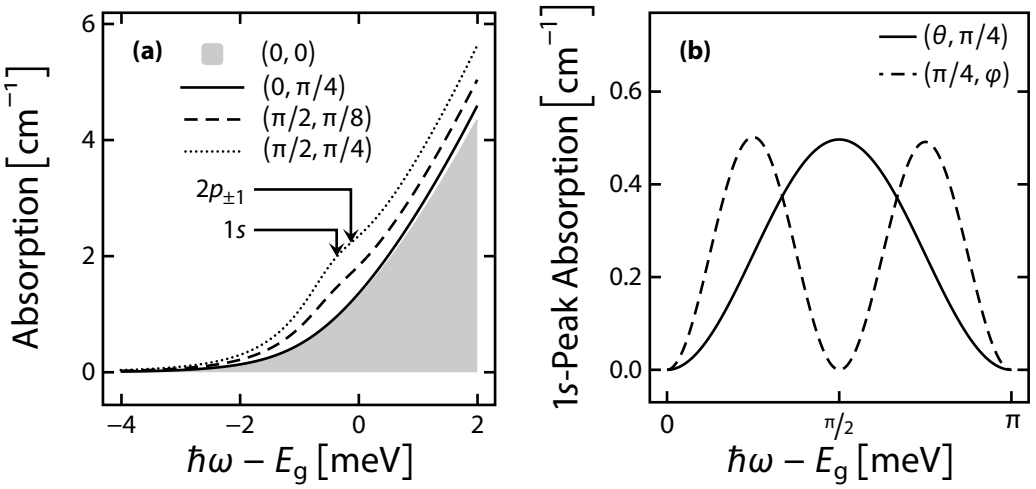

Figure 3.14 — (a) Near band gap optical Absorption of rutile TiO_2 for a light field polarized in the x–y plane and propagation angles (θ, φ). When light propagates along the z-axis (shaded area and solid line), the absorption is mainly dominated by electric dipole interactions. A propagation direction perpendicular to the z-axis (dashed and dotted lines) yields weak resonances which can be assigned to non-vanishing quadrupole interactions. (b) Resonance strength from the 1s exciton (spectral position is indicated in (a)) as a function of θ (solid) and φ (dashed), when the respective other angle is fixed.

with the generalized oscillator strength

$$\mathcal{F}_\lambda \equiv \sum_{\boldsymbol{k}} \left[\psi_\lambda^{\mathrm{R}}(\boldsymbol{k})\right]^\star F_{\mathrm{e},\boldsymbol{k}}^{\mathrm{h},\boldsymbol{k}}\,, \tag{3.57}$$

and $E(\omega)$ being the Fourier transform of $E(t)$.

The susceptibility follows from the macroscopic polarization (2.34),

$$P(\omega) = \sum_\lambda \mathcal{F}_\lambda p_\lambda(\omega)\,, \tag{3.58}$$

which yields the linear absorption

$$\alpha(\omega) = \frac{\omega}{\epsilon_0\sqrt{\epsilon_{\mathrm{BG}}}c_0} \sum_\lambda \frac{|\mathcal{F}_v|^2\,\gamma_\lambda(\omega)}{\left(E_\lambda - \hbar\omega\right)^2 + \gamma_\lambda^2(\omega)}\,, \tag{3.59}$$

using Eq. (2.50).

Next, the near-band gap optical absorption of TiO_2 is calculated via Eq. (3.59). The electric and magnetic fields are assumed to be polarized within the x–y plane and their propagation direction

is given by the polar and azimuthal angles θ and φ, respectively. More specifically, it is

$$\boldsymbol{E}(\boldsymbol{r}) = \mathrm{e}^{\mathrm{i}\boldsymbol{q}_E\cdot\boldsymbol{r}}\boldsymbol{e}_P\,, \qquad \boldsymbol{B}(\boldsymbol{r}) = \mathrm{e}^{\mathrm{i}\boldsymbol{q}_E\cdot\boldsymbol{r}}\big(\boldsymbol{q}_E \times \boldsymbol{e}_P\big)\,, \tag{3.60}$$

with the polarization

$$\boldsymbol{e}_P = x\boldsymbol{e}_x + y\boldsymbol{e}_y\,, \qquad x^2 + y^2 = 1\,, \tag{3.61}$$

and the propagation vector

$$\boldsymbol{q}_E = \big|\boldsymbol{q}_E\big|\Big(\sin\big(\theta\big)\cos\big(\varphi\big)\boldsymbol{e}_x + \sin\big(\theta\big)\sin\big(\varphi\big)\boldsymbol{e}_y + \cos\big(\theta\big)\boldsymbol{e}_z\Big)\,. \tag{3.62}$$

For the generalized oscillator strength (3.57), the wavefunctions are obtained by Eq. (3.18). Figure 3.14(a) shows the absorption for different $\boldsymbol{q}_E$, uniquely identified by the touple $\big(\theta, \varphi\big)$. If the light propagates parallel to the z-axis (shaded area and solid line), the corresponding quadrupole matrix elements have a vanishingly impact on the spectrum, since they are small for the applied polarization in the considered direction. Hence, the absorption follows almost entirely from electric dipole interactions. However, these couple predominantly excitons with $p_{\pm1}$ symmetry, which are degenerate due to the symmetry of the system. They do not show a significant angle dependency. Figure 3.14(a) also shows angles for which the light propagates away from the x, y, or z planes (dashed and dotted lines). Overall, the spectra are not drastically influenced changing $\big(\theta, \varphi\big)$, only a weak feature at the 1s ground state spectral position appears, a resonance which is dipole forbidden but quadrupole allowed.

To visualize that no propagation direction leads to a strong excitonic signal, Fig. 3.14(b) shows the 1s-peak absorption as a function of θ or φ while the respective other angle is fixed. As a general trend, whenever θ (φ) is varied, $\varphi = \pi/4$ ($\theta = \pi/2$) yields the strongest 1s-related absorption. Even using the optimal choice $(\pi/2, \pi/4)$ only results in a weak resonance. This is a consequence of the extraordinary small binding energy of $\tilde{E}_{1s} = -0.5\,\mathrm{meV}$ ($\tilde{E}_{2p_{\pm1}} = -0.1\,\mathrm{meV}$) for the 1$s$ ($2p_{\pm1}$) exciton due to the unusually large dielectric constants.

The experimental spectra presented in Refs. [126–128] show a distinct resonance 4 meV below the band gap, which is not reproduced in Fig. 3.14. Different conclusions have been drawn from the various authors about the origin of this resonance. While Pascual et al. claim that the excitonic signatures possess dipole forbidden but quadrupole allowed 1s symmetry, Amtout and Leonelli assign it to a weakly dipole allowed isotropic 2p state. To resolve this issue, a closer look at the dielectric constant is required.

When the band structure is obtained from ab-initio calculations, it is not straightforward to define wether the low or high frequency, or even some phenomenological dielectric constant between these should be used when the excitonic response is modeled [130]. This is particularly important if the high and low frequency components of the dielectric constant differ on a huge scale like in

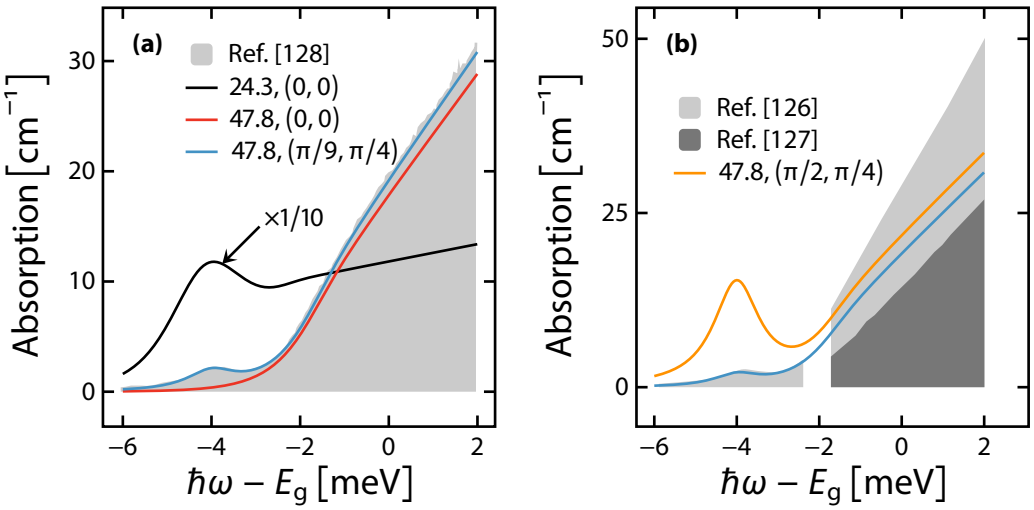

Figure 3.15 — Experimental and theoretical absorption spectra. The computed spectra are characterized by a set of ϵ and (θ, φ) containing the dielectric constant $\epsilon(\nu)$ according to Eq. (3.62) and propagation angles. To reproduce the experimental data, propagation according to $(\pi/9, \pi/4)$ and a dielectric constant of 47.8 is necessary (blue line). Other combinations do not reproduce the resonance at −4 meV or misevaluate its strength. No experimental data for a small region around −2 meV is provided as a consequence of the detection method.

TiO_2. Here, the high-frequency components are $\epsilon_\perp^\infty = 6.8$ and $\epsilon_\parallel^\infty = 8.4$, while the low-frequency constants are $\epsilon_\perp = 111$ and $\epsilon_\parallel = 257$. A pragmatic approach to cope with this issue is to obtain the dielectric constant as a linear interpolation between the low- and high-frequency limit according to

$$\tilde{\epsilon}_{\parallel/\perp}(\nu) = \epsilon_{\parallel/\perp} - \nu(\epsilon_{\parallel/\perp} - \epsilon_{\parallel/\perp}^\infty), \qquad \nu \in [0,1], \tag{3.63}$$

introducing the directionally averaged dielectric constant via $\epsilon(\nu) = \left[\tilde{\epsilon}_\parallel^2(\nu)\tilde{\epsilon}_\perp(\nu)\right]^{\frac{1}{3}}$. Tuning $\epsilon(\nu)$ in turn allows the adjustment of the exciton binding energies. Selecting either $\epsilon(\nu) = 24.3$ or $\epsilon(\nu) = 47.8$, the $2p_{\pm1}$ or $1s$ binding energy coincides with the experimentally observed signature 4 meV below E_g.

To study the implications of Eq. (3.62) on the absorption, Fig. 3.15(a) shows a comparison of $\alpha(\omega)$ for different sets of dielectric constants $\epsilon(\nu)$ and propagation angles (solid lines) to the experimental data from Ref. [128] (shaded area). Although for $\epsilon(\nu) = 24.3$ and propagation along the z-axis (black line), a resonance 4 meV below the band gap is clearly visible, the total scale and the continuum absorption is not successfully reproduced. In general, only changing the dielectric constants does not generate a signature at the appropriate spectra position while simultaneously

yielding a satisfactory agreement to the high-energy absorption tail. As an example, the absorption for $\epsilon(\nu) = 47.8$ and $\left(\theta = 0, \varphi = 0\right)$ is shown as a red line in Fig. 3.15. Moreover, it is difficult to reproduce the experimentally observed energetic position using values different from $\epsilon(\nu) = 47.8$. At the same time, the angles determine the strength of the resonance and in general, several combinations $\left(\theta, \varphi\right)$ can be found to reproduce the overall shape of the absorption, e.g. the choice $\epsilon(\nu) = 47.8$, $\theta = \pi/9$, and $\varphi = \pi/4$ (blue line) provides excellent agreement with the experiment.

Next, the theoretically obtained spectra are compared the experiments from Refs. [126] and [127]. Again, the best agreement between experiments and theory can be obtained with $\epsilon(\nu) = 47.8$ and $(\pi/9, \pi/4)$ (blue line). Additionally, $\epsilon(\nu) = 47.8$ and $(\pi/2, \pi/4)$ (orange line) is shown, which overestimates the 1*s* resonance strength. The continuum absorption settles in between the different experiments in both cases. Generally, it is only possible to reconstruct the excitonic resonance under the assumption that its origin is the 1*s* exciton. In other words, $\epsilon(\nu) = 47.8$ is a prerequisite.

To conclude this Section, a combination of DFT and the CE approach is presented and applied to calculate the near-band gap optical absorption of rutile. For this purpose, it is necessary to include electric dipole and quadrupole interactions. The corresponding matrix elements and single-particle energies are provided by DFT calculations. Since the band structure is highly parabolic with strong mass anisotropy, it has been replaced using the effective-mass approximation, allowing to obtain the wavefunctions as described in Section 3.1.1. Those can be used to calculate the optical absorption, which reveals that the quadrupole interaction in rutile is highly polarization and propagation-direction dependent. Experimentally available excitonic signatures cannot be reproduced by omitting quadrupole interactions. In contrast, a good agreement between experiment and theory can be obtained including quadrupole interactions via a tuning of the dielectric constant and propagation angles. The origin of the resonance observed in various experiments can be assigned to be the 1*s* exciton.

4 Enhancement of Optical Transients in Germanium Quantum Wells

Semiconductors with an indirect band gap have attracted the interest of scientists involved in ultrafast spectroscopy due to their suitability to study scattering mechanisms [96, 97]. In this Section, the pump–probe absorption spectra of Ge/SiGe QWs are compared to those from (Ga,In)As/GaAs, which differ fundamentally under similar excitation conditions. While the Ge QWs show distinct coherent side bands, both slightly below and above the 1*s*-excitonic resonance, such features are completely absent in (Ga,In)As QWs.

Time-resolved spectroscopy represents an excellent tool to obtain information about carrier dynamics in semiconductors. Using ultrashort pulses generated by lasers, it is possible to study processes that are as short as 10^{-16} s [131]. A well-suited method to study ultrafast phenomena is pump–probe spectroscopy. Here, a strong pump pulse excites the semiconductor sample. This excited state is then probed by a weak second pulse called probe, which is temporally separated by a delay time τ with respect to the pump. Therefore, pump–probe spectroscopy detects modifications to the probe pulse induced by an excitation of the system. Comparing a system that has not been excited by a preceding pump pulse to an excited one yields information about the polarization decay time, gain, absorption, the optical Stark effect, carrier-recombination times, and hot-carrier relaxation [131]. Naturally, the pump–probe signal is detected in direction of the probe. But it is also possible to detect signals in other directions. Figure 4.1(a) shows a schematic drawing of the process, indicating the pump–probe and four-wave mixing (FWM) detection directions $\boldsymbol{k}_\mathrm{p}$ and $2\boldsymbol{k}_\mathrm{p} - \boldsymbol{k}_\mathrm{x}$, respectively. Experiments which detect the FWM signal provide information about the spatial diffusion of charge carriers as well as homogenous and inhomogeneous broadening [132].

4.1 Experiment

The experiment was conducted using a strong 80 fs pump pulse from an optical-parametric amplifier (OPA) while the probe pulse stems from a white-light super-continuum source. Both are driven by a regenerative 1 kHz Ti:sapphire amplifier. The pump pulse excites the samples at the Γ point and energetically resonant into the 1*s*-excitonic ground-state. A spectral extremely broad probe pulse is used to detect the absorption over a wide range of energies.

Schematics of the two investigated multi-QW samples are shown in Fig. 4.1. Frame (b) depicts the sample which consists of 50 compressively strained Ge QWs with a thickness of d_QW = 10 nm.

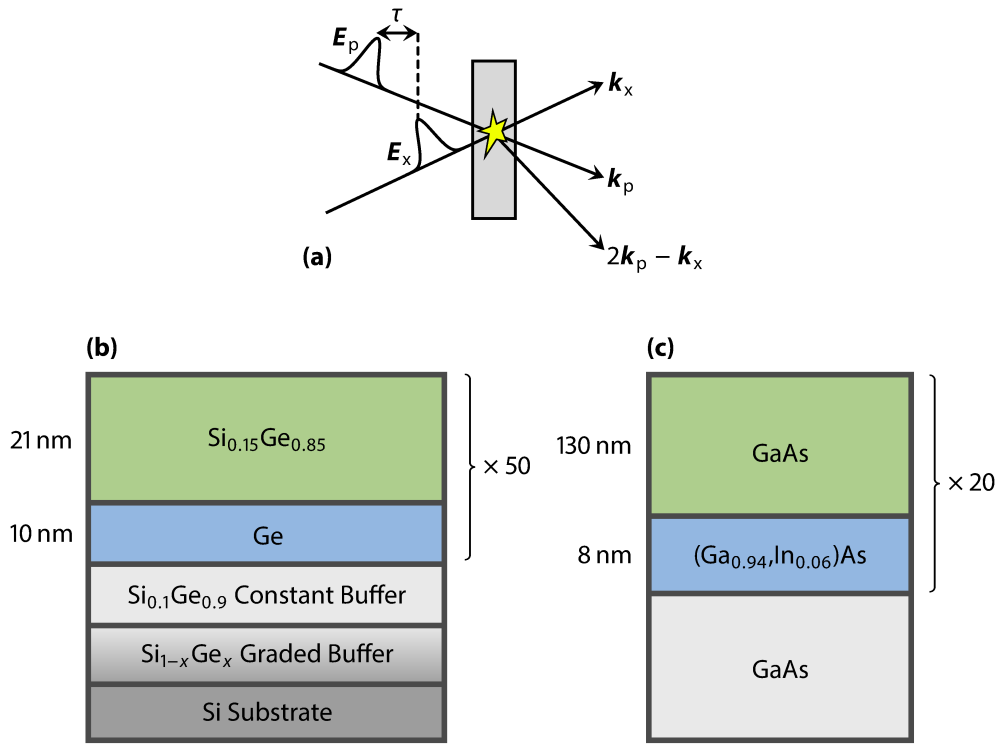

Figure 4.1 — (a) A schematic drawing of an experiment involving two pulses, which are delayed by a time τ. Due to the induced polarization lattice (yellow star), the pulses are diffracted into different directions. Detecting either in the $\boldsymbol{k}_p$ or $2\boldsymbol{k}_p - \boldsymbol{k}_x$ direction yields the pump–probe or four-wave-mixing signal. (b) Sample structure for the Ge QW. (c) Sample structure for the Ga,In)As QW.

The barriers consist of 21 nm thick $Si_{0.15}Ge_{0.85}$. Compressive (tensile) strain in the QW (barrier) layers is a result of the relaxed SiGe buffer which is linearly graded from pure Si to $Si_{0.1}Ge_{0.9}$ and breaks the degeneracy of the hh and lh valence bands. Thus, the highest hh states lie energetically above those of the lh band [133]. The sample was grown by low-energy plasma-enhanced chemical-vapor deposition (LEPECVD) [134] on a (001)-oriented Si substrate.

Figure 4.1(c) shows the second sample, which consists of 20 $(Ga_{0.94},In_{0.06})As$ QW layers between GaAs barrier layers. The QWs (barriers) have a thickness of $d_{QW} = 8\,nm$ (130 nm). Again, the highest hh states energetically lie above the lh band due to compressive strain. This sample was grown by metalorganic vapor phase epitaxy (MOVPE) [135].

Figure 4.2 shows the pump–probe absorption spectra obtained at low temperature ($T = 10\,K$) and various delay times for the Ge and (Ga,In)As sample in Frames (a) and (b), respectively. The excitation power is $P = 0.064\,mW$ ($P = 0.6\,mW$) for the (Ga,In)As (Ge) sample. For Ge, additional features around the 1s–hh1 transition resonance on both its lower and higher energy side

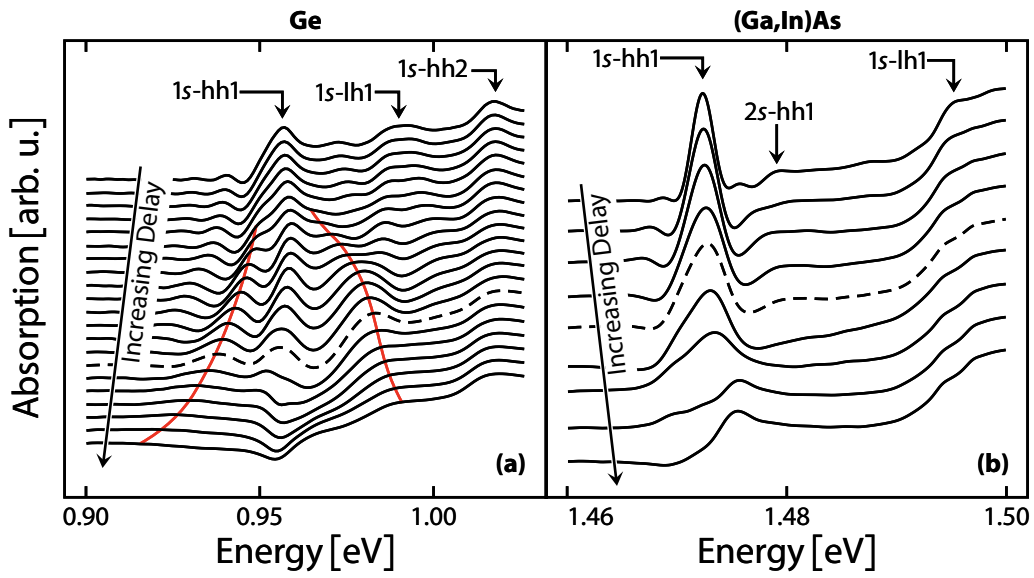

Figure 4.2 — Experimental pump–probe absorption spectra for (a) Ge and (b) (Ga,In)As QWs. Excitonic transitions are marked by arrows and indicate the respective end state. The delay between pump and probe beam increases from top (probe arrives before the pump) to bottom. The spectra plotted with dashed lines indicate the time where pump and probe field arrive simultaneously, e.g. $\tau = 0$ fs. For Ge, the top (bottom) spectrum is obtained at $\tau = -310$ fs ($\tau = 120$ fs). For (Ga,In)As, the respective spectra are measured for $\tau = -1$ ps and $\tau = 1$ ps, respectively. The red line in Frame (a) acts as a guide to the eye to identify the coherent side bands. All spectra have been vertically shifted for visibility.

can be observed for delay times $-200\,\text{fs} < \tau < 20\,\text{fs}$ (red lines). With increasing delay time, these additional resonances shift energetically away from the center 1*s*–hh1 transition energy. Simultaneously, they become more pronounced until they disappear after $\tau > 20$ fs. Due to resonant pumping, the 1*s* resonance itself only shows minor energetic shifts. It also becomes weaker with increasing delay, implying a growing occupation of the ground state which leaves fewer states unoccupied and available for absorption events. Additionally, all spectra at negative delay times show superimposed oscillations. These coherent oscillations occur only if the probe pulse arrives during the rising part of the excitation field [136]. Their origin is a transient population grating which is created coherently by both the pump and probe pulses. Coherent oscillations are manifestations of the total interference pattern generated during the overlap of the two pulses by those parts that are scattered into the probe beam direction [137].

Figure 4.2(b) presents similar pump–probe spectra for the (Ga,In)As sample. In contrast to Ge, these spectra exclusively exhibit broadening of the 1*s*-excitonic resonance and EID effects.

Although the experiment truly constitutes a many-body configuration due to the numerous mo-

mentum states involved via the band structure, a resonant excitation of the 1*s*-hh1 transition somehow mimics a two-level system. Therefore, the next Section discusses the pump–probe absorption of a two-level system before a microscopic many-body analysis is conducted.

4.2 Two-Level System

In his famous papers, Mollow described the power spectrum [138], stimulated emission, and absorption [139, 140] line shapes of a resonantly driven two-level system. He found that the fluorescence spectrum shows a triplet structure with a resonant center peak and two side bands as a consequence of the light-field induced level splitting of the two states. Accordingly, this structure is named Mollow triplet. The counterpart regarding absorption also exhibits three distinct resonances. Studied in atomic systems [141, 142] or excitons [4, 143], the effect itself is called optical Stark effect.

In a sense, the experiments described in the previous Section are inspired by an arrangement similar to Mollow's setup. The hh1 and the 1*s* exciton ground state constitute the two-level system in this analogy, which is resonantly excited in the experiments. In his original work, Mollow investigated the pump–probe absorption spectrum for two continuous wave (cw) fields. The experiments studied in this Section use pulses to excite and probe the sample. Hence, it is instructive to investigate any modifications to Mollows results using pulsed instead of cw fields.

Mollows original equations are identical to the optical Bloch equations (OBEs) [8] and read

$$\hbar \frac{\partial}{\partial t} \rho_{10} = -\mathrm{i}\, \epsilon_{10}\, \rho_{10} - \mathrm{i}\Omega(t) \left(2\rho_{11} - 1\right) - \kappa\, \rho_{10}\,, \tag{4.1}$$

$$\hbar \frac{\partial}{\partial t} \rho_{11} = -2\, \mathrm{Im}\left[\Omega(t)\, \rho_{10}^{\star}\right] - \eta\, \rho_{11}\,, \tag{4.2}$$

assuming that transitions between ground state $|0\rangle$ and excited state $|1\rangle$ are mediated via the real-valued transition dipole-matrix element $d \equiv e\, \langle 1|\boldsymbol{r} \cdot \boldsymbol{e}_{\mathrm{P}}|0\rangle$. The Rabi energy is defined as $\Omega(t) = dE(t)$ with the applied electric field $\boldsymbol{E}(t) = E(t)\boldsymbol{e}_{\mathrm{P}}$, and the energetic separation between the two states $\epsilon_{10} = \epsilon_1 - \epsilon_0$. Furthermore, the constants η and κ have been introduced to account for relaxation of diagonal and off-diagonal coefficients of the density-matrix elements ρ_{ij}.

In order to obtain a Mollow-absorption spectrum (MAS) for classical excitation ($l = \mathrm{x}$) and probe ($l = \mathrm{p}$) fields E_l, the carrier-envelope phases φ_l are introduced via

$$E(t) \to E_l\left(t, \varphi_l\right) = F_l(t) \cos\left(\omega_l t + \varphi_l\right), \tag{4.3}$$

where F_l denotes the envelope function and ω_l its central frequency. Without loss of generality, the envelope phase of the excitation field can be chosen as $\varphi_{\mathrm{x}} = 0$. Then, $\varphi_{\mathrm{p}} \equiv \varphi$ is a measure for the shift of the probe's carrier envelope with respect to the one of the pump.

Next, the quantity $\rho_{10}^{(\mathrm{x})}$ is introduced, describing the transition probability between the two states

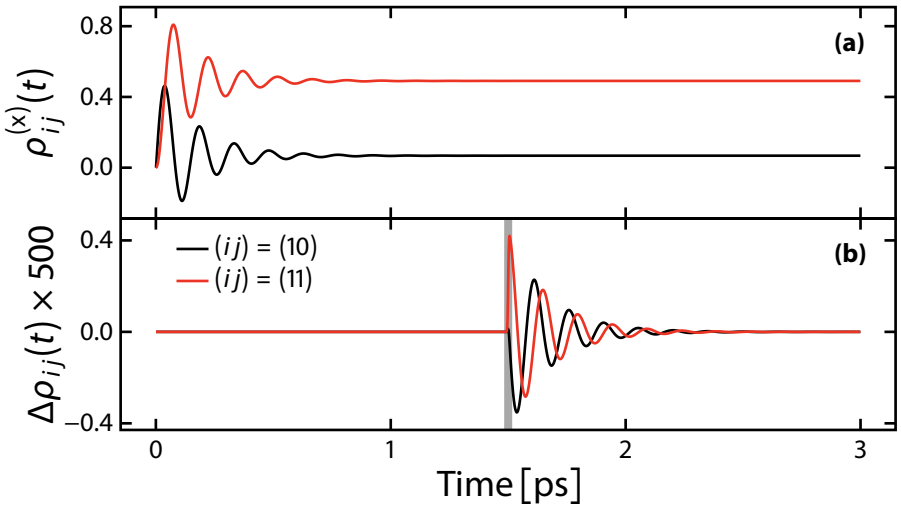

Figure 4.3 — Dynamics of density-matrix elements of a two-level system. Black (red) lines indicate off-diagonal (diagonal) elements. (a) Quantities that are generated by a single cw excitation field. (b) Matrix elements that result from a probe pulse in the presence of that same cw field are shown. A grey-shaded area marks the time of the probe's arrival.

when only the excitation field acts upon the system. Similarly, $\rho_{10}^{(\mathrm{x+p})}$ is obtained when both the excitation and probe field are present. Once these transition probabilities are known, the probe absorption in the presence of a pump field α_p follows from [137]

$$\alpha_\mathrm{p}(\omega,\varphi) \propto \omega\,\mathrm{Im}\left[\frac{\int \mathrm{d}t\,\Delta\rho_{10}(t,\varphi)\,\mathrm{e}^{\mathrm{i}\omega t}}{\int \mathrm{d}t\,E_\mathrm{p}(t,\varphi)\,\mathrm{e}^{\mathrm{i}\omega t}}\right], \tag{4.4}$$

with

$$\Delta\rho_{ij}(t,\varphi) = \rho_{ij}^{(\mathrm{x+p})}(t,\varphi) - \rho_{ij}^{(\mathrm{x})}(t)\,, \tag{4.5}$$

describing the probe-matrix element while an excitation field is present.

The temporal evolution of the density-matrix elements $\rho_{10}^{(\mathrm{x})}$ and $\rho_{11}^{(\mathrm{x})}$ are depicted in Fig. 4.3(a). A cw field is switched on at $t = 0\,\mathrm{ps}$ and continuously acts on the system. All diagonal elements approach 0.5 so that $\rho_{11}^{(\mathrm{x})}(t) + \rho_{00}^{(\mathrm{x})}(t) = 1$ at all times t (not shown). Off-diagonal elements tend to leave a small non-vanishing component in the system due to the excitation field that does not decay. Frame 4.3(b) presents the appropriate probe dynamics in the presence of a pump field. The probe arrives at $t = 1.5\,\mathrm{ps}$ (grey area) and both elements vanish.

Since the experimental setup does not allow phase-stable pulses, the measured spectrum $\tilde{\alpha}_\mathrm{p}$ is

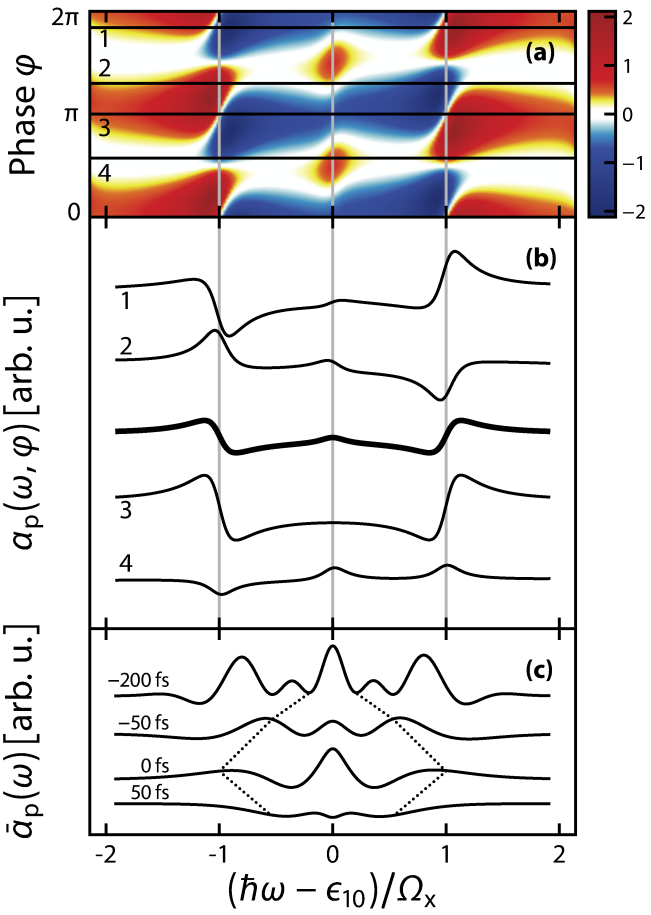

Figure 4.4 — (a) Absorption of a continuously driven two-level system according to Eq. (4.4). (b) Spectra according to horizontal cuts as indicated by the black lines and numbers. The thick-solid line is the analytical solution derived in Ref. [140]. (c) Absorption for pulsed excitation at different pump–probe delay times marked on the left side of the spectra. As a guide to the eye, the dotted line indicated the time dependent Rabi energy Ω_x of the excitation pulse.

actually given by averaging over all envelope phases, yielding

$$\tilde{\alpha}_p(\omega) \propto \int_0^{2\pi} d\varphi\, \alpha_p(\omega,\varphi)\,. \tag{4.6}$$

Figure 4.4(a) presents the phase-dependent spectra according to Eq. (4.4) as a contour plot. The cw excitation field has a field strength of 40 MV m^{-1} while the weak test pulse is assumed to be a Gaussian with a FWHM of 3.6 fs. A large delay of $\tau = 2$ ps needs to be applied so that the system has reached equilibrium. Dephasing times of $\kappa = \eta = 170$ fs and a dipole-matrix element of $d = 7\,e$ Å

have been used. The energy separation of the states is $\epsilon_{10} = 0.96\,\mathrm{eV}$. Numbered horizontal lines indicate phases φ for which the spectra $\alpha_\mathrm{p}(\omega, \varphi)$ are shown in Fig. 4.4(b) as thin black lines. Non of these spectra are identical to Mollows analytical result (not shown). However, it can be retrieved by the phase averaged result $\bar{\alpha}_\mathrm{p}(\omega)$, which is plotted in the center as a thick line. Grey-vertical lines indicate ϵ_{10} as well as the Rabi energy of the excitation pulse $\Omega_\mathrm{x} = d\,E_\mathrm{x} = 28\,\mathrm{meV}$, which define the zero-crossing near the Mollow sidebands of the phase-averaged result. As an intermediate result it is noted that Mollows analytical result, which is obtained using cw pump and probe beams, requires an envelope-phase averaging when switching to a pulsed probe field. It is the subject of current research to analytically find the deeper reason why a phase-averaging procedure must be performed to match the dynamical and analytical results [144].

As the next step towards the true experimental conditions, the system is excited with a pulsed pump field. Its temporal duration is defined by the FWHM of a Gaussian and chosen to be 190 fs. Figure 4.4(c) shows the resulting probe absorption spectra for delay times τ indicated therein. At early negative times, when the probe arrives before the pump pulse, strong nonlinear transients occur. These effects are not purely coherent oscillations since they do not decay linearly. Approaching $\tau = 0\,\mathrm{fs}$, the absorption features residues of the line shapes observed in a MAS, containing one central peak and two side peaks in the vicinity of the Rabi energy $\Omega_\mathrm{x}(t = \tau) = dE_\mathrm{x}(t = \tau)$ (dotted line). For $\tau = 50\,\mathrm{fs}$, both states are almost equally occupied, prohibiting strong absorbance.

Experimentally, the MAS has been measured in systems that closely resemble a two-level system, e.g. in atoms [145], incoherently excited cavities [146], or QDs [147, 148]. However, measuring the phase sensitivity requires a phase-stable laser system [149]. Additionally, a single two-level system would have to be isolated, since a spatial distribution would destroy any phase coherence between individual systems. Although such a measurement is extremely challenging, it has been demonstrated in QDs [113].

4.3 Quantum-Well System

In order to calculate the pump–probe absorption spectrum for a QW system, the microscopic many-body theory outlined in Section 2.5 is used. To concentrate on the relevant physics around the 1*s*-excitonic resonance, it is sufficient to consider a two-band model, assuming parabolic bands according to Eq. (2.14). Therefore, only the e1 and hh1 subbands are taken into account explicitly, following from strain arguments discussed earlier. The SBEs then take the form

$$\mathrm{i}\hbar\frac{\partial}{\partial t}p^{\mathrm{hh1,e1}}_{\boldsymbol{k}_\parallel} = \tilde{\epsilon}_{\boldsymbol{k}_\parallel}p^{\mathrm{hh1,e1}}_{\boldsymbol{k}_\parallel} - \left(1 - f^{\mathrm{e1}}_{\boldsymbol{k}_\parallel} - f^{\mathrm{hh1}}_{\boldsymbol{k}_\parallel}\right)\Omega^{\mathrm{e1,hh1}}_{\boldsymbol{k}_\parallel} + \mathrm{i}\hbar\Gamma^{\mathrm{hh1,e1}}_{\boldsymbol{k}_\parallel}, \tag{4.7}$$

$$\frac{\partial}{\partial t}f^{\mathrm{e1}}_{\boldsymbol{k}_\parallel} = -\frac{2}{\hbar}\,\mathrm{Im}\left[\Omega^{\mathrm{e1,hh1}}_{\boldsymbol{k}_\parallel}\left(p^{\mathrm{hh1,e1}}_{\boldsymbol{k}_\parallel}\right)^\star\right] + \Gamma^{\mathrm{e1,e1}}_{\boldsymbol{k}_\parallel}, \tag{4.8}$$

$$\frac{\partial}{\partial t}f^{\mathrm{hh1}}_{\boldsymbol{k}_\parallel} = -\frac{2}{\hbar}\,\mathrm{Im}\left[\Omega^{\mathrm{e1,hh1}}_{\boldsymbol{k}_\parallel}\left(p^{\mathrm{hh1,e1}}_{\boldsymbol{k}_\parallel}\right)^\star\right] + \Gamma^{\mathrm{hh1,hh1}}_{\boldsymbol{k}_\parallel}, \tag{4.9}$$

where

$$\tilde{\epsilon}_{\boldsymbol{k}_\parallel} = \tilde{\epsilon}^{\mathrm{e}}_{\mathrm{el,el}} + \tilde{\epsilon}^{\mathrm{h}}_{\mathrm{hh1,hh1}} = \epsilon_{\mathrm{el},\boldsymbol{k}_\parallel} + \epsilon_{\mathrm{hh1},\boldsymbol{k}_\parallel} - \sum_{\boldsymbol{k}'_\parallel} \left(V^{\mathrm{el,el,el,el}}_{\boldsymbol{k}_\parallel - \boldsymbol{k}'_\parallel} f^{\mathrm{el}}_{\boldsymbol{k}_\parallel} + V^{\mathrm{hh1,hh1,hh1,hh1}}_{\boldsymbol{k}_\parallel - \boldsymbol{k}'_\parallel} f^{\mathrm{hh1}}_{\boldsymbol{k}_\parallel} \right). \tag{4.10}$$

The band dispersions $\epsilon_{\lambda,\boldsymbol{k}_\parallel}$ are assumed to be parabolic according to Eq. (2.14). Additionally, a self-consistent coupling of the semi-classical field is considered via Maxwell's equation [150]

$$\left[\frac{\partial^2}{\partial z^2} - \frac{\epsilon_{\mathrm{BG}}}{c_0^2} \frac{\partial^2}{\partial t^2} \right] E(t) = \mu_0 \delta(z) \frac{\partial^2}{\partial t^2} P(t)\,, \tag{4.11}$$

where a infinitely thin QW layer has been assumed. Equations (4.7)–(4.11) constitute the Maxwell-semiconductor Bloch equations [10].

To further simplify the discussion, a box-like confinement potential with infinitely high walls is assumed, so that the confinement functions (2.17) are given by

$$\xi_{\mathrm{el}}(z) = \xi_{\mathrm{hh1}}(z) = \sqrt{\frac{2}{d_{\mathrm{QW}}}} \sin\left(\frac{\pi}{d_{\mathrm{QW}}} z \right), \tag{4.12}$$

for a box that extends from $-d_{\mathrm{QW}}$ to $+d_{\mathrm{QW}}$. Since the dipole-matrix element usually shows only a weak $\boldsymbol{k}_\parallel$ dependence [10], it is assumed to be momentum independent, e.g. $d^{\mathrm{el,hh1}}_{\boldsymbol{k}_\parallel} = d^{\mathrm{el,hh1}} = \text{const.}$

4.3.1 Dephasing

The band structure of Ge and (Ga,In)As are of intrinsically different nature, giving rise to individual dephasing mechanisms. Ge is an indirect semiconductor and after optical excitation at the Γ point, carriers are scattered into the L valley on a time scale of a few hundred femto seconds. In (Ga,In)As, which is a direct semiconductor, the carriers remain at the Brillouin-zone center until they eventually recombine.

In that regard, the scattering contributions $\Gamma^{\lambda,\nu}_{\boldsymbol{k}_\parallel}$ in the SBEs are modeled differently. For a direct semiconductor at low temperatures, the dephasing mechanism is dominantly provided by carrier–carrier scattering due to a near absence of phonons. Therefore, the diffusive model [12] is applied to simulate the consequences of this Coulomb-induced scattering processes for $p^{\mathrm{hh1,el}}_{\boldsymbol{k}_\parallel}$ via

$$\Gamma^{\mathrm{hh1,el}}_{\boldsymbol{k}_\parallel} = -\frac{1}{\tau_{\mathrm{diff}}} \left[p^{\mathrm{hh1,el}}_{\boldsymbol{k}_\parallel} - \frac{1}{2\pi} \int_0^{2\pi} \mathrm{d}\theta\, p^{\mathrm{hh1,el}}_{\boldsymbol{k}_\parallel + \boldsymbol{K}_\theta} \right]. \tag{4.13}$$

Equation (4.13) describes the redistribution of the polarization with momentum $\boldsymbol{k}_\parallel$ onto a sphere with radius $\boldsymbol{K}_\theta$, a typical momentum exchange in a Coulomb-scattering process [12]. Additionally, the decay constant τ_{diff} is introduced. Both τ_{diff} and $\boldsymbol{K}_\theta$ ultimately must be extracted from exper-

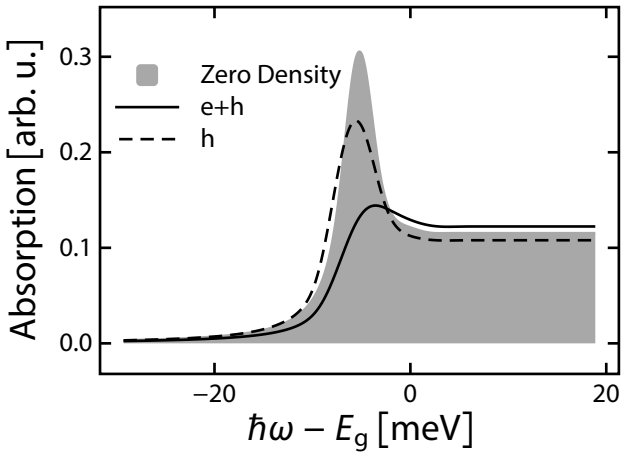

Figure 4.5 — Absorption for Ge at 40 K. A setting with electrons and holes contributing to spectral broadening (solid line) is compared to one where only holes conduce to the density-induced dephasing (dashed line). The total density is $n = 5 \times 10^9$ cm^{-2}.

iments. This model has been successfully applied to describe EID effects in optical [10] and THz spectroscopy [151]. Distributions are scattered according to

$$\Gamma^{\mathrm{e1,e1}}_{\boldsymbol{k}_\parallel} = -\frac{f^{\mathrm{e1}}_{\boldsymbol{k}_\parallel}}{\tau_\mathrm{e}}, \qquad \Gamma^{\mathrm{hh1,hh1}}_{\boldsymbol{k}_\parallel} = -\frac{f^{\mathrm{hh1}}_{\boldsymbol{k}_\parallel}}{\tau_\mathrm{h}}, \tag{4.14}$$

which describes a static decay with the time constants τ_e and τ_h. Equation (4.14) is appropriate to describe the distribution dephasing for both direct and indirect semiconductors. It is noted that in this Section, all broadening effects are simulated via the decay constants such that the spectra are not convoluted with a Gaussian as described in Section 2.6.

In indirect semiconductors it can be expected that phonons provide the prevalent dephasing contribution. This is a consequence of momentum conservation during the redistribution of carriers into the indirect energy minimum. In the simplest approximation, phonon scattering can be modeled using a constant scattering similar to Eq. (4.14) via

$$\Gamma^{\mathrm{hh1,e1}}_{\boldsymbol{k}_\parallel} = -\frac{p^{\mathrm{hh1,e1}}_{\boldsymbol{k}_\parallel}}{\tau_p}. \tag{4.15}$$

At the same time, density-induced dephasing effects become weaker when the inter-valley scattering is fast since the scattering partners become separated in momentum space. To substantiate that EID effects are dramatically decreased once the electron-scattering partner has been separated from the hole, Fig. 4.5 shows the absorption of Ge at the level of the second-Born approximation [152] using numerical matrix inversion. For this purpose, carrier distributions are assumed

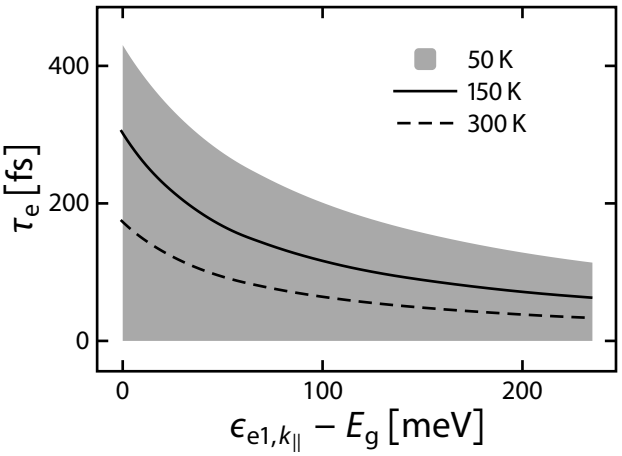

Figure 4.6 — Electron scattering times for a momentum path from the Γ to the L valley at different temperatures. They have been obtained by an empirical pseudopotential method.

to follow Fermi–Dirac statistics. Used material parameters for Ge are summarized in Table 4.1 and the temperature is $T = 40\,\mathrm{K}$. The shaded area depicts an unexcited system and serves as a reference to identify broadening effects. If both electrons and holes contribute to the dephasing, $f^{\mathrm{el}}_{\boldsymbol{k}_\parallel} \neq 0 \neq f^{\mathrm{hh1}}_{\boldsymbol{k}_\parallel}$, the absorption for a total density of $n = 5 \times 10^9\,\mathrm{cm}^{-2}$ is shown as a solid line. A considerable broadening of the 1s-excitonic resonance is observed. In contrast, the dashed line depicts a situation where it is assumed that electrons have been scattered away from the Γ valley, so that they effectively disappear completely. Then, only hole contribute to the dephasing, e.g. $f^{\mathrm{el}}_{\boldsymbol{k}_\parallel} = 0$. Although the same density for the holes was applied, the broadening and reduction in oscillator strength is much less prominent.

Besides experimental evidence for an efficient $\Gamma \rightarrow L$ depopulation in Ge [96, 97], the electron dephasing time τ_e has been calculated for confirmation. Using an empirical pseudopotential method [153, 154], Fig. 4.6 shows the resulting scattering rates as a function of energy for the momentum path $\Gamma \rightarrow L$. They are found to be below 500 fs for various temperatures.

	E_g/eV	m_{e1}/m_0	m_{hh1}/m_0	ϵ_{BG}	τ_p/ps	τ_e/ps	τ_h/ps	$d^{e1,hh1}/e$ Å
Ge	0.96	0.041	0.33	16	0.17	0.3	7000	7
(Ga,In)As	1.48	0.0665	0.457	13.74	-	2000	2000	5

Table 4.1 — Material parameters used in the computations for Ge and (Ga,In)As. They are mainly taken from Refs. [8] and [152] or extracted from experiments.

4.4 Experiment-Theory Comparison

The previous Section discussed that it is justified to use a diffusive Coulomb scattering for direct and a constant dephasing for the polarization of indirect semiconductors. Additionally, the time it takes electrons to be effectively removed from the system is much shorter in Ge due to fast intervalley scattering.

In this Section, the microscopic many-body dynamics are solved simultaneously with Maxwell's equation (4.11). The absorption is computed equivalently to the two-level system, e.g. similar to Eq. (4.6), as the average over envelope-phase dependent responses. Figure 4.7 presents the resulting pump–probe absorption spectra for both samples and selected delay times. The top row shows the response of the (Ga,In)As sample whereas the bottom row those of the Ge QW. In the left (right) column, experimental (theoretical) spectra are presented.

As described in the previous Section, the diffusive Coulomb scattering (4.13) is used to model the (Ga,In)As sample. Since a scattering process becomes both more likely and intense with increasing number of carriers, it must be density dependent. The density sensed by the probe pulse is the amount of carriers, which have been created via the pump pulse until the moment the probe arrives, e.g. the delay time τ. Consequently, the variables τ_{diff} and K_θ introduced by the diffusive model depend on the delay time or equivalently, the density. Therefore, K_θ and $\hbar/\tau_{\text{diff}}$ are presented in Fig. 4.8(a) and (b) as a function of density. Their values are chosen to reproduce the experimental data as best as possible and follow a monotonic behavior. As predicted, the Coulomb-exchange momentum enhances with increasing density, while the scattering time decreases. Using the presented choice yields an excellent agreement between experimental and theoretical spectra. A comparison between experimental (left column) and theoretical spectra (right column) is shown in Fig. 4.7(a) and (b) for the (Ga,In)As (top row) and Ge QW sample (bottom row), respectively. When the probe arrives much earlier than the pump, only coherent oscillations are visible. With increasing delay, the density experienced by the probe rises and EID effects occur so that the 1s resonance becomes much broader. As a consequence of the density-induced renormalization of the band gap, the resonance additionally shifts slightly to higher energies. Once the dephasing model is replaced by a purely phonon-induced scattering (4.15), the spectra exhibit a similar triplet structure as observed in Ge (not shown).

Similarly, the diffusive model does not produce any features besides weak coherent oscillations when using Ge values. On the other hand, the experimental triplet structure is reproduced to a high degree of agreement when a purely phonon-based scattering is assumed. Figure 4.7(c) and (d) present the resulting experimental and theoretical data, respectively. Coherent oscillations can be observed at large negative delay times. Strong nonlinear transients occur around $\tau = -210\,\text{fs}$ and form the triplet structure together with 1s resonance. For $\tau > 0\,\text{fs}$, the system shows gain. This behavior is the many-body manifestation of the effects observed in the two-level system discussed in Section 4.2.

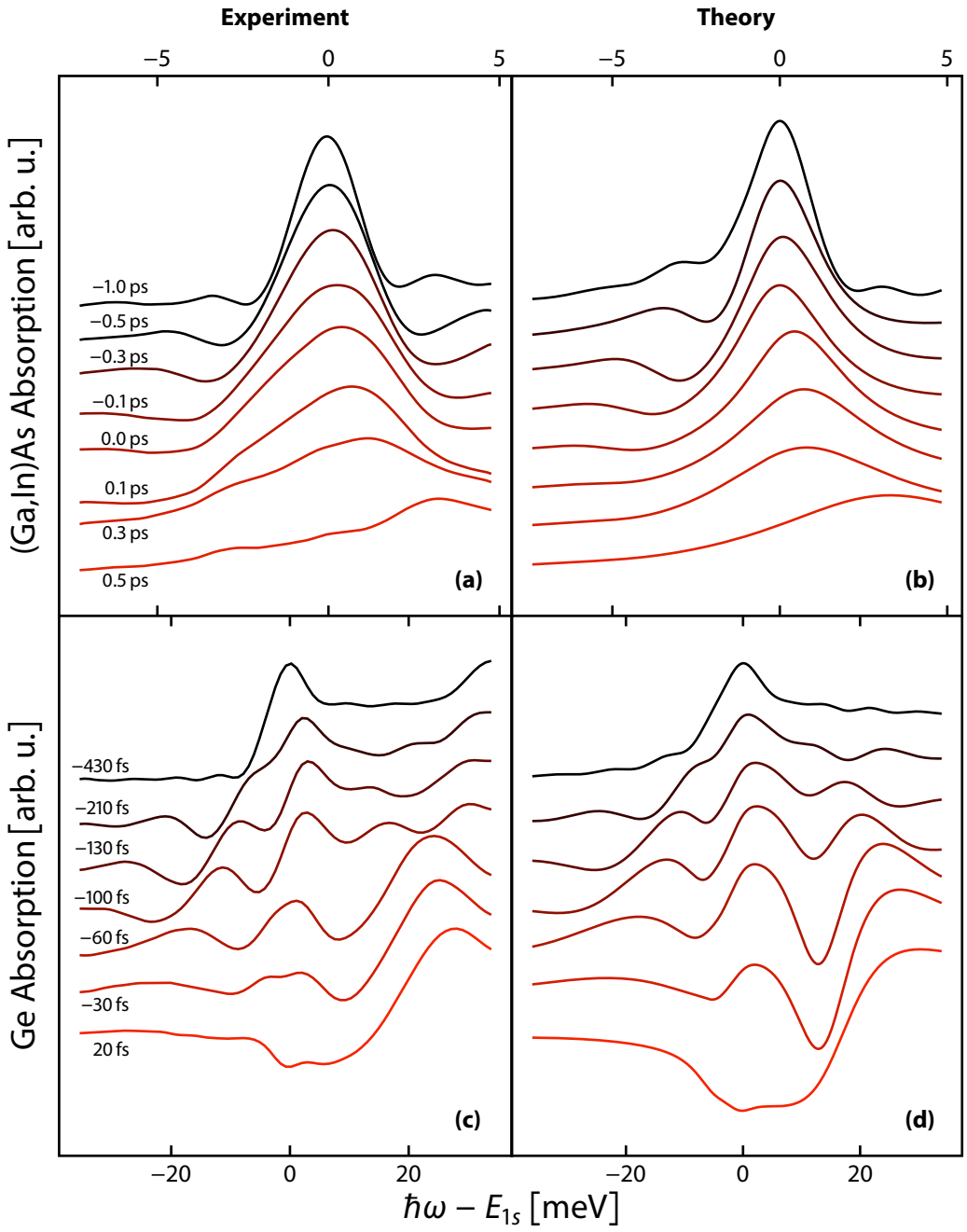

Figure 4.7 — Comparison of experimental (left column) and theoretical (right column) pump–probe absorption spectra. Different delay times are compared for the (Ga,In)As (top row) and Ge sample (bottom row). For (Ga,In)As, the used diffusive Coulomb scattering variables τ_{diff} and K_θ as a function of density are shown in Fig. 4.8(a) and (b), respectively.

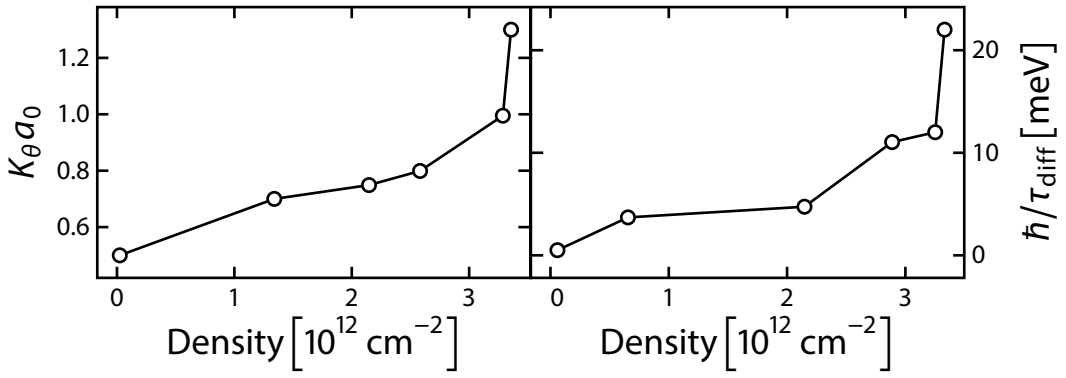

Figure 4.8 — Diffusive variables as a function of density (circles). (a) Coulomb-exchange momentum. (b) Diffusive scattering rate. The solid lines act as a guide to the eye.

It has been demonstrated in this Section, that a resonantly driven two-band semiconductor shows residuals of a MAS in the form of strong coherent transients, if both the pump and probe beam are pulsed light fields. Furthermore, the dephasing model determines if such residuals can be observed in a system or not. Although present, it is not possible to detect them in (Ga,In)As since Coulomb scattering processes dominante the dephasing mechanism so that EID effects characterize the pump–probe response. Conversely, these coherent transients are enhanced if the main scattering process is provided by phonons. Since this is the case for Ge, where electrons are quickly scattered into the *L* valley, residues of a MAS can be observed.

5 Optical Properties of Highly Mismatched Alloys

Today, semiconductor heterostructures are commonly used in a variety of popular solid-state electronic devices such as lasers, LEDs, or metal-oxide semiconductor field-effect transistors (MOSFETs). Electronic transport, recombination efficiencies, and other properties depend crucially on material parameters such as the band gap as well as build-in potentials or conduction and valence band discontinuities. The carrier confinement strongly affects the emission energies of the device and follows from spatial arrangement of the band edges of the used compounds and their relative energetic alignment. Hence, the engineering of band gaps and offsets is a powerful tool to produce devices that satisfy required specifications. As an example, a clever sequence of semiconducting compounds may cover the complete energy range of the sun's spectra, making extremely efficient solar cells possible [155].

Available methods that allow band gap tuning are not only strain, which can be generated by lattice mismatch, but also material composition. Both approaches are limited concerning epitaxy since continuous layer growth gets difficult once the lattice mismatch becomes too large. For that reason, it is not possible to grow arbitrary material layers on top of each other. Some applications however require the growth of heterostructures on a specific substrate, constraining the selection of alloys to be used in the process. Integrating light-emitting devices on Si based microelectronics for optoelectronic applications is one popular example, since Si is a widely used material in communications. Due to its indirect nature, Si itself is not suitable as the active material for a laser. The lack of a suitable direct gap materials that can be grown lattice matched onto Si prohibited such integrated devices for a long time. Combining existing Si based microelectronics and optoelectronics introduces interesting possibilities for integrated devices with enhanced functionality. Especially data-transfer applications would benefit from this approach. Speed limitations due to transport of electrical pulses could be overcome by replacing them with optical pulses. A realization of an integrated laser on a Si substrate has recently been demonstrated [156, 157].

Thanks to advances in growth techniques, especially in MOVPE, it has become possible to produce a new class of materials: Highly mismatched alloys (HMAs). Ever since, these semiconductor compounds have attracted considerable interest within the research community. Common semiconductors like III-V (e.g. GaAs, gallium phosphide (GaP), or aluminum antimonide (AlSb)) or II-VI (e.g. cadmium sulfide (CdS) or zinc selenide (ZnSe)) alloys are relatively well matched with respect to atom size, electronegativity or ionicity. However, if an atom of such a material is replaced

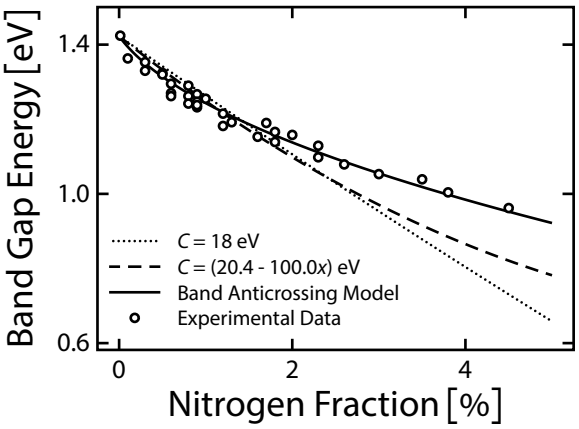

Figure 5.1 — Band gap energy for bulk $Ga(N_xAs_{1-x})$ after Fig. (6) from Ref. [158]. The experimental data (marker) stem from several publications [159–162]. The band anticrossing result (solid) for the band gap using suggested values given in Ref. [158] is compared to a constant bowing (dotted) and a concentration dependend one (dashed) as suggested in Ref. [163].

by one which drastically differs regarding these attributes (hence the name highly mismatched), extraordinary band gap reduction, enhancing of the spin-orbit splitting energy, or other anomalous properties can be observed. These effects occur even for dilute concentrations of the incorporated impurity, thus allowing relatively small lattice mismatch conditions. In turn, this enables the growth of so far impossible band gap combinations in heterostructure systems, exploiting new emission ranges for specific substrate materials. Especially the combination of band gap reduction and split-off energy enhancement may lead to materials in which emission free recombination channels (e.g. Auger-recombination) are greatly suppressed. Used as an active region, such a material could enable lasers with efficiencies exceeding modern day devices.

The usual approach to access material parameters of arbitrary semiconductor compounds by interpolation between the binary end points fails for HMAs. A single bowing parameter describing parabolic interpolation, and even a concentration dependent bowing parameter taking cubic interpolation into account is not sufficient to describe alloy disorder effects of the band gap. Therefore, the band anticrossing (BAC) model was developed and as yet very successfully applied. A comparison of bowing and BAC modeling of the band gap of gallium nitride arsenide (Ga(N,As)) is presented in Fig. 5.1, and will be described in more detail in the following Section.

5.1 Band Anticrossing Model

When nitrogen (N) atoms are integrated into a GaAs host matrix, the N and As atoms compete for the same lattice place since they both stem from the same group of the periodic table. Their different

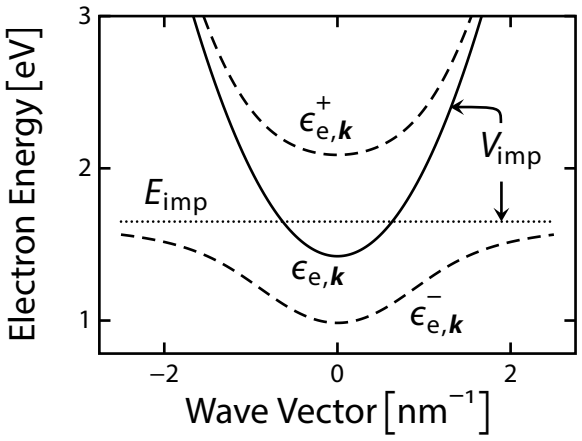

Figure 5.2 — Band anticrossing for bulk $Ga(N_{0.04},As_{0.96})$. The parabolically assumed conduction band (solid) splits into two branches $\epsilon_e^{\pm}$ (dashed). The dispersionless impurity level (dotted) and the interaction strength V_{imp} are shown.

size (N beeing 40 % smaller than As) and ionization energies (As is considerably less electronegative) define the energetic position of the highly localized N defect states. Impurity derived states in $Ga(N_x,As_{1-x})$ are expected to lie energetically either above or close to the lowest conduction band edge [164, 165]. Exchanging only 1 % As by N already decreases the band gap by approximately 180 meV. First attempts to explain this extraordinary shrinkage using a single bowing parameter [166, 167] or a concentration dependent one [168] were proofed insufficient. A comparison of both approaches together with experimental data is shown in Fig. 5.1. They fail over a wider range of N fractions, creating the need for a more sophisticated model.

Remedy was provided by the BAC model, which was developed by Shan et al. [169]. It assumes that the conduction band undergoes a restructuring process due to interactions between the highly localized substitutional N atoms and the extended conduction band edge states. The interaction strength between the dispersionless impurity band E_{imp} and the extended states of the host matrix is determined by the hybridization energy $V_{imp}\sqrt{x}$, where x is the impurity concentration. In a simple two-band model which neglects any interaction to the valence bands, the consequential splitting of the original conduction band into a ϵ^{+} and a ϵ^{-} branch is given by [169]

$$\epsilon^{\pm}_{e,\boldsymbol{k}} = \frac{1}{2}\left[\epsilon_{e,\boldsymbol{k}} + E_{imp} \pm \sqrt{\left[\epsilon_{e,\boldsymbol{k}} - E_{imp}\right]^2 + 4V_{imp}^2\, x}\right]. \tag{5.1}$$

For GaAs at room temperature, the parameters are $\epsilon_{e,\mathbf{0}} = 2.42\,\text{eV}$, $m_e = 0.067\,m_0$, $V_{imp} = 2.7\,\text{eV}$, and $E_{imp} = 1.65\,\text{eV}$ [158, 163]. Figure 5.2 depicts the corresponding two branches of Eq. (5.1) (dashed lines) for $x = 4\%$ N incorporation. The anticrossing between the flat E_{imp} band (dotted line) and the parabolically assumed conduction band (solid line) gives rise to the $\epsilon^{-}_{e,\boldsymbol{k}}$ band that defines the

true band gap.

The composition and strain dependence of the bulk band edge and the impurity level is given by [170, 171]

$$\epsilon_{\mathrm{e},\mathbf{0}}(x) = \epsilon_{\mathrm{e},\mathbf{0}}^{\mathrm{host}} - \alpha\, x + 2a_{\mathrm{c}}^{\mathrm{host}}\, \epsilon_{xx}\left(1 - \frac{c_{12}^{\mathrm{host}}}{c_{11}^{\mathrm{host}}}\right), \tag{5.2}$$

and

$$E_{\mathrm{imp}}(x) = E_{\mathrm{imp}}(x=0) - \gamma\, x + 2a_{\mathrm{c}}^{\mathrm{imp}}\, \epsilon_{xx}\left(1 - \frac{c_{12}^{\mathrm{host}}}{c_{11}^{\mathrm{host}}}\right), \tag{5.3}$$

introducing the virtual crystal shifts α and γ for the conduction and impurity band, respectively. The superscript *host* refers to the suggestion that all material parameters except the band gap should be taken from the host matrix rather than being interpolated between all binary consitutents [158, 172]. The vast difference between the band structure of GaN and other (binar, ternary, or quaternary) compounds is an argument in favor of this suggestion. However, this issue is not finally settled. The hydrostatic deformation potentials of the conduction band are referred to as a_{c}. Biaxial strain contributions are given following the Bir–Pikus formalism, containing the elastic constants c_{ij}^{host} of the host with $\epsilon_{xx} = \frac{a_{\mathrm{s}}-a}{a}$, the strain resulting from mismatch between the lattice constant of the substrate a_{s} and the material a, respectively.

To calculate realistic band structures in the framework of $\boldsymbol{k}\cdot\boldsymbol{p}$ theory, one needs to couple each conduction band to the defect levels via the interaction strength $V_{\mathrm{imp}}\sqrt{x}$. Then, the $\boldsymbol{k}\cdot\boldsymbol{p}$ Hamiltonian can be written as [173]

$$H = \begin{pmatrix} E_{\mathrm{imp}} & V_{\mathrm{imp}}\sqrt{x} & 0 \\ V_{\mathrm{imp}}\sqrt{x} & E_{\mathrm{e}}(\boldsymbol{k}) & \dots \\ 0 & \vdots & \ddots \end{pmatrix}, \tag{5.4}$$

where $E_{\mathrm{e}}(\boldsymbol{k})$ results from the matrix formalism of Eq. (2.10) between conduction band wave functions. Its precise form differs depending on what basis set is used and how many bands are included. An explicit version can be found in Ref. [173].

5.2 Valence Band Offset Determination of Ga(N,As)/GaAs Quantum Wells

As a consequence of its enormous band gap reduction, Ga(N,As) attracts great interest due the corresponding device applications in long-wavelength optoelectronics. Although the band gap

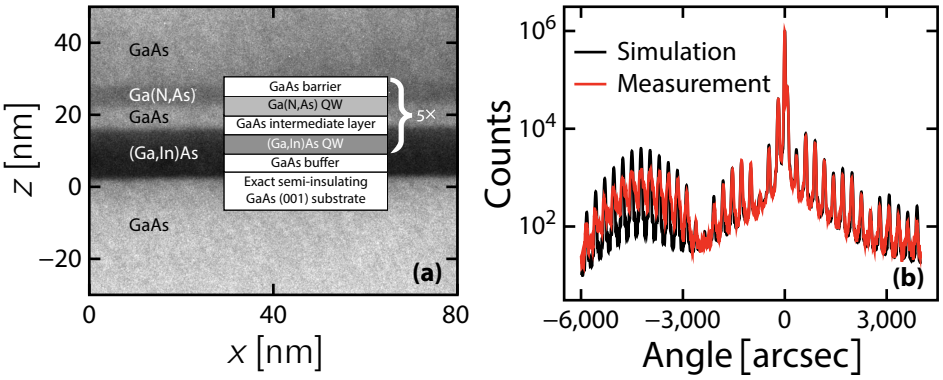

Figure 5.3 — (a) TEM image of sample #25857 along the growth direction z and in-plane coordinate x. The inset shows a schematic of the layer sequence. (b) HR-XRD measurement (red) and simulation (black). The best fit simulation yields layer composition and thicknesses.

reduction of bulk Ga(N,As) has been well explained by the BAC model, the nature of its band alignment in heterostructures remains an open question. Several authors interpreted their data to show a type-I band alignment [174], while others found a type-II discontinuity [175, 176] in Ga(N,As)/GaAs quantum wells. It is also reasonable to argue that the valence band offsets (VBOs) are vanishingly small, since all N related modifications should occur in the conduction band.

To clarify this issue, a sequence of samples was designed to eliminate both the GaAs and Ga(N,As) valence band states in the PL spectrum for low excitation powers. The replacement by a controllable PL valence band end state ultimately allows the determination of the VBO, which is shown in this Chapter.

5.2.1 Sample Series

The samples were grown by MOVPE in a commercially available AIXTRON AIX 200 Gas Foil Rotation (GFR) on exact semi-insulating GaAs (001) (0.1°) substrates at 525 °C. The active region of each sample was repeated five times and consists of adjacent (Ga,In)As, GaAs, and Ga(N,As) layers, thus forming a double QW (DQW) structure. The growth was designed to keep all material parameters constant except the thickness d of the central GaAs layer that serves as a separation between the (Ga,In)As and the Ga(N,As) QWs. Therefore, a gradual decrease of d should reveal the transition from a type-I PL within the (Ga,In)As to a type-II PL across the spacing layer.

Structural characterization has been obtained by high resolution X-ray diffraction (HR-XRD) in (004)-reflection as well as transmission electron microscopy (TEM). With these methods, layer thicknesses and alloy compositions of each layer can be evaluated. The results are shown in Fig. 5.3 while the extracted alloy compositions x_{In}, x_{N}, and layer thicknesses d_{In}, d_{N} of the (Ga,In)As and Ga(N,As) QW, respectively, are summarized in Table 5.1. An illustration of the bulk band edges of

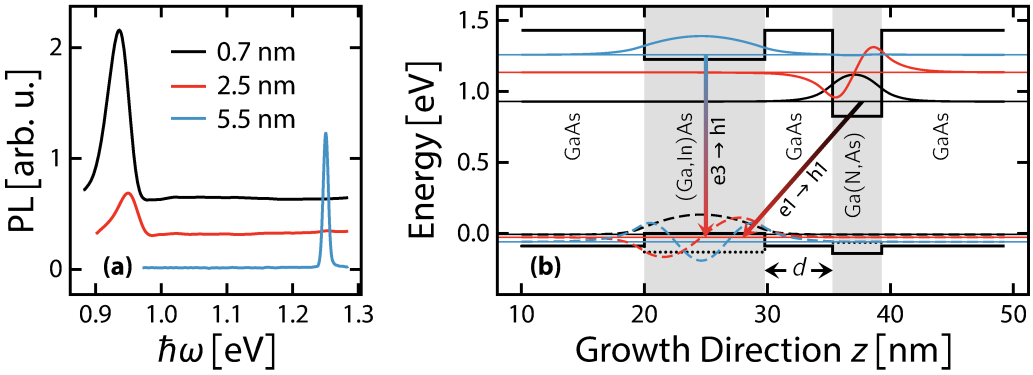

Figure 5.4 — (a) Experimental photoluminescence spectra for an excitation power of 3 W cm^{-2} of all three samples specified in Table 5.1. For better visibility, the spectra are shifted. (b) Schematic overview of sample #25857 with d = 5.5 nm, showing the most important electronic states and transitions. The hh and e band edges are shown as a black solid line while the lh band is shown as a black dotted line.

sample #25857 with d = 5.5 nm is presented in Fig. 5.4(b).

5.2.2 Valence Band Offset

The samples described in the previous Section represent an excellent system to determine the VBO at the Ga(N,As)/GaAs interface. This is due to the fact that it has been shown, that the measured PL is actually that of a type-II junction in such samples, if x_N exceeds 1% [40, 177]. Hence, the initial and final states of PL transitions at low densities will be located in the Ga(N,As) and (Ga,In)As layer, respectively, since all samples contain more than 4% N. Although all necessary material parameters such as effective masses or deformation potentials are well characterized, the band offsets are only known for the (Ga,In)As/GaAs interface. A valid strategy to extract them at the Ga(N,As)/GaAs interface is to treat them as variable and calculate the PL under the premise to reproduce the experimentally observed type-II transition energy.

#	x_{In}	x_N	d_{In}	d_N	d
25857	24.2 %	4.9 %	9.8 nm	4.0 nm	5.5 nm
25859	24.1 %	4.5 %	9.8 nm	4.0 nm	2.5 nm
25858	23.9 %	4.6 %	9.9 nm	4.0 nm	0.7 nm

Table 5.1 — Structural specification of all samples obtained by HR-XRD and TEM. The spacing layer thickness d is the only parameter varied. All other parameters were attempted to be identical. The first column characterizes the samples via a unique identifier.

First, it is beneficial to inspect the experimental PL spectra of all samples which are shown in Fig. 5.4(a). Here, the excitation power P is $3\,\mathrm{W\,cm^{-2}}$. A noticeable difference can be observed between sample #25857 (blue) with thick separation layer $d = 5.5\,\mathrm{nm}$ and the other two. For the former, the PL stems from a transition where both electrons and holes are localized within the (Ga,In)As region. In contrast, the other two samples show a PL signal that can be assigned to a transition across the GaAs spacing layer, where the involved electronic states are in the Ga(N,As) QW. For a more pictorial view, the bulk band edges together with the most relevant confinement wave functions and transitions within sample #25857 are visualized in Fig. 5.4(b), obtained by diagonalizing the $\boldsymbol{k}\cdot\boldsymbol{p}$ Hamiltonian. Here, the transitions e3 → h1 can be connected to the peak visible in the spectrum of sample #25857, while the spatially indirect e1 → h1 transition is linked to the other two spectra.

Proceeding to find the band offsets at the Ga(N,As)/GaAs interface, they are assumed to be unknown and determined by finding values that reproduce the experimentally observed PL peak position from samples #25858 (black) at 0.935 eV and #25859 (red) at 0.951 eV shown in Fig. 5.4(a). Fixing the BAC parameters to the well established values [158] of $\alpha = \gamma = 0\,\mathrm{eV}$, $V_{\mathrm{imp}} = 2.7\,\mathrm{eV}$, and $E_{\mathrm{imp}}(x = 0) = 2.65\,\mathrm{eV}$ results in a bulk band gap energy around 1 eV at 10 K for the Ga(N,As) QW. Tuning the band offset in order to reproduce the experimentally obtained PL peak energy yields a VBO of around 24 meV. This value is referring to the lh band which energetically lies above the hh states in the Ga(N,As) layer due to strain. It is used in all further computations. Although the lh VBO is of type-I, those for the hh is of type-II. However, a variety of BAC parameter sets have been proposed, a selection of which are summarized in Table 5.2 together with the resulting lh VBO which reproduces the experimental PL peak position. It is worth noting that all BAC parameter sets produce a type-I lh band alignment necessary to explain the experimental PL. This constitutes strong evidence that the Ga(N,As)/GaAs interface indeed forms a type-I heterojunction.

Having the VBO determined, Fig. 5.5 presents a comparison between experimental and theoretical PL spectra. While the shaded areas represent the experimental data which are also shown in Fig. 5.4(a), the dashed lines are the theoretically obtained counterparts using a density of $n_0 =$

Reference	α	γ	V_{imp}	$E_{\mathrm{imp}}(x = 0)$	VBO
[176]	−1.55 eV	−3.89 eV	−2.4 eV	1.7 eV	176 meV
[171]	−1.55 eV	0.0 eV	−2.45 eV	1.65 eV	35 meV
[170]	−1.55 eV	−2.52 eV	−1.5 eV	1.675 eV	132 meV
[158]	0.0 eV	0.0 eV	−2.7 eV	1.65 eV	24 meV

Table 5.2 — Valence band offset of the lh band, which is the upmost valence band resulting from different sets of band anticrossing taken from the indicated references.

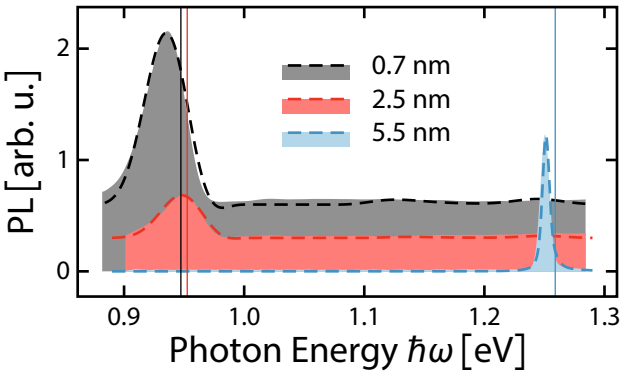

Figure 5.5 — Comparison between experimental (shaded areas) and computed (dashed lines) PL signals for weak excitation conditions. The vertical lines indicate the respective dominant transition energy. The samples were excited at $P = 3\,\mathrm{W\,cm^{-2}}$, while a density of $10^9\,\mathrm{cm^{-2}}$ was assumed for the theoretical spectra.

$10^9\,\mathrm{cm^{-2}}$. The inhomogeneous broadening was chosen to be 7 meV for sample #25857 ($d = 5.5\,\mathrm{nm}$), while for the other two it is 35 meV, producing an extraordinary degree of agreement. The vast difference for the inhomogeneous broadening can be explained by the nature of the dominant transition. For sample #25857, the dominant PL transition at 1.251 eV is of type-I and exclusively involves electron states in the (Ga,In)As layer. Regarding the other two samples with significantly less space between the QW layers, electrons are confined to the Ga(N,As) QW and define the transition around 0.94 eV. It is well known that incorporating even a dilute concentration of N into a semiconductor host matrix induces a large amount of disorder [178–181]. This leads to deviations in the band gap so that carriers are exposed to a variety of potential fluctuations. These circumstances are reflected in a broad PL signal, where FWHM of 35 – 40 meV are not unusual.

5.2.3 Dominant Transitions

To further characterize this system, the optical response of the DQW structures are studied under different excitation conditions. Therefore, the PL spectra of one specific sample are examined as a function of excitation power P.

For sample #25859 with $d = 2.5\,\mathrm{nm}$, Fig. 5.6 presents the PL signals (shaded areas) for various excitation powers. For increasing power, the PL peak signal shifts to higher energies while it simultaneously broadens as a consequence of Pauli blocking effects. However, for $P > 84\,\mathrm{W\,cm^{-2}}$, the line shape broadens asymmetrically and unusually strong. Further increasing the pump power above $3\,\mathrm{kW\,cm^{-2}}$ even evokes a narrowing of the spectrum.

To identify the underlying physics behind this effect, PL spectra for several carrier sheet densities n are calculated for this particular sample. Figure 5.7 presents the hh and lh confinement potentials

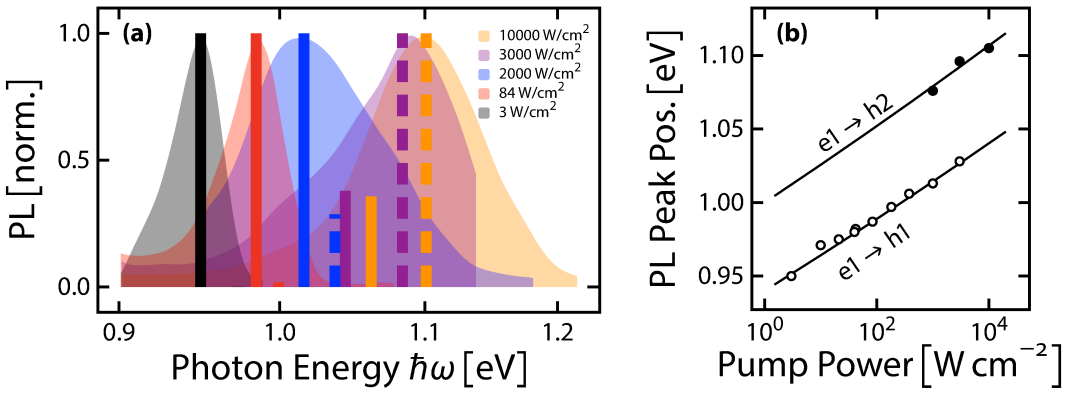

Figure 5.6 — (a) Pump power dependent PL signals (shaded areas). The theoretical predicted PL intensities from the e1 → h1 (solid) and e1 → h2 (dashed) transitions are indicated by vertical bars. (b) Respective transition energies extracted from the experiment by a bi-Gaussian fitting. The solid line is a fit and acts as a guide to the eye.

V_{hh} and V_{lh} for various densities after solving the Poisson equation self-consistently in Frames (a) and (b), respectively. Due to local charge inhomogeneities, the band structure gradually loses its step-like appearance with increasing density. Both V_{hh} and V_{lh} significantly change in the center Ga(N,As)/GaAs region. Especially the lh states in the Ga(N,As) layer energetically rise until they almost reach the same height as the hh band in the (Ga,In)As QW.

This in turn affects the confinement functions. Especially the second (h2) and third (h3) hole wave functions become modified while all other relevant wave functions are more or less unaffected. Therefore, Fig. 5.7(c) and (d) present the dominant part of the band edge wave function corresponding to the h2 and h3 states, respectively. For weak excitation, the holes are confined within the (Ga,In)As QW. With increasing density, the h3 state shifts into the Ga(N,As) QW region as a consequence of the energetically favorable lh potential. Further increasing the density exchanges the h2 and h3 states above a certain critical density $n_{\mathrm{cr}} = 1.25 \times 10^{12}\,\mathrm{cm}^{-2} = 1250\,n_0$. For very high densities, the carriers in the h3 state get redistributed into the GaAs barrier.

The total charge density distribution substantiates this trend. It is shown for electrons and holes in Fig. 5.8(a) and (b), respectively, and according to Eq. (2.20). While electrons only redistribute within the Ga(N,As) QW, the charge density of holes for a relatively weak excitation enhances near the (Ga,In)As/GaAs interface. For strong excitations, the hole charge density begins to accumulate in the Ga(N,As) QW and even in the separation layer. Additionally, the h2 state, which is the origin of charges within the Ga(N,As) QW region, will be increasingly occupied with elevating density. Therefore, Fig. 5.8(c) presents the occupation ratio $n_{\mathrm{h1}}/n_{\mathrm{h2}}$ the states h1 and h2, which are relevant for the PL, as a function of total density n. Significant amount of carriers populate the h2 state only above $n = 10^{12}\,\mathrm{cm}^{-2}$.

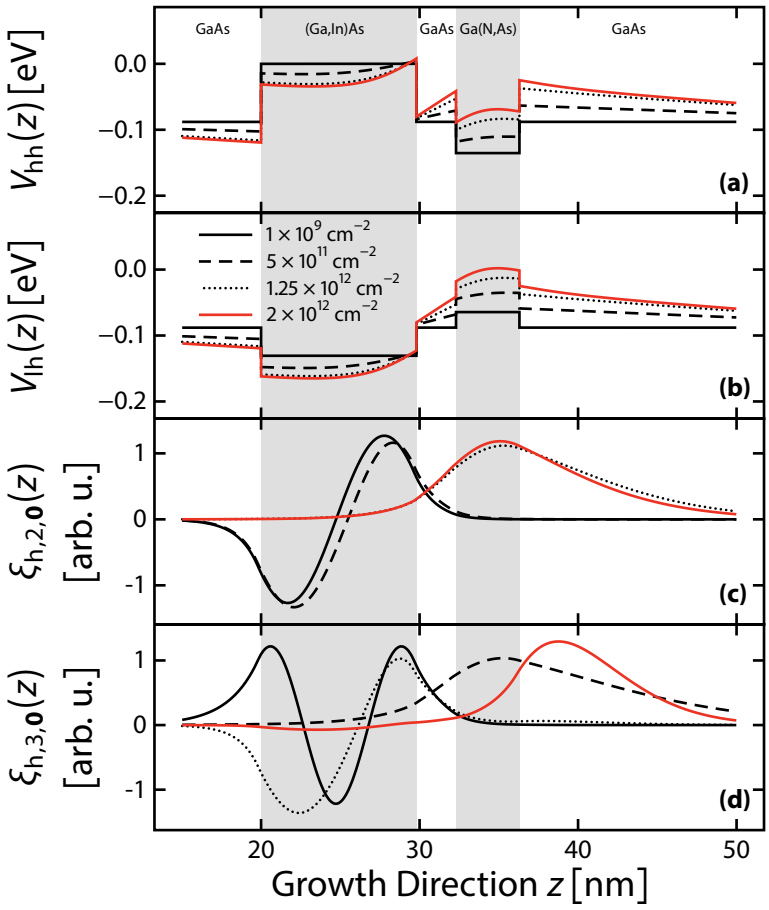

Figure 5.7 — Band edges and wave functions as a function of density. Confinement potential of the (a) hh and (b) lh band. The single-particle wave functions in the (c) h2 and (d) h3 state.

This has direct consequences for the optical transitions, since they are mainly dominated by the dipole-matrix elements, which are determined by the spatial overlap of the wave functions of the participating states. Transitions involving the e1 and h1 states have an inefficient overlap since their wave functions remain in the Ga(N,As) and (Ga,In)As layers, respectively. However, since the h2 wave function is located in the Ga(N,As) QW for $n > n_{cr}$ just like the electrons are, the corresponding dipole-matrix element is much stronger. In total, the PL spectrum consists of the two transitions e1 → h1 and e1 → h2, which compete against each other. This competition is decided in favor of the e1 → h2 transition above the threshold density due to an interplay of an increasing occupation of the h2 state and a larger dipole-matrix element. But at low densities, e1 → h1 dominates the spectrum.

For better visualization, theoretically obtained PL strengths are presented along the experimental data in Fig. 5.6. While the shaded areas show the experimental data, the vertical lines indicate

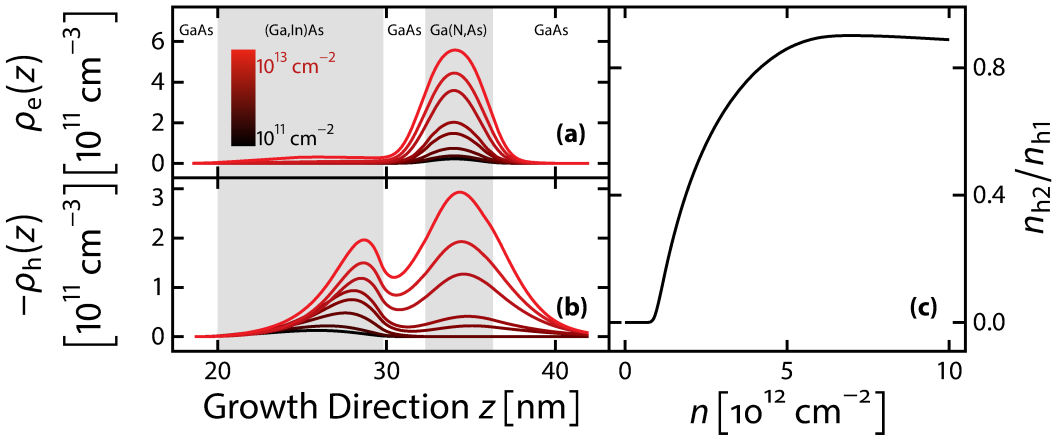

Figure 5.8 — Absolute charge distribution for (a) electrons and (b) holes inside the DQW structure. (c) Occupation ratio between the states h1 and h2.

the computed PL contributions according to the e1 → h1 (solid) and the e1 → h2 (dashed) transition. As discussed, the interplay between these two transitions is the origin of the unusually broad PL line shape.

In this Section, it was demonstrated that once the band gap for Ga(N,As) is fixed by choosing a BAC parameter set, the band offsets of the Ga(N,As)/GaAs heterojunction can be determined by tuning the type-II PL transition to available experimental data. This is possible due to the unique sample design where a GaAs spacing layer separates a (Ga,In)As and a Ga(N,As) QW, so that the PL end state is well characterized. A density dependent PL study reveals that the h2 carriers relocalize from their initial position within the (Ga,In)As QW into the Ga(N,As) QW region. This redistribution of charges leads to an increased dipole-matrix element due to an increased spatial overlap of the participating wave functions. With an additionally increasing occupation of the h2 state, the related PL signal dominates the overall spectrum which is otherwise defined by the e1 → h1 transition at lower densities.

6 Conclusion and Outlook

Until today, the microscopic many-body description of exciton properties has been applied to direct semiconductors with isotropic effective electron–hole masses. In this thesis, I have extended the theory to also include materials exhibiting mass anisotropy. For this purpose, the Wannier equation, which constitutes an eigenvalue problem for the exciton wave functions and their binding energies, was generalized to systems where the band structure can be described within the effective–mass approximation, and all three principle directions have individual effective electron and hole masses. An efficient numerical scheme based on an expansion of the exciton wave functions in terms of spherical harmonics was developed to obtain the radial solutions of the Wannier equation. As a consequence, radial parts with different quantum numbers are coupled, which is contrary to the case with isotropic masses where only identical quantum numbers couple. Implied modifications to the shape of the exciton wave functions have been studied on the example of Ge, where a squeezing in the direction of the heavier mass is observed. Consequently, the $2s$ and $2p$ states become energetically non-degenerate.

Since THz spectroscopy is a tool specially suited to investigate exciton properties, their wave functions were used to calculate the THz absorption spectrum of Ge and Si. Both materials exhibit strong mass anisotropy. Indirect semiconductors in general have multiple energy minimums. Investigating a specific one reveals that the selection rules are modified dependent on the applied THz field polarization. If the field is polarized parallel to the momentum path that points from the Brillouin-zone center to the energy minimum, transitions are allowed that involve equal m components while the l components differ by ± 1. When the THz field is polarized in the plane perpendicular to this path, both m and l are changed by ± 1 to result in a non-vanishing transition-matrix element.

As a consequence, two distinct exciton resonances can be observed in the THz absorption spectrum. Due to the degeneracy of the indirect energy minimum, these resonances are detected simultaneously and cannot be addressed separately via the THz field polarization. Nevertheless, they should be measurable in good-quality THz-absorption experiments.

These experiments have not yet been conducted for Ge. However, similar measurements have been performed using Si and indeed show a double-resonance structure. The authors of the corresponding study attribute this feature to the exciton's fine structure. To conclusively confirm that this is rather a consequence of mass anisotropy, additional experiments should be conducted. A splitting due to the fine splitting of excitons can be excluded via magneto-photoluminescence spectroscopy or circularly polarized excitation fields.

The exciton wave functions of semiconductors exhibiting mass anisotropy has also been applied to calculate the optical absorption of rutile TiO_2 near its fundamental direct band gap. In this regard, the Elliott formula for optical absorption was used in which optical-matrix elements were obtained by DFT calculations. It was possible to assign experimentally available excitonic signatures by including quadrupole interactions, revealing that its origin is the 1*s* exciton.

I also analyzed pump–probe absorption experiments of Ge and (Ga,In)As QWs, which are inspired by a Mollow-type setup, e.g. a resonantly pumped two-level system. The samples were excited resonantly to the 1*s*-hh1 transition by strong optical pulses. While the Ge sample exhibits unusually strong nonlinear transients in the form of two side bands around the 1*s* resonance, the (Ga,In)As heterostructure only features expected EID effects such as a broadening. A thorough investigation of the dephasing mechanisms in these samples show that a phonon-assisted scattering produces the observed side bands in Ge while carrier–carrier scattering prevent their formation. From the analysis of the pure two-level system it becomes clear that an averaging of the envelope-function phase is necessary to reproduce Mollow's famous triplet structure appearing in absorption measurements. Confirming such a phase dependency experimentally poses an extremely challenging task. However, if under control, the absorption of a two-level system like a single QD can then be used to determine the carrier-envelope phase in phase-stable laser systems. Thus, more research effort is worth considering.

Finally, I investigated the experimental PL spectra of a semiconductor heterostructure using a fully microscopic many-body theory. The sample was designed to show a type-II PL at low densities where electrons are confined in a Ga(N,As) QW while holes are located in a (Ga,In)As QW. Realistic band structures are obtained using a 10-band $\boldsymbol{k}\cdot\boldsymbol{p}$ model including a BAC model. A weak type-I valence band alignment for lh states at the Ga(N,As)/GaAs interface could be confirmed. The unusually broad PL spectra observed/GaAs while increasing the excitation power in the experiment were explained by the relocalization of carriers.

Bibliography

[1] K. Leo, M. Wegener, J. Shah, D. Chemla, E. Göbel, T. Damen, S. Schmitt-Rink, and W. Schäfer, Phys. Rev. Lett. **65**, 1340–1343 (1990).

[2] Y. Z. Hu, R. Binder, S. W. Koch, S. T. Cundiff, H. Wang, and D. G. Steel, Phys. Rev. B **49**, 14382–14386 (1994).

[3] L. Bányai, D. B. T. Thoai, E. Reitsamer, H. Haug, D. Steinbach, M. U. Wehner, M. Wegener, T. Marschner, and W. Stolz, Phys. Rev. Lett. **75**, 2188–2191 (1995).

[4] A. Mysyrowicz, D. Hulin, A. Antonetti, A. Migus, W. T. Masselink, and H. Morkoç, Phys. Rev. Lett. **56**, 2748–2751 (1986).

[5] C. Sieh, T. Meier, F. Jahnke, A. Knorr, S. W. Koch, P. Brick, M. Hübner, C. Ell, J. Prineas, G. Khitrova, and H. M. Gibbs, Phys. Rev. Lett. **82**, 3112–3115 (1999).

[6] S. Leinß, T. Kampfrath, K. Volkmann, M. Wolf, J. T. Steiner, M. Kira, S. W. Koch, A. Leitenstorfer, and R. Huber, Phys. Rev. Lett. **101**, 1–4 (2008).

[7] O. Vänskä, I. Tittonen, S. W. Koch, and M. Kira, Phys. Rev. Lett. **114**, 116802 (2015).

[8] H. Haug, and S. W. Koch, *Quantum Theory of the Optical and Electronic Properties of Semiconductors*, 5. (World Scientific Publishing Co., 2009).

[9] M. Kira, W. Hoyer, and S. W. Koch, Phys. Status Solidi B **238**, 443–450 (2003).

[10] M. Kira, and S. W. Koch, Prog. Quantum Electron. **30**, 155–296 (2006).

[11] J. T. Steiner, "Microscopic Theory of Linear and Nonlinear Terahertz Spectroscopy of Semiconductors", Dissertation (Philipps-Universität Marburg, 2008).

[12] M. Kira, and S. W. Koch, *Semiconductor Quantum Optics*, 1. (Cambridge University Press, Cambridge/New York, 2012).

[13] H. Weyl, *Raum, Zeit, Materie*, Vol. 7 (Springer-Verlag, 1918).

[14] H. Weyl, Z. Phys. **46**, 1–46 (1927).

[15] W. P. Schleich, "Atom-Field Interaction", in *Quantum opt. phase sp.* (2004), pp. 381–412.

[16] L. D. Landau, and E. M. Lifshitz, *Electrodynamics of Continuous Media*, 1st ed., Vol. 8, Course of Theoretical Physics (Pergamon Press, 1960).

[17] L. I. Schiff, *Quantum Mechanics*, edited by L. I. Schiff, 3rd ed. (McGraw-Hill, 1968).

[18] E. O. Kane, "The $\boldsymbol{k} \cdot \boldsymbol{p}$ Method", in *Semicond. semimetals*, Vol. 1 (1966), pp. 75–100.

[19] L. C. Lew Yan Voon, and M. Willatzen, *The $\boldsymbol{k} \cdot \boldsymbol{p}$ Method: Electronic Properties of Semiconductors* (2009).

[20] P. Yu, and M. Cardona, *Fundamentals of Semiconductors: Physics and Materials Properties*, 4. (Springer Science & Business Media, 2010).

[21] G. F. Koster, and J. C. Slater, Phys. Rev. **95**, 1167 (1954).

[22] C. M. Goringe, D. R. Bowler, and E. Hernández, Reports Prog. Phys. **60**, 1447–1512 (1997).

[23] P. Hohenberg, and W. Kohn, Phys. Rev. **136**, B864–B871 (1964).

[24] K. Capelle, eprint arXiv:cond-mat/0211443 (2002).

[25] J. Hader, N. Linder, and G. H. Döhler, Phys. Rev. B **55**, 6960–6974 (1997).

[26] F. Bloch, Z. Phys. **52**, 555–600 (1929).

[27] G. Bastard, *Wave mechanics applied to semiconductor heterostructures*, 1., Monographies de physique (Les Éditions de Physique, 1988).

[28] H. Wang, K. Ferrio, D. G. Steel, Y. Hu, R. Binder, and S. W. Koch, Phys. Rev. Lett. **71**, 1261–1264 (1993).

[29] W. W. Chow, and S. W. Koch, *Semiconductor-Laser Fundamentals*, 1. (Springer-Verlag, Berlin/Heidelberg, 1999).

[30] U. Rössler, and D. Strauch, *Group IV Elements, IV-IV and III-V Compounds. Part α - Lattice Properties*, edited by O. Madelung, U. Rössler, and M. Schulz, Landolt-Börnstein - Group III Condensed Matter (Springer-Verlag, Berlin/Heidelberg, 2001).

[31] P.-O. Löwdin, J. Chem. Phys. **19**, 1396 (1951).

[32] S. Richard, F. Aniel, and G. Fishman, Phys. Rev. B **70**, 235204 (2004).

[33] G. Bastard, and J. Brum, IEEE J. Quantum Electron. **22**, 1625–1644 (1986).

[34] D. Ahn, and S. L. Chuang, J. Appl. Phys. **64**, 6143 (1988).

[35] I.-H. Tan, G. L. Snider, L. D. Chang, and E. L. Hu, J. Appl. Phys. **68**, 4071 (1990).

[36] G. Liu, and S. L. Chuang, Phys. Rev. B **65**, 165220 (2002).

[37] N. N. Ledentsov, J. Böhrer, M. Beer, F. Heinrichsdorff, M. Grundmann, D. Bimberg, S. V. Ivanov, B. Y. Meltser, S. V. Shaposhnikov, I. N. Yassievich, N. N. Faleev, P. S. Kop'ev, and Z. I. Alferov, Phys. Rev. B **52**, 14058–14066 (1995).

[38] Y. S. Chiu, M. H. Ya, W. S. Su, and Y. F. Chen, J. Appl. Phys. **92**, 5810 (2002).

[39] A. H. Khalid, and K. Kontis, Meas. Sci. Technol. **20**, 025305 (2009).

[40] C. Schlichenmaier, "Modeling of Optical Properties of Semiconductor Heterostructures", Dissertation (Philipps-Universität Marburg, 2005).

[41] W. Hoyer, "Quantentheorie zu Exzitonbildung und Photolumineszenz in Halbleitern", Dissertation (Philipps-Universität Marburg, 2002).

[42] F. Jahnke, M. Kira, and S. W. Koch, *Linear and nonlinear optical properties of excitons in semiconductor quantum wells and microcavities*, Feb. 1997.

[43] J. Hader, S. W. Koch, and J. V. Moloney, Solid. State. Electron. **47**, 513–521 (2003).

[44] A. K. Rajagopal, Phys. Rev. B **15**, 4264–4269 (1977).

[45] T. Stroucken, A. Knorr, P. Thomas, and S. W. Koch, Phys. Rev. B **53**, 2026–2033 (1996).

[46] E. Hecht, *Optik*, 5. (Oldenbourg Wissenschaftsverlag, 2009).

[47] I. Vurgaftman, W. W. Bewley, C. L. Canedy, C. S. Kim, J. R. Lindle, M. Kim, and J. R. Meyer, "Antimonide Type-II "W" Lasers", in *Mid-infrared semicond. optoelectron.* Edited by A. Krier, (2006), pp. 189–217.

[48] C. Berger, C. Möller, P. Hens, C. Fuchs, W. Stolz, S. W. Koch, A. Ruiz Perez, J. Hader, and J. V. Moloney, AIP Adv. **5**, 047105 (2015).

[49] S. Gies, C. Kruska, C. Berger, P. Hens, C. Fuchs, A. Ruiz Perez, N. W. Rosemann, J. Veletas, S. Chatterjee, W. Stolz, S. W. Koch, J. Hader, J. V. Moloney, and W. Heimbrodt, Appl. Phys. Lett. **107**, 13–16 (2015).

[50] C. Möller, C. Fuchs, C. Berger, A. Ruiz Perez, M. Koch, J. Hader, J. V. Moloney, S. W. Koch, and W. Stolz, Appl. Phys. Lett. **108**, 071102 (2016).

[51] S. Schmitt-Rink, D. S. Chemla, and D. A. B. Miller, Adv. Phys. **38**, 89–188 (1989).

[52] M. Schäfer, M. Werchner, W. Hoyer, M. Kira, and S. W. Koch, Phys. Rev. B **74**, 1–11 (2006).

[53] W. Hoyer, M. Kira, and S. W. Koch, (2006), arXiv:0604349 [cond-mat].

[54] M. L. Coffman, Am. J. Phys. **33**, 820 (1965).

[55] M. Dvorak, S. H. Wei, and Z. Wu, Phys. Rev. Lett. **110**, 1–5 (2013).

[56] P. U. Jepsen, D. G. Cooke, and M. Koch, Laser Photonics Rev. **5**, 124–166 (2011).

[57] M. Kira, W. Hoyer, T. Stroucken, and S. W. Koch, Phys. Rev. Lett. **87**, 176401 (2001).

[58] D. Golde, "Microscopic Investigations of the Terahertz and the Extreme Nonlinear Optical Response of Semiconductors", Dissertation (Philipps-Universität Marburg, 2010).

[59] A. E. Almand-Hunter, H. Li, S. T. Cundiff, M. Mootz, M. Kira, and S. W. Koch, Nature **506**, 471–5 (2014).

[60] M. Mootz, M. Kira, and S. W. Koch, New J. Phys. **15** (2013) 10.1088/1367-2630/15/9/093040.

[61] W. Y. Liang, Phys. Educ. **5**, 226–228 (1970).

[62] S. B. Nam, D. C. Reynolds, C. W. Litton, R. J. Almassy, T. C. Collins, and C. M. Wolfe, Phys. Rev. B **13**, 761–767 (1976).

[63] R. C. Miller, D. A. Kleinman, W. T. Tsang, and A. C. Gossard, Phys. Rev. B **24**, 1134–1136 (1981).

[64] H. Tong, and M. W. Wu, Phys. Rev. B **83**, 61–67 (2011), arXiv:1103.0467.

[65] S. Chatterjee, C. Ell, S. Mosor, G. Khitrova, H. M. Gibbs, W. Hoyer, M. Kira, S. W. Koch, J. P. Prineas, and H. Stolz, Phys. Rev. Lett. **92**, 067402 (2004), arXiv:0309160 [cond-mat].

[66] L. Brus, J. Phys. Chem. **90**, 2555–2560 (1986).

[67] N. Nagai, R. Kumazawa, and R. Fukasawa, Chem. Phys. Lett. **413**, 495–500 (2005).

[68] O. Schubert, M. Hohenleutner, F. Langer, B. Urbanek, C. Lange, U. Huttner, D. Golde, T. Meier, M. Kira, S. W. Koch, and R. Huber, Nat. Photonics **8**, 119–123 (2014).

[69] M. C. Beard, G. M. Turner, and C. A. Schmuttenmaer, Phys. Rev. B **62**, 15764–15777 (2000).

[70] R. H. M. Groeneveld, and D. Grischkowsky, J. Opt. Soc. Am. B **11**, 2502 (1994).

[71] J. Černe, J. Kono, M. S. Sherwin, M. Sundaram, A. C. Gossard, and G. E. W. Bauer, Phys. Rev. Lett. **77**, 1131–1134 (1996).

[72] R. A. Kaindl, M. A. Carnahan, D. Hägele, R. Lövenich, and D. S. Chemla, Nature **423**, 734–738 (2003).

[73] C. Y.-P. Chao, and S. L. Chuang, Phys. Rev. B **43**, 7027–7039 (1991).

[74] H. Mathieu, P. Lefebvre, and P. Christol, Phys. Rev. B **46**, 4092–4101 (1992).

[75] P. Chen, C. Piermarocchi, and L. J. Sham, Phys. Rev. Lett. **87**, 067401 (2001), arXiv:0102482 [cond-mat].

[76] C. Piermarocchi, P. Chen, Y. S. Dale, and L. J. Sham, Phys. Rev. B **65**, 075307 (2002).

[77] K.-H. Pantke, V. G. Lyssenko, B. S. Razbirin, H. Schwab, J. Erland, and J. M. Hvam, Phys. Status Solidi B **173**, 69–76 (1992).

[78] G. Bacher, C. Hartmann, H. Schweizer, T. Held, G. Mahler, and H. Nickel, Phys. Rev. B **47**, 9545–9555 (1993).

[79] A. Vinattieri, J. Shah, T. C. Damen, D. S. Kim, L. N. Pfeiffer, M. Z. Maialle, and L. J. Sham, Phys. Rev. B **50**, 10868–10879 (1994).

[80] G. Finkelstein, V. Umansky, I. Bar-Joseph, V. Ciulin, S. Haacke, J.-D. Ganière, and B. Deveaud, Phys. Rev. B **58**, 12637–12640 (1998).

[81] S. Zwerdling, B. Lax, L. M. Roth, and K. J. Button, Phys. Rev. **114**, 80–89 (1959).

[82] L. Laude, F. Pollak, and M. Cardona, Phys. Rev. B **3**, 2623–2636 (1971).

[83] T. Suzuki, and R. Shimano, Phys. Rev. Lett. **103**, 057401 (2009).

[84] T. Suzuki, and R. Shimano, Phys. Rev. Lett. **109**, 046402 (2012).

[85] F. Schwabl, *Quantenmechanik für Fortgeschrittene (QM II)*, 5., Springer-Lehrbuch (Springer-Verlag, Berlin/Heidelberg, 2008).

[86] E. U. Condon, and G. H. Shortley, *The Theory of Atomic Spectra*, 1. (Cambridge University Press, 1935).

[87] A. Messiah, *Quantum Mechanics*, 2nd ed. (Courier Corporation, 2014).

[88] A. Bezubik, A. Dbrowska, and A. Strasburger, J. Non-linear Math. Phys. **11**, 167 (2004).

[89] R. Mehrem, Appl. Math. Comput. **217**, 5360–5365 (2011), arXiv:0909 . 0494.

[90] M. Abramowitz, and I. A. Stegun, *Handbook of Mathematical Functions With Formulas, Graphs and Mathematical Tables*, 10th ed., Applied Mathematics Series (Dover Publications Inc., 1972).

[91] T. C. Damen, J. Shah, D. Y. Oberli, D. S. Chemla, J. E. Cunningham, and J. M. Kuo, Phys. Rev. B **42**, 7434–7438 (1990).

[92] M. Nathan, Phys. Rev. **130**, 2201–2204 (1963).

[93] O. Madelung, *Semiconductors: Group IV Elements and III-V Compounds*, Data in Science and Technology (Springer-Verlag, Berlin/Heidelberg, 1991).

[94] X. Q. Zhou, H. M. van Driel, and G. Mak, Phys. Rev. B **50**, 5226–5230 (1994).

[95] S. Adachi, *Properties of Group-IV, III-V and II-VI Semiconductors* (2005).

[96] C. Lange, N. S. Köster, S. Chatterjee, H. Sigg, D. Chrastina, G. Isella, H. von Känel, M. Schäfer, M. Kira, and S. W. Koch, Phys. Rev. B **79**, 201306 (2009).

[97] C. Lange, N. S. Köster, S. Chatterjee, H. Sigg, D. Chrastina, G. Isella, H. von Känel, B. Kunert, and W. Stolz, Phys. Rev. B **81**, 045320 (2010).

[98] M. Mootz, M. Kira, and S. W. Koch, J. Opt. Soc. Am. B **29**, A17 (2012).

[99] J. R. Haynes, and W. Shockley, Phys. Rev. **81**, 835–843 (1951).

[100] J. R. Haynes, Phys. Rev. **98**, 1866–1868 (1955).

[101] W. P. Dumke, Phys. Rev. **105**, 139–144 (1957).

[102] R. J. Elliott, Phys. Rev. **108**, 1384–1389 (1957).

[103] G. Dresselhaus, J. Phys. Chem. Solids **1**, 14–22 (1956).

[104] T. P. McLean, and R. Loudon, J. Phys. Chem. Solids **13**, 1–9 (1960).

[105] A. Baldereschi, and N. O. Lipari, Phys. Rev. B **3**, 439–451 (1971).

[106] N. O. Lipari, and M. Altarelli, Solid State Commun. **18**, 951–954 (1976).

[107] N. O. Lipari, and M. Altarelli, Phys. Rev. B **15**, 4883–4897 (1977).

[108] T. Nishino, M. Takeda, and Y. Hamakawa, Solid State Commun. **12**, 1137–1140 (1973).

[109] A. Frova, G. Thomas, R. Miller, and E. O. Kane, Phys. Rev. Lett. **34**, 1572–1575 (1975).

[110] M. Hohenleutner, F. Langer, O. Schubert, M. Knorr, U. Huttner, S. W. Koch, M. Kira, and R. Huber, Nature **523**, 572–575 (2015).

[111] M. E. Levinshtein, S. L. Rumyantsev, and M. S. Shur, eds., *Properties of Advanced Semiconductor Materials: GaN, AIN, InN, BN, SiC, SiGe*, A Wiley-Interscience Publication (Wiley, 2001).

[112] E. L. Ivchenko, in Proc. spie, Vol. 2362, edited by J. Singh, (Feb. 1995), pp. 580–591.

[113] M. Bayer, G. Ortner, O. Stern, A. Kuther, A. A. Gorbunov, A. Forchel, P. Hawrylak, S. Fafard, K. Hinzer, T. L. Reinecke, S. N. Walck, J. P. Reithmaier, F. Klopf, and F. Schäfer, Phys. Rev. B **65**, 195315 (2002).

[114] J. Puls, M. Rabe, H.-J. Wünsche, and F. Henneberger, Phys. Rev. B **60**, R16303–R16306 (1999).

[115] C. Fiolhais, F. Nogueira, and M. A. L. Marques, eds., *A Primer in Density Functional Theory*, 1st ed., Lecture Notes in Physics (Springer Berlin Heidelberg, 2003).

[116] J. A. Pople, Rev. Mod. Phys. **71**, 1267–1274 (1999).

[117] W. Kohn, Rev. Mod. Phys. **71**, 1253–1266 (1999).

[118] J. P. Perdew, K. Burke, and M. Ernzerhof, Phys. Rev. Lett. **77**, 3865–3868 (1996).

[119] J. P. Perdew, K. Burke, and M. Ernzerhof, Phys. Rev. Lett. **78**, 1396–1396 (1997).

[120] Y.-S. Kim, M. Marsman, G. Kresse, F. Tran, and P. Blaha, Phys. Rev. B **82**, 205212 (2010).

[121] S. Kück, and H. Werheit, *Non-Tetrahedrally Bonded Binary Compounds II: Supplement to Vol. III/17g*, edited by O. Madelung, 1st ed., Landolt-Börnstein - Group III Condensed Matter (Springer-Verlag Berlin Heidelberg, 2000).

[122] J. M. Soler, E. Artacho, J. D. Gale, A. García, J. Junquera, P. Ordejón, and D. Sánchez-Portal, J. Phys. Condens. Matter **14**, 2745 (2002).

[123] Z. H. Levine, and D. C. Allan, Phys. Rev. Lett. **63**, 1719–1722 (1989).

[124] X. Gonze, and C. Lee, Phys. Rev. B **55**, 10355–10367 (1997).

[125] D. O. Scanlon, C. W. Dunnill, J. Buckeridge, S. A. Shevlin, A. J. Logsdail, S. M. Woodley, C. R. A. Catlow, M. J. Powell, R. G. Palgrave, I. P. Parkin, G. W. Watson, T. W. Keal, P. Sherwood, A. Walsh, and A. A. Sokol, Nat. Mater. **12**, 798–801 (2013).

[126] J. Pascual, J. Camassel, and H. Mathieu, Phys. Rev. Lett. **39**, 1490–1493 (1977).

[127] J. Pascual, J. Camassel, and H. Mathieu, Phys. Rev. B **18**, 5606–5614 (1978).

[128] A. Amtout, and R. Leonelli, Phys. Rev. B **51**, 6842–6851 (1995).

[129] A. Amtout, and R. Leonelli, Solid State Commun. **84**, 349–352 (1992).

[130] F. Bechstedt, *Many-Body Approach to Electronic Excitations: Concepts and Applications*, Springer Series in Solid-State Sciences (Springer Berlin Heidelberg, 2014).

[131] J. Shah, *Ultrafast Spectroscopy of Semiconductors and Semiconductor Nanostructures*, 2. (Springer-Verlag, 1999).

[132] J. Ye, and S. T. Cundiff, eds., *Femtosecond Optical Frequency Comb: Principle, Operation, and Applications*, 1st ed. (Kluwer Academic Publishers, Boston, 2005).

[133] M. C. Gupta, and J. Ballato, eds., *The Handbook of Photonics*, 2nd ed. (CRC Press, 2006).

[134] B. Rössner, D. Chrastina, G. Isella, and H. von Känel, Appl. Phys. Lett. **84**, 3058 (2004).

[135] T. F. Kuech, Mater. Sci. Reports **2**, 1–49 (1987).

[136] M. Joffre, D. Hulin, A. Migus, A. Antonetti, C. Benoit a la Guillaume, N. Peyghambarian, M. Lindberg, and S. W. Koch, Opt. Lett. **13**, 276 (1988).

[137] S. W. Koch, N. Peyghambarian, and M. Lindberg, J. Phys. C **21**, 5229–5249 (1988).

[138] B. R. Mollow, Phys. Rev. **188**, 1969–1975 (1969).

[139] B. R. Mollow, Phys. Rev. A **5**, 1522–1527 (1972).

[140] B. R. Mollow, Phys. Rev. A **5**, 2217–2222 (1972).

[141] F. Wu, S. Ezekiel, M. Ducloy, and B. R. Mollow, Phys. Rev. Lett. **38**, 1077–1080 (1977).

[142] P. Tamarat, B. Lounis, J. Bernard, M. Orrit, S. Kummer, R. Kettner, S. Mais, and T. Basché, Phys. Rev. Lett. **75**, 1514–1517 (1995).

[143] D. Fröhlich, A. Nöthe, and K. Reimann, Phys. Rev. Lett. **55**, 1335–1337 (1985).

[144] J. E. Sipe, Personal communication, 2013.

[145] A. Lipsich, S. Barreiro, A. M. Akulshin, and A. Lezama, Phys. Rev. A **61**, 053803 (2000).

[146] E. del Valle, and F. P. Laussy, Phys. Rev. Lett. **105**, 233601 (2010).

[147] X. Xu, B. Sun, P. R. Berman, D. G. Steel, A. S. Bracker, D. Gammon, and L. J. Sham, Science **317**, 929–32 (2007).

[148] A. Ulhaq, S. Weiler, S. M. Ulrich, R. Roßbach, M. Jetter, and P. Michler, Nat. Photonics **6**, 238–242 (2012).

[149] R. W. P. Drever, J. L. Hall, F. V. Kowalski, J. Hough, G. M. Ford, A. J. Munley, and H. Ward, Appl. Phys. B Photophysics Laser Chem. **31**, 97–105 (1983).

[150] B. Ewers, N. S. Köster, R. Woscholski, M. Koch, S. Chatterjee, G. Khitrova, H. M. Gibbs, A. C. Klettke, M. Kira, and S. W. Koch, Phys. Rev. B **85**, 075307 (2012).

[151] J. Bhattacharyya, S. Zybell, F. Eßer, M. Helm, H. Schneider, L. Schneebeli, C. N. Böttge, B. Breddermann, M. Kira, S. W. Koch, A. M. Andrews, and G. Strasser, Phys. Rev. B **89**, 125313 (2014), arXiv:arXiv:1309.6426v1.

[152] M. Schäfer, "Microscopic Theory of Coherent and Incoherent Optical Properties of Semiconductor Heterostructures", Dissertation (Philipps-Universität Marburg, 2008).

[153] M. Rieger, and P. Vogl, Phys. Rev. B **48**, 14276–14287 (1993).

[154] W. Weber, Phys. Rev. B **15**, 4789–4803 (1977).

[155] Y. J. Kuang, K. M. Yu, R. Kudrawiec, A. V. Luce, M. Ting, W. Walukiewicz, and C. W. Tu, Appl. Phys. Lett. **102**, 112105 (2013).

[156] B. Mayer, L. Janker, B. Loitsch, J. Treu, T. Kostenbader, S. Lichtmannecker, T. Reichert, S. Morkötter, M. Kaniber, G. Abstreiter, C. Gies, G. Koblmüller, and J. J. Finley, Nano Lett. **16**, 152–156 (2016).

[157] T. Stettner, P. Zimmermann, B. Loitsch, M. Döblinger, A. Regler, B. Mayer, J. Winnerl, S. Matich, H. Riedl, M. Kaniber, G. Abstreiter, G. Koblmüller, and J. J. Finley, Appl. Phys. Lett. **108**, 011108 (2016).

[158] I. Vurgaftman, and J. R. Meyer, J. Appl. Phys. **94**, 3675–3696 (2003).

[159] K. Uesugi, N. Morooka, and I. Suemune, Appl. Phys. Lett. **74**, 1254 (1999).

[160] B. M. Keyes, J. F. Geisz, P. C. Dippo, R. Reedy, C. Kramer, D. J. Friedman, S. R. Kurtz, and J. M. Olson, in Aip conf. proc. Vol. 462 (1999), p. 511.

[161] L. Malikova, F. H. Pollak, and R. Bhat, J. Electron. Mater. **27**, 484–487 (1998).

[162] R. Bhat, C. Caneau, L. Salamanca-Riba, C. Bi, and C. W. Tu, J. Cryst. Growth **195**, 427–437 (1998).

[163] I. Vurgaftman, J. R. Meyer, and L. R. Ram-Mohan, J. Appl. Phys. **89**, 5815 (2001).

[164] D. J. Wolford, J. A. Bradley, K. Fry, and J. Thompson, in Proc. 17th int. conf. phys. semicond. Edited by J. D. Chadi, and W. A. Harrison, (1985), pp. 627–630.

[165] X. Liu, M.-E. Pistol, L. Samuelson, S. Schwetlick, and W. Seifert, Appl. Phys. Lett. **56**, 1451 (1990).

[166] J. A. Van Vechten, and T. K. Bergstresser, Phys. Rev. B **1**, 3351–3358 (1970).

[167] S. Sakai, Y. Ueta, and Y. Terauchi, Jpn. J. Appl. Phys. **32**, 4413–4417 (1993).

[168] S.-H. Wei, and A. Zunger, Phys. Rev. Lett. **76**, 664–667 (1996).

[169] W. Shan, W. Walukiewicz, J. Ager, E. Haller, J. Geisz, D. Friedman, J. Olson, and S. Kurtz, Phys. Rev. Lett. **82**, 1221–1224 (1999).

[170] A. Lindsay, and E. P. O'Reilly, Solid State Commun. **112**, 443–447 (1999).

[171] S. Tomić, E. P. O'Reilly, P. J. Klar, H. Grüning, W. Heimbrodt, W. M. Chen, and I. A. Buyanova, Phys. Rev. B **69**, 1–12 (2004).

[172] I. Vurgaftman, Personal communication, Apr. 2015.

[173] M. Gladysiewicz, R. Kudrawiec, J. M. Miloszewski, P. Weetman, J. Misiewicz, and M. S. Wartak, J. Appl. Phys. **113**, 063514 (2013).

[174] I. A. Buyanova, G. Pozina, P. N. Hai, W. M. Chen, H. P. Xin, and C. W. Tu, Phys. Rev. B **63**, 033303 (2000).

[175] B. Q. Sun, D. S. Jiang, X. D. Luo, Z. Y. Xu, Z. Pan, L. H. Li, and R. H. Wu, Appl. Phys. Lett. **76**, 2862 (2000).

[176] J. Hader, S. W. Koch, J. V. Moloney, and E. P. O'Reilly, Appl. Phys. Lett. **76**, 3685 (2000).

[177] H. Grüning, L. Chen, T. Hartmann, P. J. Klar, W. Heimbrodt, F. Höhnsdorf, J. Koch, and W. Stolz, Phys. Status Solidi B **215**, 39–45 (1999).

[178] L. Bellaiche, S.-H. Wei, and A. Zunger, Appl. Phys. Lett. **70**, 3558 (1997).

[179] I. A. Buyanova, W. M. Chen, G. Pozina, J. P. Bergman, B. Monemar, H. P. Xin, and C. W. Tu, Appl. Phys. Lett. **75**, 501 (1999).

[180] K. Uesugi, N. Morooka, and I. Suemune, J. Cryst. Growth **201-202**, 355–358 (1999).

[181] I. A. Buyanova, W. M. Chen, G. Pozina, P. N. Hai, B. Monemar, H. P. Xin, and C. W. Tu, Mater. Sci. Eng. B **82**, 143–147 (2001).

Wissenschaftlicher Werdegang

Name	Phillip Springer
Geburtsdatum	24. Juli 1985
Geburtsort	Wuppertal

Juni 2005	Abitur an der Gesamtschule Hagen-Haspe
Oktober 2005	Beginn des Diplomstudiengangs Physik an der Philipps-Universität Marburg
Mai 2008	Vordiplom im Fach Physik
März 2011	Diplom im Fach Physik in der Arbeitsgruppe “Experimentelle Halbleiterphysik” bei Prof. Dr. Martin Koch an der Philipps-Universität Marburg
Juni 2011	Beginn der Promotion in der Arbeitsgruppe “Theoretische Halbleiterphysik” bei Prof. Dr. Stephan Koch an der Philipps-Universität Marburg